

AC Motor Design and Evaluation for Automotive Traction Applications

by

Johann Willberger

Doctoral Thesis

submitted to the Faculty of Mechanical Engineering and Economic Sciences
Graz University of Technology, Austria

Assessors

Prof. Dr. Wolfgang Hirschberg

Institute of Automotive Engineering, TU Graz, Austria

Prof. Dr. Annette Mütze

Electric Drives and Machines Institute, TU Graz, Austria

DECEMBER 2011



Abstract

Today's automotive industry faces fast changing impacts and conditions which forces fast and reliable decisions. The companies are pushed to innovative solutions, mainly caused by political concerns, aiming at a gentle handling of energy sources.

In order to meet average fleet consumptions, automotive manufacturers and suppliers are trying to replace existing mechanical systems with electric/mechatronic systems. Today exists a big variety of different partial or full electric power train configurations on the market, each using different electric drives with different design and optimization criteria. Which machine to use for a specific application and how to design and control them is probably one of the main issues in a hybrid vehicle development process. At present, conceptual design and dimensioning tools are of big interest as subsequent production and modifications costs can be lowered significantly. An efficient hybrid or full electric vehicle development process minimizes the overall development time for the design and the analysis of the entire mechatronic system and addresses electric motor selection issues and power train evaluation processes.

The present thesis presents a novel time-efficient design and modeling approach of two different AC drives which allows a fast evaluation of the machine topologies in conceptual design studies of automotive traction applications. The design methodology applies to the V-model of VDI-standard 2206 focusing on the sizing of electric motors under given geometric restrictions caused by the vehicle. The work has a special focus on the design of the electric machines and the analysis of the resulting thermal and operative machine characteristics.

Kurzfassung

Die Fahrzeugindustrie ist heutzutage mehr gefordert denn je zuvor. Das restriktive Umfeld heutiger Fahrzeughersteller, politischer oder gesellschaftlicher Natur, ändert sich rasch, sodass Entscheidungen in Innovations- oder Entwicklungsprozessen von Fahrzeugen sehr schnell und nachvollziehbar gefällt werden müssen.

Im Zuge der Realisierung von Flottenverbrauchszielen werden Antriebsstrangkomponenten im Fahrzeug sukzessive elektrifiziert. Aktuell existiert am Markt eine Vielzahl unterschiedlicher Antriebsstrangkonfigurationen wobei jede dieser Topologien verschiedene Typen von Elektromotoren mit unterschiedlichen Auslegungs- und Optimierkriterien verwendet. Welcher Maschinentyp für welchen Zweck unter gegebenen geometrischen Einschränkungen wie ausgelegt und betrieben werden sollte, stellen dabei essentielle Fragen in einem Entwicklungsprozess eines Fahrzeugs dar. Ein effizienter Entwicklungsprozess eines hybriden oder rein elektrischen Fahrzeugs versucht demnach, sowohl Analyse als auch Synthese des mechatronischen Gesamtentwicklungsprozesses zu reduzieren und widmet sich Berechnungs- und Evaluierungsprozessen von elektrischen Antriebsstrangkomponenten.

Der Schwerpunkt der vorgelegten Arbeit konzentriert sich auf die Berechnungsmethodik zweier verschiedener Elektromotortopologien unter spezieller Berücksichtigung geometrischer Restriktionen durch das Fahrzeug. Die entworfene Berechnungsmethodik basiert auf dem V-Modell aus der VDI-Richtlinie 2206, wobei der anwendungsspezifische Entwurf der Maschinen und die Analyse des resultierenden thermischen und operativen Verhaltens im Vordergrund steht. Ziel der Arbeit ist der Entwurf einer effizienten Berechnungsmethodik für die vorgestellten Motortopologien, die eine schnelle konstruktive und operative Evaluierung der Motoren für den Einsatz in hybriden oder rein elektrischen Traktionsantrieben im Fahrzeug unterstützt.

Acknowledgements

The present thesis was part of my work as a scientific researcher at the Institute of Automotive Engineering at Graz University of Technology, Austria. During my stay, I was involved in an advanced development project in cooperation with MAGNA Powertrain AG & Co KG focusing on in-wheel motors for automotive traction applications.

There are many people who have contributed to this work. First of all I want to thank my supervisor Prof. Dr. Wolfgang Hirschberg who gave me the opportunity to achieve a doctoral degree within the interesting subject of electric machines focused on hybrid power trains. I pretty much appreciated the discussions with him that gave me a much wider understanding of the daily things, not just technical issues but even social ones. A special thank goes to the team of the Electric Drives and Machines Institute headed by Prof. Dr. Annette Mütze. Although she joined the team recently she was very open-minded to the research work and supported it by many useful discussions. I am very grateful for the support of Ass.-Prof. Dr. Klaus Krischan who gave me many insightful recommendations throughout my research. Furthermore, I want to thank Mr. Arno Huber from THIEN eDrives GmbH who supported the thesis by many technical details concerning motor sizing. The present research work was greatly supported by the Department of Product Innovation at MAGNA Powertrain AG & Co KG. Therefore, I am very much obliged to Dipl.-Ing. Franz Gratzer and his team. My heartfelt appreciation goes to my girl friend Claudia and my son Julian. Many thanks to all of them.

*Johann Willberger
Graz, December 2011*

Statutory Declaration

I declare that I have authored this thesis independently, that I have not used other than the declared sources / resources, and that I have explicitly marked all material which has been quoted either literally or by content from the used sources.

Date: _____ Signature:

Nomenclature

Abbreviations

Chap.	Chapter
Fig.	Figure
Sec.	Section
Tab.	Table

Acronyms

AC	Alternating Current
ASIC	Application Specific Integrated Circuit
AWD	All-Wheel Drive
CFC	Constant Flux Control
DM	Design Methodology
DTC	Direct-Torque-Control
EM	Electric Motor
EMF	Electromotive Force
EV	Electric Vehicle
FEM	Finite Element Method
FOC	Field-Oriented Control
FTP	Federal Test Procedure
HEV	Hybrid Electric Vehicle
HR	Hybridization Ratio
ICE	Internal Combustion Engine
IM	Induction Motor
MMF	Magnetomotive Force
MTPA	Maximum Torque Per Ampere
NdFeB	Neodymium-Iron-Boron
NEDC	New European Driving Cycle
OD	On-Demand
PWM	Pulse-Width Modulation
PMSM	Permanent Magnet Synchronous Motor
RMS	Root Mean Square
SOC	State-Of-Charge
SOP	State-Of-Power

SRM	Switched Reluctance Motor
TTW	Tank-To-Wheel Efficiency
VFC	Variable Flux Control
WMA	Weighted Moving Average

Matrices and Vectors

B_δ	Flux density vector
C_{VB}	Transformation matrix
$d\mathbf{F}_\delta$	Infinitesimal Lorentz force vector
$d\mathbf{T}$	Infinitesimal torque output vector
\mathbf{F}_δ	Lorentz force vector
\mathbf{I}	Identity matrix
l_{fe}	Stack length vector
\mathbf{M}_{BB}	Mass matrix of vehicle body
\mathbf{M}_{FF}	Mass matrix of front axle
\mathbf{M}_{RR}	Mass matrix of rear axle
\mathbf{M}_{BF}	Coupling mass matrix between body and front axle
\mathbf{M}_{BR}	Coupling mass matrix between body and rear axle
$\mathbf{M}_{vehicle}$	Mass matrix of the full vehicle model
\mathbf{Q}_{VB}	Force and torque vector of vehicle body
\mathbf{Q}_{FA}	Force and torque vector of front axle
\mathbf{Q}_{RA}	Force and torque vector of rear axle
$\mathbf{Q}_{vehicle}$	Force and torque vector of the full vehicle model
r_δ	Air gap diameter vector
\mathbf{y}_{VB}	Minimum coordinates of main vehicle body
\mathbf{y}_{FA}	Minimum coordinates of front axle
\mathbf{y}_{RA}	Minimum coordinates of rear axle
\mathbf{z}_{VB}	Generalized velocities of vehicle body
\mathbf{z}_{FA}	Generalized velocities of front axle
\mathbf{z}_{RA}	Generalized velocities of rear axle
$\mathbf{z}_{vehicle}$	Generalized velocities of of the full vehicle model

Notation

a	Phase leg number [-]
a_i	Translational acceleration [$\frac{m}{s^2}$]
A_δ, A_b	Cross-sectional area [m^2]: air gap, bar (rotor)
A_{cS}, A_f	Cross-sectional area [m^2]: cooling (stator), front (vehicle)
A_m, A_r	Cross-sectional area [m^2]: magnet (rotor), ring (rotor)
A_{sl}, A_w	Cross-sectional area [m^2]: slot, conductor
A_R, A_S	Cross-sectional area [m^2]: rotor, stator
A_{fe}	Torque building cylinder area [m^2]
A_h	Thermal conductive cross-sectional area [m^2]
A_k	Thermal convective cross-sectional area [m^2]

Roman letters

A, A_d	Electric loading [$\frac{A}{m}$]: total, d-component
A_q	Electric loading [$\frac{A}{m}$]: q-component
$B_\delta, B_{fe}, B_{max}$	Flux density [T]: air gap, iron, maximum
B_r, B_t, B_y	Flux density [T]: remanence, tooth, yoke
C_{add}, C_{cu}	Loss coefficient [-]: additional, copper
C_{fe}, C_{al}	Loss coefficient [-]: iron, aluminium
C_f, C_i	Constant factor [-]: flux focusing, inductance slope
C_l, C_p	Constant factor [-]: leakage, permeance
C_r, C_u	Constant factor [-]: reluctance, utilization
c_d, c_p	Drag value [-], heat capacity [$\frac{Ws}{kg K}$]
d	Torque distribution factor [-]
d_δ, d_i, d_o, d_r	Diameter [m]: air gap, inner, outer, wheel rim
E_n	Nominal battery energy [kWh]
F_δ	Tangential force (Lorentz force) [N]
f_n, f_{slip}	Supply frequency, slip frequency [Hz]
h_r, h_{sl}, h_y, h_m	Height: slot opening, slot, yoke, magnet [m]
H_δ, H_c, H_m	Field strength [$\frac{A}{m}$]: air gap, coercive, magnet
H_t, H_y	Field strength [$\frac{A}{m}$]: tooth, yoke
I_R, I_S	Current [A]: rotor, stator
I_c, I_d, I_{dc}	Current [A]: charge, d-component, discharge
I_{max}, I_n	Current [A]: maximal, nominal
I_q, I_{ref}	Current [A]: q-component, reference
I_{sc}, I_{sl}	Current [A]: short-circuit, slot
J_{al}, J_{cu}, J_{sl}	Current density [$\frac{A}{mm^2}$]: aluminium, copper, slot
J_{ICE}	Moment of inertia [kgm^2]: combustion engine
J_{EM}	Moment of inertia [kgm^2]: electric motor
k_{fe}, k_{sl}	Fill factor [-]: iron, slot
L_{SR}, L_c	Leakage inductance [H]: stator and rotor, coil end
L_d, L_q	Leakage inductance [H]: d-component, q-component
$L_{sl}, L_t, L_\delta, L_\chi$	Leakage inductance [H]: slot, tooth, harmonic, skew
L_{m2m}	Leakage inductance [H]: magnet-to-magnet
L_{m2r}	Leakage inductance [H]: magnet-to-iron-core
l, l_δ, l_{act}	Length [m]: individual, air gap (radial), active
l_{ax}, l_w, l_{fe}	Length [m]: winding axial, winding mean, stack
m	Number of phases [-]
$m_{act}, m_{cu}, m_{fe}, m_v$	Mass [kg]: active, copper, iron, vehicle
n, n_n, n_{os}, n_{max}	Speed [rpm]: individual, rated, overspeed, maximum
p	Pole pair number [-]
P_{ICE}	Continuous power [W]: combustion engine
P_{EM}	Continuous power [W]: electric motor
P_R, P_S	Loss [W]: rotor, stator
P_{add}, P_{cu}	Loss [W]: additional, copper
P_{fe}, P_m	Loss [W]: iron, mechanical
P_{rel}, P_{total}	Loss [W]: relative, total
P_δ, P_i	Power [W]: air gap, apparent

P_{max}, P_{mech}, P_n	Power [W]: maximum, mechanical, nominal
Q	Number of slots [-]
q	Number of slots per pole and phase [-]
r_δ, r_i	Radius: air gap (middle), inner [m]
r_o, r_e	Radius: outer, tyre (effective) [m]
R_R, R_S	Resistance [Ω]: rotor, stator
R_b, R_r	Resistance [Ω]: bar (rotor), ring (rotor)
R_{m2m}	Reluctance [$\frac{A}{Vs}$]: magnet-to-magnet
R_{m2r}	Reluctance [$\frac{A}{Vs}$]: magnet-to-rotor iron
SP	Sound pressure level [dB]
s_χ	Skewing factor [-]
s, s_{po}, s_{ft}	Slip [-]: per-unit, pull-out, front tyre
T_∞, T_{ref}	Temperature [$^\circ C$]: maximum, reference
T_{fa}, T_n	Torque [Nm]: front axle, nominal
T_{max}, T_{po}	Torque [Nm]: maximum, pull-out
T_{ra}, T_r, T_s	Torque [Nm]: rear axle, reluctance, synchronous
T_{su}, T_{tot}	Torque [Nm]: start-up, total
t_e, t_{ol}	Time [s]: settling, overload
U_S, U_{Sd}, U_{Sq}	Voltage [V]: stator, d-component, q-component
U_b, U_i	Voltage [V]: battery, intermediate circuit
U_d, U_p	Voltage [V]: induced, back-EMF
v_c	Circumferential speed [$\frac{m}{s}$]
w_δ, w_{fe}	Width [m]: air gap, iron
w_m, w_{sl}, w_t	Width [m]: magnet, slot, tooth
X_R, X_S, X_{SR}	Reactance [Ω]: rotor, stator, stator and rotor

Notation

α	Rotational acceleration [$\frac{rad}{s^2}$]
α_{el}	Slot angle [rad]
α_{fl}	Flattening factor [-]
α_T	Linear temperature coefficient [$\frac{1}{K}$]
γ	Skew angle [-]
δ	Polar wheel angle [rad]
ϵ_0	Electric constant [$\frac{As}{Vm}$]
η_n	Nominal efficiency [%]
θ, θ_δ	Magnetomotive force [A]: total, air gap
θ_d, θ_q	Magnetomotive force [A]: d-, q-component
θ_{fe}, θ_m	Magnetomotive force [A]: iron, magnet
λ	Permeance ratio [-]
λ_c	Permeance value [-]: coil leakage
$\lambda_{sl,t}$	Permeance value [-]: slot and tooth tip leakage
λ_d, λ_q	Permeance [$\frac{Vs}{A}$]: d-, q-component
λ_{m2m}	Permeance [$\frac{Vs}{A}$]: magnet-to-magnet
λ_{m2r}	Permeance [$\frac{Vs}{A}$]: magnet-to-rotor iron

Greek letters

μ_0	Magnetic constant [$\frac{Vs}{Am}$]
μ_{fe}, μ_{rec}	Permeability [$\frac{Vs}{Am}$]: iron, recoil
ξ_c, ξ_d	Chord factor [-], distribution factor [-]
ξ_w	Winding factor [-]
ρ_{al}, ρ_{cu}	Specific resistance [Ωm]: aluminium, copper
σ_δ	Harmonic leakage factor [-]
σ_c	Leakage reduction factor [-]
σ_n	Nominal shear force density [$\frac{N}{m^2}$]
τ_c, τ_h	Time constants [s]: cooling, heating
$\tau_{cp}, \tau_{pp}, \tau_{sp}$	Coil pitch [m], pole pitch [m], slot pitch [m]
ϕ	Machine flux [Wb]
ϕ_l, ϕ_n	Machine flux [Wb]: leakage, nominal
ϕ_t, ϕ_y	Machine flux [Wb]: tooth, yoke
φ	Phase angle [rad]
φ_e, φ_m	Angle [rad]: electrical, mechanical
φ_p	Local displacement between two phases [rad]
φ_t	Time displacement between two phases [rad]
χ	Skewing reduction factor [-]
ψ_d, ψ_q	Flux linkage [Wb]: d-, q-component
ω_{ph}, ω_w	Number of turns [-]: per phase, per slot
ω_{sl}	Number of conductors per slot [-]
ω	Angular frequency [$\frac{rad}{s}$]
$\omega_n, \omega_m, \omega_{po}$	Angular frequency [$\frac{rad}{s}$]: nominal, mechanical, pull-out

Table of Contents

Abstract	iii
Kurzfassung	v
Acknowledgements	vii
Statutory Declaration	ix
Nomenclature	xi
List of Tables	xxi
List of Figures	xxiii
1 Introduction	1
1.1 V-Model Based Design Process	2
1.2 Purpose and Motivation	3
1.3 Outline of the Thesis	4
2 Hybrid Electric Power Train Topologies	7
2.1 The Early Steps of Electrification	7
2.2 Electrification of Power Trains Today	11
2.2.1 Hybrid Vehicle Topologies	11
2.2.2 Hybridization Ratio	15
2.2.3 Relevance of Different Hybrid Topologies Today	16
3 AC Machine Topology Issues	19
3.1 The Emerging of Variable Speed-Controlled AC Machines	19

3.2	Torque, Speed and Power Characteristics	20
3.3	Electric Machine Characterization	21
3.4	Assumptions	22
3.5	Induction Motors	23
3.5.1	Sizing	23
3.5.2	Operation, Control and Acoustic Noise	25
3.5.3	Fault Tolerance	27
3.6	Surface Permanent Magnet Synchronous Motors	29
3.6.1	Sizing	30
3.6.2	Operation, Control and Acoustic Noise	32
3.6.3	Fault Tolerance	34
4	AC Motor Design	37
4.1	Design Fundamentals	37
4.1.1	Current Sheet and Electric Loading	38
4.1.2	Magnetomotive Forces and Air Gap Fields	40
4.1.3	Electromagnetic Utilization	41
4.1.4	Lorentz Force and Torque Development	43
4.1.5	Loss Characterization and Computation	44
4.1.6	Leakage Analysis and Evaluation	47
4.1.7	Overload Capability	50
4.2	Design Methodology	53
4.2.1	Assumptions	54
4.2.2	Sizing Examples	54
4.2.3	Induction Motor Design	60
4.2.4	Surface Permanent Magnet Synchronous Motor Design	75
4.2.5	Summary and Discussion	86
5	AC Motor Operation	89
5.1	Assumptions	89
5.2	Energy Efficient Control Methods	90
5.2.1	Assumptions	90

5.2.2	Constant Flux Control Method	90
5.2.3	Variable Flux Control Method	93
5.3	Active Component Temperatures	96
5.3.1	Continuous Operation	98
5.3.2	Short-term Operation	100
5.4	Summary and Discussion	102
6	In-Wheel Motor Application	105
6.1	Assumptions	105
6.2	Vehicle Dynamics Model	106
6.3	In-Wheel Motor System Specification	107
6.4	Power Train Architecture	109
6.5	Power Train Components	111
6.6	New European Driving Cycle	113
6.6.1	On-Demand Operation Strategy	113
6.6.2	European City Cycle	114
6.6.3	European Urban Cycle	116
6.7	Summary and Discussion	119
7	Summary and Conclusion	121
A	Appendix A	125
A.1	Evaluation of Induction Motors and Permanent Magnet Synchronous Motors	125
B	Appendix B	129
B.1	Switched Reluctance Motors	129
B.1.1	Sizing	129
B.1.2	Operation, Control and Acoustic Noise	132
B.1.3	Fault Tolerance	134
	Bibliography	135

List of Tables

4.1	Suggested rotor diameters of machines depending on stator diameter and pole pair number.	55
4.2	Design parameters of induction motor and permanent magnet synchronous motor.	59
4.3	Comparison of electric loadings, induced voltages and magnetizing parameters of the induction motor.	71
4.4	Comparison of the component sizes and weights of the induction motor.	72
4.5	Comparison of component losses of the induction motor.	73
4.6	Comparison of the winding and pull-out torque parameters of the induction motor.	74
4.7	Summary of electric loadings, induced voltages and magnetizing parameters of the permanent magnet synchronous motor.	84
4.8	Summary of component losses of the designed permanent magnet synchronous motor.	84
4.9	Summary of resulting component sizes of the designed permanent magnet synchronous motor.	85
4.10	Summary of winding and pull-out torque parameters of the designed permanent magnet synchronous motor.	85
4.11	Comparison of the sized induction motor and the permanent magnet synchronous motor.	87
5.1	Computed loss coefficients of the designed induction motor and permanent magnet synchronous motor.	90
5.2	Applied power of the investigated operation modes.	98
5.3	Maximum overtemperatures of the active components of induction motor and synchronous motor.	99
5.4	Maximum overload duration of different control methods for induction motor and synchronous motor.	101

5.5	Thermal time constants and overload durations of the induction motor and permanent magnet synchronous motor.	103
6.1	System design specifications for the in-wheel motor configuration.	108
6.2	Vehicle data of the parallel hybrid power train topology.	110
6.3	Power train data of the parallel hybrid power train topology. . .	112
6.4	Comparison of operational characteristics of induction motor and permanent magnet synchronous motor in the European city cycle applying constant flux control.	115
6.5	Comparison operational characteristics of induction motor and the permanent magnet synchronous motor in the European city cycle applying variable flux control.	116
6.6	Comparison of operational characteristics of induction motor and the permanent magnet synchronous motor in the European urban cycle applying constant flux control.	117
6.7	Comparison of operational characteristics of induction motor and permanent magnet synchronous motor in the European urban cycle applying variable flux control.	118
A.1	Overview of different design and operational characteristics of induction motors and permanent magnet synchronous motors, part 1.	126
A.2	Overview of different design and operational characteristics of induction motors and permanent magnet synchronous motors, part 2.	127

List of Figures

1.1	V-Model based power train development process.	2
1.2	Utilization of the VDI-model for the development of electric drives for automotive traction applications.	4
2.1	Advertisement of electric and gasoline automobiles at the turn of the 20 th century.	8
2.2	Historic series hybrids invented by Ferdinand Porsche.	9
2.3	Historic series hybrid car published by the Canadian Galt Motor Company.	10
2.4	Principal sketch of a series hybrid electric vehicle.	12
2.5	Principal sketch of a parallel hybrid electric vehicle.	13
2.6	Principal sketch of a power-split hybrid electric vehicle.	14
2.7	Comparison of relative fuel consumption reduction realized of parallel and series hybrid vehicles as a function of the hybridization ratio.	15
2.8	Costs of parallel and hybrid HEVs depending different hybridization ratios.	16
2.9	Market available hybrid power train topologies by the year 2010.	17
3.1	Comparison of the tractive power chart diagram with the torque-speed profile of a speed-controlled electric motor.	20
3.2	Representation of the characteristic machine design parameters.	21
3.3	Representation of the active machine components of a three-phase four-pole induction motor.	23
3.4	Normed copper and iron losses of an induction motor stator.	26
3.5	Comparison of different control approaches of induction motors concerning efficiency.	26
3.6	Comparison of sound pressure and stator current of induction motors at different loads.	27

3.7	Distributed winding topology induction machines.	28
3.8	Active machine components and a rotor fixed coordinate system along different magnetization directions of synchronous machines.	29
3.9	Operational characteristics of Neodymium-Iron-Boron magnets.	32
3.10	Concentrated winding topology at fault-tolerant synchronous machines.	34
4.1	Illustration of a single layer winding and the corresponding electric loading.	39
4.2	Utilization factor range for all motor types.	43
4.3	Simplified circuit model for overload considerations of induction motors.	50
4.4	Simplified circuit models for different magnetization directions of synchronous motors.	52
4.5	Characteristics of two different electric sheets.	58
4.6	Magnetic field characteristics of the induction motor.	60
4.7	Magnetic circuit of the designed induction motor.	62
4.8	Different tooth flux densities and the corresponding magnetic excitations of the induction machine.	63
4.9	Sinusoidal yoke flux densities and the corresponding magnetic excitations for the induction machine.	64
4.10	Air gap flux density characteristic at different magnetizing currents for the induction motor.	64
4.11	Magnetizing permeance at different magnetizing currents of the induction motor.	65
4.12	Iterative computation algorithm for the induction motor - design stage 1.	66
4.13	Iterative computation algorithm for the induction motor - design stage 2.	68
4.14	Iterative computation algorithm for the induction motor - design stage three.	70
4.15	Magnet design configurations of surface mounted permanent magnet synchronous motors.	75
4.16	Transformation of three-phase values on a two-dimensional operation vector showing d- and q-components of the permanent magnet synchronous motor.	76
4.17	Magnetic circuit of the permanent magnet synchronous motor.	77

4.18	Operation range of permanent magnets.	78
4.19	Local flux densities of the permanent magnet synchronous motor.	79
4.20	Magnetizing curve of the designed permanent magnet synchronous motor.	79
4.21	Permeance ratio as a function of the magnetizing current at synchronous motors.	80
4.22	Iterative computation algorithm for synchronous motors - design stage two.	82
4.23	Fundamental wave along the main magnetization direction of synchronous motors.	82
5.1	Constant flux control method.	91
5.2	Constant flux control - comparison of the magnetizing current of induction motor and permanent magnet synchronous motor.	91
5.3	Constant flux control - comparison of the torque building current of induction motor and permanent magnet synchronous motor.	92
5.4	Constant flux control - comparison of the resulting motor efficiencies of induction motor and permanent magnet synchronous motor.	92
5.5	Advantageous operation ranges of induction motor and permanent magnet synchronous motor.	93
5.6	Variable flux control method.	93
5.7	Variable flux control - comparison of the magnetizing current of induction motor and permanent magnet synchronous motor.	94
5.8	Variable flux control - comparison of torque building current between induction motor and permanent magnet synchronous motor.	94
5.9	Variable flux control - comparison of the absolute motor efficiency increases of induction motor and permanent magnet synchronous motor at different loads.	95
5.10	Variable flux control - comparison of absolute motor efficiency increases of induction motor and permanent magnet synchronous motor at different speeds.	96
5.11	Thermal interaction of the active components of the designed motor types.	97
5.12	Overtemperature characteristic of stator winding and rotor cage of the designed induction motor.	98

5.13	Overtemperature characteristic of stator winding and rotor magnet of the designed permanent magnet synchronous motor. . . .	99
5.14	Influence of different control methods on overtemperature of rotor cage of the designed induction motor.	100
5.15	Influence of different control methods on overtemperature of stator winding of the designed permanent magnet synchronous motor.	100
6.1	Full vehicle model of veDYNA including driving and steering components.	107
6.2	Power train architecture and operation strategy of the hybrid vehicle.	109
6.3	Operation modes of the integrated in-wheel motors.	110
6.4	Motor package study at a double wishbone suspension.	111
6.5	City cycle and urban cycle of the European test procedure. . . .	113
6.6	Normed rear axle torque during European test procedure. . . .	114
6.7	Electric motor operation distribution in the European city cycle.	114
6.8	Generator efficiency map of the induction motor and the permanent magnet synchronous motor.	116
6.9	Electric motor operation distribution in the European urban cycle.	117
7.1	Iron stacks of the assembled induction motor.	124
B.1	Flux linkage, phase inductance and phase current as a function of the rotor tooth position for a single phase of a switched reluctance machine.	130
B.2	Comparison of different turn-on angles of a switched reluctance motor drive as a function of the rotor position.	133

“Do not fear a slow move forward, but fear to stand
still. Success does not know any shortcut.”
(Tanaka Masahiko)

to my son Julian

1

Introduction

Mobility is considered to be a basic need of humanity. Therefore, automobiles always had and still have a strong presence and importance for human beings. Providing mobility in future is a sociological and technical challenge. Today's automotive industry faces fast changing impacts and conditions which forces fast and reliable decisions. Some of these issues exist since the first automobile was invented. Cost and quality have always been of big interest to the consumers, however, the variety of present vehicles is wide and changed dramatically compared to former times. The continuous integration of mechatronic power train components leads to an increase of the overall system complexity. Automotive companies are pushed to innovative solutions, mainly caused by political concerns, aiming at a gentle handling of energy sources. Shorter product innovation cycles cause cost and time urgencies which counteract product quality and consumer expectations.

During the 1960s up to the 1970s the development time for a vehicle was approximately seven years. However, today's vehicles are developed within a two years innovation cycle [HIR10]. Since then, the development time decreased by approximately 70% facing a much higher number of vehicle variants. One of the most challenging task concerning the development of vehicles is the consideration of the entire system itself, especially longitudinal vehicle dynamics. In most cases, the system design is done independently. In fact, this frequently results in system components being able to handle maximum loads. The reason for it looks very simple, however, its solution is challenging. Neglecting system relationships and dependencies normally results in oversized system components [NP06]. Thus, an effective design process considers all relationships of superior and inferior

system design stages combining linked virtual design and simulation tools with expert knowledge. At present, virtual design and dimensioning tools are of big interest as the early development process impacts subsequent production costs by 70% [SR08]. Virtual design tools allow a basic dimensioning of system components at relatively low computing time. Product optimization can already be done during early development stages which significantly reduces product varieties and subsequent product modification costs.

1.1 V-Model Based Design Process

Fig. 1.1 depicts the development process stages of mechatronic system design methods based on the V-model of VDI-standard 2206 [SR08]. The vertical axis of the design process reflects the degree of detail of the entire system design. Therefore, the degree of detail gets higher at lower system hierarchies. The horizontal axis is considered to be the time axis representing the verification and validation efforts of the corresponding test procedures. The V-model can basically be split up into stages of system design, domain specific optimization and system integration. This process is continuously verified and validated at different development stages up to the final product. The system design stage focuses on the implementation of the system specifications at a defined accuracy. The stage considers mechanical, electrical and software requirements for a given partial or entire system test. The domain specific optimization is probably the most intensive design stage examining the effects of different system

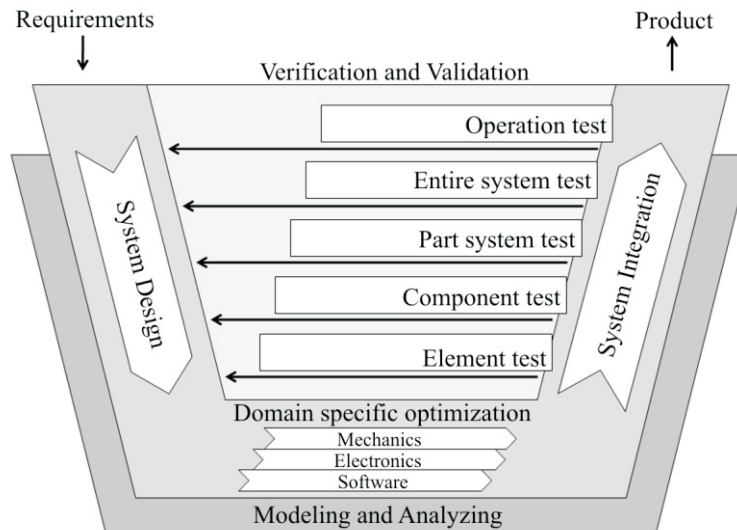


Figure 1.1: V-Model based power train development process (VDI-standard 2206) [SR08].

variants, different operation variants and modifications of system behavior and costs. The third design stage contains the system integration in combination with the system test at different development stages. The information flow between the different design levels is not unidirectional, as the effects of system modifications can eventually be seen at successive design stages. Hence, the information exchange needs to be bidirectional in order to get a product fulfilling the predefined requirements.

1.2 Purpose and Motivation

Bidirectional information flow within a design process is an essential but time-intensive procedure. An efficient mechatronic system development quickly provides information to superior or inferior system hierarchies. It tries to minimize the overall development time for the design and analysis of the entire system.

Finite-Element (FE) programs such as ANSYS Maxwell2D/3D® or JMAG® are well-established in professional circles [ANS11] [JMA11]. However, machine sizing on a FE basis represents a computationally intensive system design procedure which may reach 8 – 16 hours depending on the electric motor type [WEI06]. Thus, design parameters derived from the underlying application scenarios should be accurately known in order to prevent unneeded long system design phases and ensure a fast information flow to other system hierarchies. Considering new hybrid vehicle architectures, the design parameters of the machines are mostly known rudimentarily. The optimum traction drive should be able to handle predefined operation points at highest efficiency considering a maximum acceptable active machine volume. The design process therefore has to evaluate several optimization criteria which need to be solved iteratively. In fact, there is a need of a time-efficient computation algorithm trying to find a first estimation of an ideal layout of the traction drive for a given application scenario under predefined requirements of vehicle dynamics.

The present work addresses this problem and applies it to the V-model of VDI-standard 2206. The goal of the design methodology (DM) is to introduce a time-efficient computation algorithm on an analytic basis trying to allow a determination of the machine sizes for given geometric and thermal limitations of the machine components. The thesis therefore concentrates on the domain specific optimization of induction motors and permanent magnet synchronous motors with surface mounted magnets considering design and operational issues on a simulative basis, see Fig. 1.2. The introduced DM directly evaluates the resulting speed-controlled efficiency maps of the machines and shows efficiency optimization potentials by energy efficient control methods. The resulting design and operational characteristics of the DM support a rapid information flow to other system hierarchies. The DM is planned to allow a faster and reliable validation of different electric machines for hybrid or pure electric vehicles under a given application scenario.

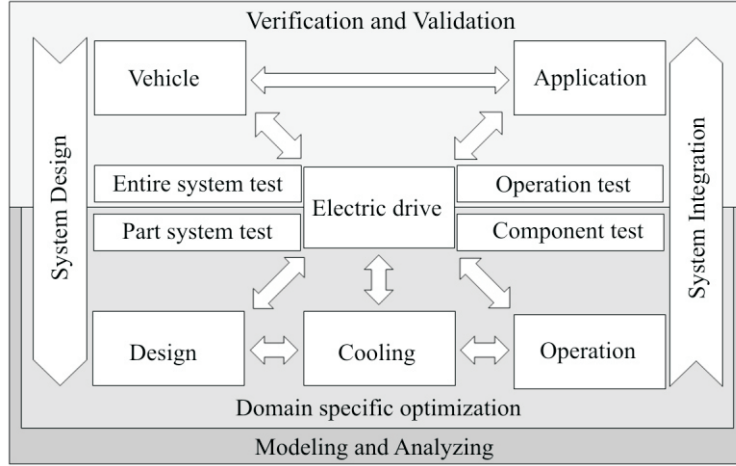


Figure 1.2: Utilization of the VDI-model for the development of electric drives for automotive traction applications.

1.3 Outline of the Thesis

Chap. 2 gives a short introduction into the chronology of development steps of hybrid electric power trains and reflects the status quo of currently used hybrid power train architectures.

Chap. 3 reports background information of machine sizing focusing induction motors and permanent magnet synchronous motors. It gives an overview of the status quo concerning sizing, operation, control and fault tolerant issues.

Chap. 4 presents a detailed look into AC motor design focusing the previously mentioned machines. The fundamental equations of their magnetomotive forces are derived and the computation of the motor sizes and operational characteristics are introduced by a time-efficient computational algorithm. An evaluation of the machine design characteristics is given at the end of the chapter.

Chap. 5 concentrates on AC motor operation issues and gives an insight into the resulting efficiency maps and the machine component temperatures at continuous and short-term operation. Chap. 5 emphasizes individual advantageous operation ranges and presents optimization potentials by energy efficient control methods. An evaluation of the operative characteristics is given at the end of the chapter.

Chap. 6 presents an energetic cycle analysis of the machines used as in-wheel motors. The motors act as “on-demand” torque supplier on the rear axle representing an electrical all-wheel drive concept. The comparison of the machines is based on the New European Driving Cycle having a detailed look into fuel consumption savings by energy efficient control methods of the machines.

Finally, Chap. 7 summarizes presented work and points out the main issues of the individual chapters.

2

Hybrid Electric Power Train Topologies - A Chronology of Developments

Chap. 2 gives a brief introduction into the history of electric propulsion from the early 19th century up to the present. Furthermore, it provides an overview of existing partial power train topologies and points out configuration, functionality and efficiency.

2.1 The Early Steps of Electrification

The history of electric propulsion started at the beginning of the 19th century and was closely related to the history of batteries. Numerous inventors in Europe and North America pushed on a replacement for the horse to move people and goods. In 1821, the Briton Michael Faraday demonstrated the principles of the electric motor. Later, in 1831, Faraday showed the principles of electromagnetic induction with the physical relation between electric currents and magnetism representing the basis of electric motors [HØY08]. The first experimental lightweight electric vehicles appeared in 1834. The 1860s until the beginning of the 1880s have probably been the most inventive decades in automotive history. The Belgian Etienne Lenoir invented the first internal combustion engine (ICE) in the early 1860s, Nicholas Otto produced the four-cycle engine in the late 1870s, Gottlieb Daimler and Karl Benz produced the first commercial automobiles in Germany in the late 1880s, and Thomas Edison and George Westinghouse introduced the electric power generation at the beginning of the

1880s. At the turn of the 20th century electric vehicles were the most common means of transportation in the United States and in Europe. In 1900, there were a total of 2370 automobiles in New York, Chicago and Boston, of which 50% were steamers, 34% were electrics, and only 16% were gasoline powered [SUL04]. The number of steam-powered cars decreased significantly within the following decade as they had poor acceleration capability and suffered from intense maintenance. Gasoline powered vehicles at that time were considered to be noisy, smelly and polluting. They were unreliable, prone to mechanical problems and had to be cranked by hand to start them. Many people, especially women, therefore preferred the push-button electrics, as they did not require any shifting of gears or turning of hand-cranks. Electric automobiles were simply considered to be “neater” than gasoline and steam-powered automobiles. They were easier to operate and produced no steam or odor [D’A93]. In 1899, the popular newspaper *Scientific American* praised electricity as an “ideal power for vehicles, for it eliminates all the complicated machinery of either gas, steam, or compressed air motors, with their accompanying noise, heat, and vibration” [SOV09].



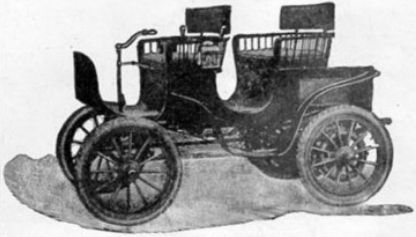

	Automobiles Electric Gasolene	 AUTOMOBILES ELECTRIC GASOLENE
<p>Forty Miles on Each Battery Charge. Safe, reliable, free from noise, odor and dirt, and easily operated by man, woman or child, the perfected electric vehicle excels for all city and suburban uses.</p>	 <small>COLUMBIA ELECTRIC SURREY</small>	 Afford the maximum of Safety, Reliability, Comfort, Luxury <small>Vehicles for all requirements of pleasure or business</small> Write for catalogue of 11 different Columbia models
<p style="text-align: center;"><i>Write for 1901 Illustrated Catalog and Price List.</i></p> <p>ELECTRIC VEHICLE COMPANY, HARTFORD, CONN. <small>Western Agency and Showrooms, No. 267 Wabash Avenue, Chicago, Ill.</small></p> <p style="text-align: right;">Electric Vehicle Co. Hartford, Conn. <small>NEW YORK - 100 Broadway BOSTON - 43-45 Columbus Ave. CHICAGO - 1421 Michigan Ave.</small></p>		

Figure 2.1: Advertisement of electric and gasoline automobiles at the turn of the 20th century [MUL10].

At the beginning of the 20th century the battery technology was in its infancy. Early lead-acid batteries had an energy density of 9Wh/kg to 13Wh/kg resulting in a battery weight of 77kg for 1kWh at best case. These batteries provided a pure electric range of 30 to 70 kilometers and an electric vehicle top speed of approximately 24km/h. Taxi companies in London, New York and Paris represented the first enterprises which replaced their fleets by electric vehicles, as the daily distances of their “cabs” were well within the battery range, see Fig. 2.1. The electric vehicle at the turn of the century was an appropriate means of transportation within cities. The distances were easily manageable, besides

charging stations were well established and very common within cities or urban areas. On the other hand the necessary electric infrastructure for recharging vehicle batteries, either at home or at nearby locations, was very bad in rural areas. They simply did not exist. Even distances were far longer. The most powerful and pervading factor towards gas automobiles was certainly the fact that this technology was available at a lower price. The costs of a gasoline automobile in 1900 were \$1000 to \$2000, whereas that of an electric vehicle were \$1250 to \$3500. The average income at the turn of the 20th century was upon 438\$ per year, which evidences the enormous price issue car manufacturers were facing [EMB08]. Concerning vehicle operation the costs of electric cars were two to three times higher compared to gasoline cars. Because of that, gasoline powered vehicles already took the lead in numbers and popularity by 1905. In 1909, the number of electric cars being produced was down to 4.4% of the number of gasoline-driven automobiles [D'A93].



a) Military application.



b) Race car application.

Figure 2.2: Historic series hybrids invented by the Austrian Ferdinand Porsche. Both vehicles were equipped with in-wheel motors at the front axle [WRR10].

At the same time, a further important technology came up - the hybrids. The automobile engineer Ferdinand Porsche was one of the first inventors in this field. These early hybrids also included regenerative braking technologies, see Fig. 2.2. They claimed to combine the best of electric and gasoline powered vehicles: noiseless when driving in city areas and with no limits concerning the range of the car outside the cities [HØY08]. In 1914, the Canadian *Galt Motor Company* had a hybrid on the market with a top speed of 50km/h, and a fuel consumption of four liters per 100km [AA05]. Even though the top speed is not particularly impressive from a today's point of view, the fuel consumption level is better than that of the Toyota Prius model in 2004 [JB02]. Fig. 2.3 depicts a view of this historic hybrid vehicle. This was the last hybrid production of any importance for a long time. Mainly due to cost reasons, the hybrid concept more or less disappeared from the First World War until the early 1970s. Due to the energy crisis, there had been a second hybrid initiative in politics and economy in the early 70s. The US Congress passed the *Electric and Hybrid Vehicle Act of 1976*, establishing a demonstration programme with the explicit aim to make the USA an all-electric car economy by the year 2000 [AA05]. As fast as those

initiatives arose, they had been abandoned by the end of the decade. It was generally concluded that neither electric nor hybrid cars were able to compete with gasoline driven cars.

The third era began in the 1990s. Toyota launched their Prius hybrid sedan model on the Japanese market in 1997. At the same time, Audi was the first European manufacturer to put a hybrid, the *Audi Duo*, on the market [HØY08]. This decade was probably the most intensive period concerning hybrid or electric car research and development. New efforts were put into the development of new batteries and more efficient electric motor drives. Several countries took the chance to establish new car manufacturing plants, such as the *Think Car Company*, which was founded in Norway and later taken over by the American *Ford Motor Company*.

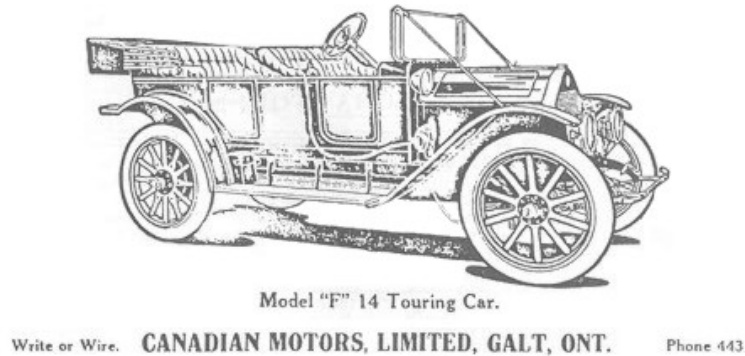


Figure 2.3: Historic series hybrid car published by the Canadian Galt Motor Company [WRR10].

The history of electric and hybrid car development has not been a history of continuous success. Obviously, it has been accompanied by many ups and downs. The downs have largely been the same as today; costly batteries, small ranges, and time consuming recharging conditions. The ups have taken place due to environmental concerns meaning local and global pollution, noise reduction and the call for sustainability of energy resources. Climate change and the finiteness of fossil energy resources nowadays is a worldwide concern. Countries all over the world are therefore obliged to deal with the subject of an energy efficient use of our all resources. One way to address this global challenge is certainly the full or partial electrification of power train systems.

2.2 Electrification of Power Trains Today

Partial electric vehicles, so-called *Hybrids*, are generally known as vehicles having two different energy sources together with two different energy converters.

Modeling a hybrid or pure electric power train topology requires the consideration of each power train component in order to be able to understand all mechanical and electrical energy flows. The superior control unit, frequently known as operation strategy, differs according to the individual power train topology and provides the implemented operation modes of the vehicle. The operation strategy of an electric vehicle is quite simple, as it can be reduced down to the pure electric conformance to power requirements. The operation modes of hybrid vehicles are numerous and depend on the power train topology and the degree of hybridization. In order to shorten and ease the development process of these control units the individual application scenarios of the vehicle under development are of essential importance. The more is known about possible use cases of the vehicle, the more decisions regarding suitability of hybrid topologies and reasonable degrees of hybridization can be made.

2.2.1 Hybrid Vehicle Topologies

There exists a large variety of possibilities to combine mechanical and electrical system components within a hybrid electric vehicle (HEV). The elementary hybrid system topologies are classified into series HEV, parallel HEV, and power-split HEV topologies, which are briefly described in the following.

Series Hybrid Topology

The series HEV is characterized by a series connection of all energy converters. The internal combustion engine (ICE) is electrically decoupled from the wheel speed of the vehicle, see Fig. 2.4. The structure of a series HEV liberates the ICE and allows it to be operated mostly within an area of better efficiency as an on-board generator. An electric machine (EM_1), operating in generator mode, converts the mechanical energy into electrical energy which can either be stored in an energy storage device, or directly supply a second electric machine that is operated as a motor (EM_2) [BOS07]. This motor is mechanically coupled to the propelled axle. A clutch mechanism is not mandatory. Depending on the power of the electric motor a gear drive might not be necessary either. The basic operation modes are electric driving and electric braking. In addition, the ICE can be operated dynamically if the battery is not able to provide sufficient power. In order to meet the needs for the required torque, series HEVs usually employ a relatively powerful on-board battery pack and electric motor which tends to increase the overall power train mass [XW07]. Therefore, the electric power components need to be designed for the entire propulsion power which results in higher component sizes and higher cooling requirements. Moreover,

series HEVs represent a long efficiency chain leading to sometimes unsatisfactory overall power train efficiencies. The primary energy reservoir is converted up to four times until it is applied on the wheels. Fig. 2.4 shows the corresponding minimum losses for each system component of a series HEV. The system boundary for the efficiency calculation is the power train topology. The overall maximum power train efficiencies can therefore be considered as Tank-To-Wheel (TTW) efficiencies.

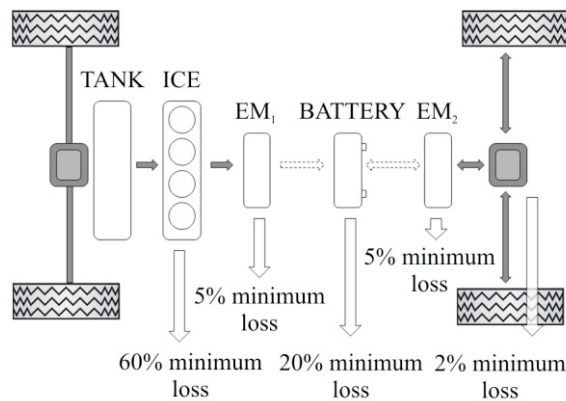


Figure 2.4: Principal sketch of a series HEV.

According to Fig. 2.4, the energy flow is unidirectional from the ICE to the battery, the power path considering all system components from the battery to the wheel is bidirectional. An internal combustion engine being operated in its best point produces at least 60% of losses, representing a maximum efficiency of 40%. The electric motor drives are considered by a minimal loss of 5%. For a commercially available battery and power electronic converter maximum efficiencies of around 80% can be given [XW07]. Considering the entire efficiency chain of the series HEV, the maximum TTW efficiency goes down to 28%. For pure electric driving the maximum TTW efficiency can be estimated by approximately 84%.

Parallel Hybrid Topology

Parallel HEVs are characterized by a mechanical coupling of the ICE and the driven wheels. The engine is therefore coupled to the wheels which basically forces the integration of a clutch mechanism and a gear box. The design options of parallel HEVs are manifold and vary according to the sequence of ICE, clutch and electric motor drive. Only one electric motor exists for a parallel topology which can either be operated as generator or as motor. According to this, the battery knows two states, charging and discharging, of which only one can be active at a given time. The parallel HEV topology basically combines ICE power with electric motor power. The sum of the two power sources can either

be managed by a gear box or by a road itself. Power addition via the road is known as *Through-The-Road-Hybrid* topology. The parallel HEV topology has the freedom to adjust the most efficient system component combination settings for a given driver input. Therefore, the operation strategy represents a big challenge due to the fact that the power restrictions and efficiencies of all system components need to be known. The basic operation modes are pure electric driving, electric braking, pure ICE operation and combined operation of both power sources (ICE load point shifts). For these reasons, parallel HEV strategies are more numerous, need to handle more information and are therefore more complex than series ones. Compared to series HEVs, long efficiency chains can be avoided and system modules do not need to be designed for the full propulsion power requirements, which might result in smaller components. Hence, parallel HEVs are able to represent a better compromise considering a compact vehicle packaging.

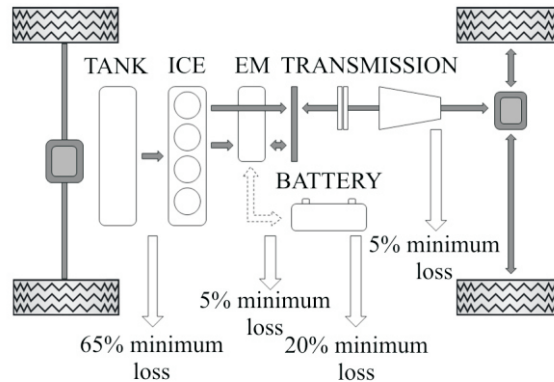


Figure 2.5: Principal sketch of a parallel HEV.

According to Fig. 2.5, the energy flow is unidirectional from the ICE to the electric motor drive, and bidirectional from the wheels to the battery. The ICE speed is coupled to the wheels which means that the engine can hardly be operated in its best efficiency point during different driving conditions. Indeed, this increases the ICE losses to a minimum cycle loss of about 65%. The other system component losses are assumed to be quite the same as with series HEVs. Anyhow, due to the greater number of possible operation modes there exists a relatively high variation of the TTW efficiency. Considering pure electric driving, which represents the most efficient chain, a maximum TTW efficiency of approximately 81% can be reached.

Power-Split Hybrid Topology

The power-split hybrid topology can be regarded as a combination of the previously mentioned series and parallel HEV topologies. The concept comprises one

ICE and two electric machines (EM_1 , EM_2). EM_1 is operated as a generator, EM_2 works as a motor unit. In fact, the ICE is mechanically connected to the wheels, however, its speed is electrically decoupled. Depending on the driver torque demand, the power-split HEV chooses the most efficient path to achieve the required torque.

Basically, the higher the torque demand, the higher the advantages of the parallel HEV topology. Contrary, the lower the torque demand, the higher the advantages of the series HEV topology. The reason for this is that high torque inputs can efficiently be provided by the ICE engine, a further load shifting into upper operation ranges is useful and additionally improves the engine efficiency. Low torque requirements represent advantages for the series HEV as the torque demand can be settled by the electric motor and the ICE can efficiently be operated on the characteristic full load curve representing the highest ICE efficiencies. The basic operation modes are pure electric driving, electric braking, power-split drive and shifting of ICE load points. The power-split HEV represents a maximum number of degrees of freedom concerning the operation modes and can therefore be seen as the most complex topology. The concept is based on a power distribution which can effectively be done by a planetary gear box. Compared to stand-alone variants of series and parallel HEVs the power-split HEV represents the most component intensive topology.

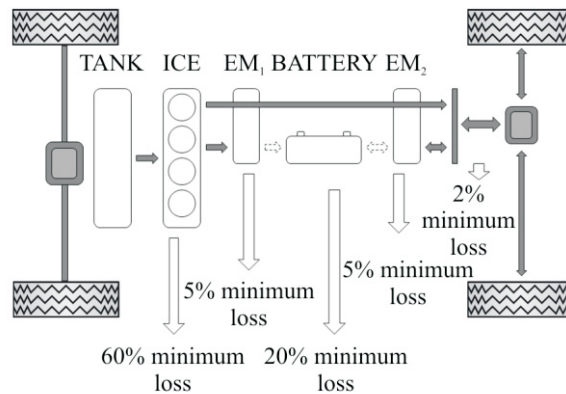


Figure 2.6: Principal sketch of a power-split HEV.

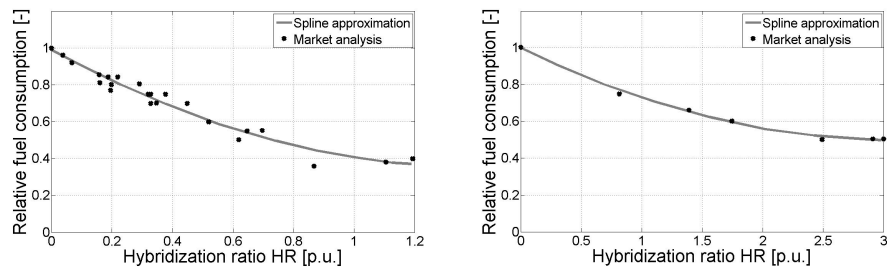
According to Fig. 2.6, the energy flow is unidirectional from the ICE via the generator EM_1 to the battery and bidirectional from the wheels to the battery via EM_2 . The maximum TTW efficiencies vary with the numerous possible modes of operation. However, pure electric driving can result in a maximum estimated TTW efficiency of approximately 84%.

2.2.2 Hybridization Ratio

Hybridization ratios are a useful characterization of HEV topologies concerning functionality, performance, fuel economy and costs. The standard classification schemes of different hybridization levels such as *micro*, *mild* and *full hybrid* systems are well known among experts. However, they do not convey any information on how to choose reasonable relations between the ICE power output and the output of electric motors. There exist no standardized classification schemes of hybrids, which makes the evaluation of technical and economical HEV parameters generally very difficult. Therefore, each company had developed its own solution on how to choose the relation between ICE and electric motor sizes [LE04]. The hybridization ratio (HR) is a relational operator and is defined as

$$HR = \frac{P_{EM}}{P_{ICE}}, \quad (2.1)$$

with P_{EM} being the continuous electromotive power output and P_{ICE} being the continuous internal combustion engine power output for vehicle traction. The HR in Equ. (2.1) can vary from near zero (for a conventional vehicle) up to infinity (for a pure electric vehicle) [BBH09].



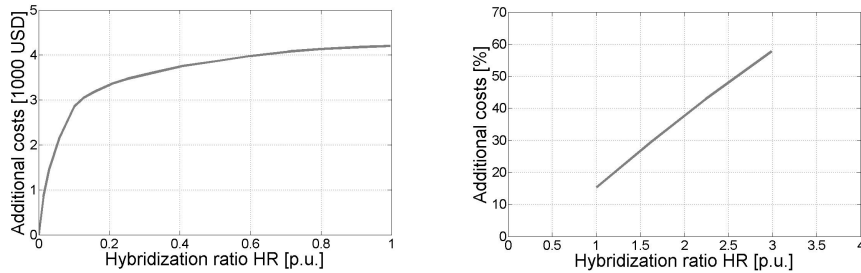
a) Relative fuel consumption of parallel HEV concepts.

b) Relative fuel consumption of series HEV concepts.

Figure 2.7: Comparison of relative fuel consumption reduction of parallel and series HEVs as a function of the HR [BBH09].

Fig. 2.7 shows the relationships between the HR and the fuel consumption for parallel, power-split (a) and series HEV topologies (b). The fuel consumption is based on the comparison of hybrid cars with their non-hybrid counterparts [BBH09]. The spline approximation of the relative fuel consumption conveys a clear relationship between HR and relative fuel saving potential of a given HEV topology. The relative fuel consumption of parallel and power-split HEVs is quite linear up to a HR of 0.3, however, it heavily declines at higher HRs which becomes quite obvious at a HR of 0.6. Series HEV topologies show a considerable decline of the relative fuel consumption at a HR of approximately 1. A further increase of the HR would lead to an increase of the relative fuel

consumption due to additional system masses which become dominant at higher HR ranges. Based on market analysis data of 2006, [BHE06] states in his work that the fuel saving potential of parallel HEV topologies is within 5% to 25%, those of series HEVs is approximately 50% and power-split HEV topology may reach a fuel saving potential of 60% to 65%.



a) Additional costs for different HRs at parallel HEVs.

b) Additional costs for different HRs at series HEVs.

Figure 2.8: Additional costs of parallel and hybrid HEVs depending on different HRs [BBH09].

Fig. 2.8 shows an estimation of additional costs for HEV topologies compared with a conventional car based on accessible information in [BHE06]. These figures show a snapshot of the automotive market in 2006 and are strongly related to the development of the world wide economy. Product costs might have changed since that, nevertheless, they show a reference on how automotive manufacturers are challenged regarding costs and fuel consumption reduction. The hybridization of a conventional car with an additional cost restriction of approximately \$3000 would therefore result in relative fuel saving of 11% with a HR of 12%. The additional costs for series hybrid topologies are generally higher than those of parallel or power-split hybrid topologies due to the higher requirements on energy storage systems. The additional costs of a HEV with a HR of 3 are approximately 50% to 60% higher compared to conventional configurations [BHE06].

Fuel consumptions cannot be a standalone decision parameter for designing hybrid electric vehicle topologies. The decision which HR to use is made by the consideration of vehicle dynamics, application scenario, functionality, fuel consumption and eventually the overall vehicle costs.

2.2.3 Relevance of Different Hybrid Topologies Today

The examination of today's HEV topologies clearly shows that the relevance of a particular topology depends on its potential use. While series hybrid concepts are frequently used in commercial vehicle or rail car applications, parallel and

power-split hybrid concepts are predominately used in automobiles. The following market analysis of HEV topologies considers 20 vehicles being currently available on the market or close to start of production.

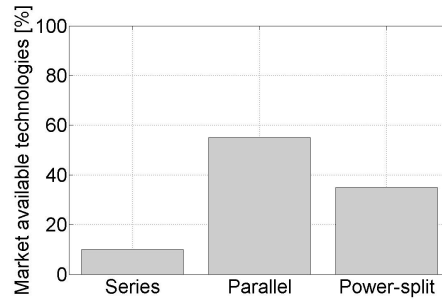


Figure 2.9: Market available hybrid power train topologies by the year 2010.

Fig. 2.9 shows that series HEV topologies have hardly any relevance for automotive manufacturers as they represent only 10% of the available technologies. The considered series hybrids are exclusively commercial vehicles. Parallel HEVs take the lead as they represent 55% out of the investigated power train topologies. The remaining percentage of 35% can be assigned to power-split HEV topologies.

Indeed, the favored use of parallel HEV can be explained by a lower complexity compared to power-split topologies. A potential entry of an automotive manufacturer on the hybrid market represents the lowest risk regarding fail-safe behavior and costs for parallel topologies. Furthermore, the information gain concerning system behavior should be the highest for this topologies under given costs.

3

AC Machine Topology Issues

Chap. 3 investigates different electric machine topologies concerning their design, their operational characteristics and their fail-safe behavior. The present chapter aims to give background information on these issues trying to ease the design considerations given in Chap. 4.

3.1 The Emerging of Variable Speed-Controlled AC Machines

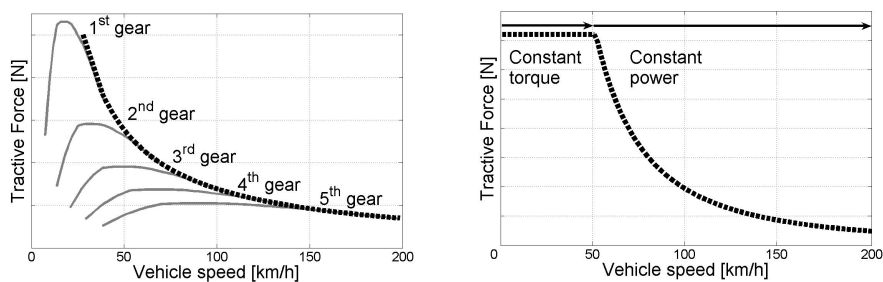
The first speed-controlled AC drives with sinusoidal excitation were synchronous machines, since early inverter topologies were not capable of handling reactive power. In 1930, the invention of the cycloconverter addressed this problem which enabled the use of AC machines in speed-control applications. Further developments, like the space vector theory for multi-phase AC motors by Kovács and Ràcz in 1959 finally improved the machine performance and allowed AC drives to be used in speed-controlled applications [PUR06].

However, these early drives were frequency controlled (u/f-control) only and offered poor dynamic behavior. In 1972, the German Felix Blaschke introduced the Field-Oriented Control method (FOC). He achieved significant improvements concerning the dynamic behavior of AC controlled drives by decoupling flux and torque building current components. Because the FOC method required - at that time - relatively large computing time, the Japanese Isao Takahashi and Toshihiko Noguchi and the German Manfred Depenbrock introduced almost si-

multaneously the Direct-Torque Control method (DTC) in the mid 1980s. The DTC method is based on the optimal choice of the stator voltage vector and is characterized by a high dynamic torque performance and the omission of coordinate transformation which is an essential part of the FOC method [PEI03]. Fast development in the field of microprocessors and the introduction of Application Specific Integrated Circuits (ASICs) in the early 1980s represent the basis for speed-controlled AC drives and pushed the use of electric motor types within automotive traction applications [PUR06].

3.2 Torque, Speed and Power Characteristics

Currently, several types of HEVs are being mass produced. Moreover, the start of production of pure electric vehicles (EV) is in progress or very close. The selection of a specific electric motor type in combination with its control strategy is a key enabling factor for these vehicles, as they mainly affect the overall power train efficiency. The electric motor as propulsion source has to meet predefined vehicle dynamic requirements which can be distinguished into acceleration, climbing and braking performance. In general, the propulsion power source has to provide high torque at low speed, at the same time, it needs to be capable of providing constant power at high speed ranges. The connection of each gear's point of maximum power of a conventional ICE results in a hyperbolic tractive force characteristic. The envelope of these forces represents all valid operation points of the vehicle. The controlled torque-speed profile of an electric motor type shows a significant similarity to the tractive power chart of a vehicle, see Fig. 3.1. Thereby, the motor control unit works as gear unit and provides continuous torque transmission. Thus, using an electric motor within a vehicle can eliminate the integration of a gear box.



a) Tractive power chart of a conventional vehicle. b) Torque-speed profile of a speed-controlled electric motor.

Figure 3.1: Comparison of the tractive power chart with the torque-speed profile of a speed-controlled electric motor. The characteristics of the tractive forces of both diagrams show a high similarity in case of powering.

Concerning the design of electric machines, there exist four characteristic design points, see Fig. 3.2. They need to be achieved in order to meet the predefined vehicle requirements. The sizing parameters are the rated torque T_n , the rated or base speed n_n , maximum speed n_{max} and maximum torque at start-up T_{su} and at maximum speed. The maximum torque is frequently known as pull-out torque T_{po} . The electric motor provides constant torque below base speed, therefore this region is called “constant torque” region. Due to the voltage limit of the energy source, the machine flux needs to be decreased above the base speed. As a consequence the rated torque decreases inversely proportional to the motor speed. The electric motor provides constant power within this region, hence, the operation range above base speed is denoted as “constant power” or “field weakening region”.

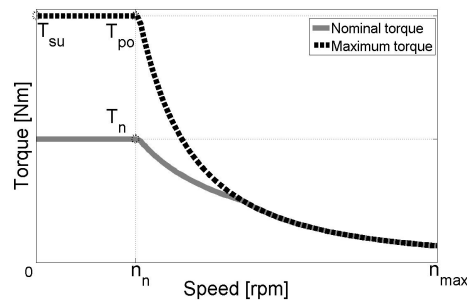


Figure 3.2: Representation of the characteristic machine design parameters.

3.3 Electric Machine Characterization

The individual suitability of a specific machine topology and its design strongly depend on the torque and therefore driver demand. The machine torque is a quadratic function of the diameter, as a consequence the main design parameter of an electric machine type concerning size and weight is its torque. Different machine topologies are generally characterized by different overload capabilities due to individual physical and thermal limitations. Moreover, a potential overload duration heavily depends on cooling restrictions and varies with the maximum allowed component temperatures.

The application and surrounding of the electric motor within the power train is of great interest, as a specific operation frequency within the operation range entails different energetic and thermal advantages and disadvantages. The operational losses of a machine topology result on the one hand from their different functional principles, on the other hand they can significantly be influenced by the control algorithms. Frequently operated load points should be characterized by a low torque ripple and low acoustic noise.

Different motor technologies require different system components. Therefore, a comparison of machine types has to consider the system including every stage of power flow. Focusing on the use of different electric machines within a specific vehicle topology, the electric machine has to provide essential design and operational features. The main characteristics are listed below, cf. [ZH07]:

- High torque density and low weight
- High efficiency across the full torque-speed profile
- High overload capability
- Wide speed range with a constant power range of around two to four times of the base speed
- High reliability, robustness and life-time
- Low acoustic noise
- Low production costs
- Low maintenance requirements

The following sections introduce the characteristics of different motor technologies for the use in automotive traction applications. Thereby, the analysis concentrates on sizing, control and fault tolerance issues showing the basic dependencies of sizing and operational features.

3.4 Assumptions

There exists a big variety of different machine topologies in literature. Each of them differs concerning assembling, design and operational features being suitable for different application scenarios. Chap. 3 concentrates on two different machine topologies - induction motors (IM) and permanent magnet synchronous motors (PMSM) having surface mounted magnets. From today's point of view, these motor topologies represent the most promising technologies concerning assembling, efficiency, noise and costs for automotive traction applications. An evaluation of their qualifications is given in App. A. For comparative purposes, App. B introduces a third machine topology - the switched reluctance machine (SRM).

Due to the fact, that both motor topologies are used as additional torque suppliers at a non-permanent-driven axle, the subsequent explanations will be given in terms of motor operation. The research work concentrates on three-phase systems only. Therefore, fault tolerance analysis of machines with higher phase numbers is beyond the scope of this work. Chap. 3 focuses on explanation of the basic relations concerning sizing and operational features at IMs and PMSMs. A detailed derivation and analysis of these characteristics is given in Chap. 4.

3.5 Induction Motors

Induction motors (IMs) are generally known because of their robustness, reliability and their well-established and relatively low cost assembling. In fact, they take the lead concerning quantity and business volume and represent the standard motor technology in industrial applications. In automotive applications, permanent magnet synchronous motors are mostly dominating. However, there can be observed a recent return to IMs since prices for rare earth magnets are going to increase rapidly [WK09].

For illustration purposes, Fig. 3.3 depicts the active machine components of a three-phase four-pole induction motor having three slots per pole and phase. Thereby, the slot conductors are given by a two layer winding topology. Due to the pole symmetry, the cross section of the sheet is given along a single pole pitch.

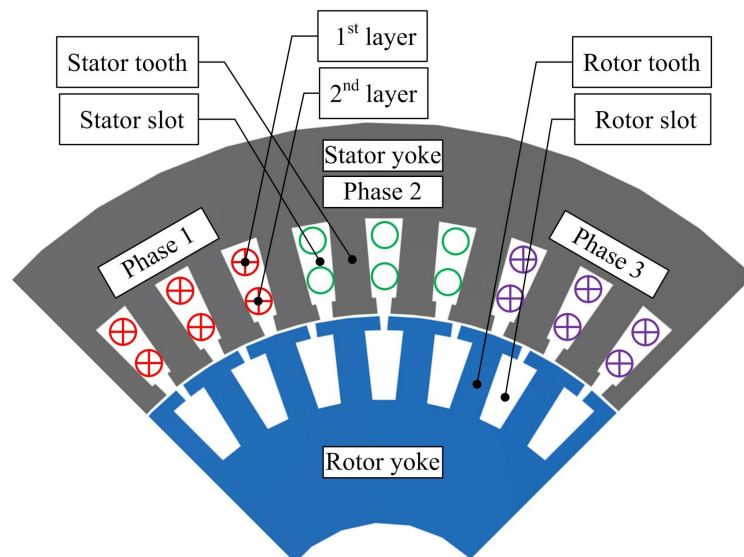


Figure 3.3: Representation of the active machine components of a three-phase four-pole induction motor.

3.5.1 Sizing

According to Fig. 3.2, the torque-speed profile of a speed-controlled motor drive is mainly affected by the characteristics of the nominal design torque T_n , the start-up torque T_{su} and the pull-out torque T_{po} over speed n . Considering the equivalent circuit diagram of an IM with a squirrel cage rotor, the torque output T is proportional to the supply voltage U_S and the stator flux linkage ψ_d . The

torque is inversely proportional to the angular slip frequency ω , the total stator and rotor reactance X_{SR} or the total stator and rotor leakage inductance per phase L_{SR} [ZH07] The corresponding equation reads

$$T \propto \frac{U_S^2}{\omega X_{SR}} \propto \frac{\psi_d^2}{L_{SR}}. \quad (3.1)$$

According to Equ. (3.1), the torque output T is higher, the lower the leakage inductance L_{SR} . Thus, stator and rotor slots should be designed and optimized in order to minimize L_{SR} . This generally favors the use of wide and relatively shallow rotor slots and parallel sided teeth. At the same time, focusing on the use of a voltage-source inverter, the amplitude of high-order harmonic currents is higher the lower the total leakage reactance X_{SR} . Therefore, a suitable leakage reactance should be chosen in order to meet the predefined performance and efficiency requirements.

The designed machines in Chap. 4 are supposed to be used within the wheel rim representing a restricted volume which basically constrains the motor design torque. In order to meet the predefined torque requirements, the in-wheel motors are designed to have a low leakage inductance. Conventional IMs at automotive traction applications typically have a constant power range or field weakening range of two to three times the base speed. However, long field weakening ranges are generally desirable [ERT97]. These ranges are mechanically limited by a characteristic overspeed reaching the maximum circumferential speed of the rotor. The ranges are operatively limited by the characteristic decline of the torque output as the supply voltage is limited. Therefore, in order to obtain wide speed ranges it is beneficial to minimize the leakage reactance X_{SR} .

The choice of pole pairs p has a great influence on the machine characteristics. In fact, the stator yoke can be made thinner at a higher number of pole pairs. Multi-pole IMs are characterized by smaller pole pitches τ_{pp} reducing the MMF along the iron core θ_{fe} and the electric loading A along the radial length of the air gap diameter d_δ . This causes the MMF of the air gap θ_δ and the air gap reluctance R_δ to become more dominant within the magnetic circuit:

$$\underbrace{\frac{1}{p} \int H_{fe} dl}_{\theta_{fe}} + \underbrace{\int H_\delta dl}_{\theta_\delta} = \underbrace{\frac{1}{p} \int A dl}_\theta \quad (3.2)$$

The air gap reluctance R_δ is specified by:

$$\theta_\delta = \frac{B_\delta}{\mu_0} w_\delta \quad (3.3)$$

$$\theta_\delta = \frac{w_\delta}{\mu_0} \frac{\phi_\delta}{\tau_{pp} l_{fe}} \quad (3.4)$$

$$R_\delta = \frac{w_\delta}{\mu_0 \tau_{pp} l_{fe}} \quad (3.5)$$

Choosing a high number of poles pairs might introduce magnetic problems, as the magnetizing inductance L_d decreases and the leakage becomes dominant. The analytic derivation of L_d is given in Equ. (4.98). The power factor $\cos(\varphi)$ of IMs is directly connected to the magnetizing inductance L_d and inversely proportional to the pole number squared. The equation reads

$$\cos(\varphi) \propto L_d \propto \frac{1}{(2p)^2}. \quad (3.6)$$

According to this, the number of pole pairs at IMs is limited to four [CWBR04]. The increased demand of magnetizing current I_d reduces their torque and force density and causes slight weight disadvantages compared to other machine technologies. There exists no characteristic torque density for IMs, however, IMs typically produce only 70 – 90% of the torque produced by a comparable synchronous motor with the same current [WZZC04]. The range of torque densities is large and need to be considered by the underlying optimization and cooling criteria. Nevertheless, high torque demands within restricted volumes are associated with higher losses representing a tradeoff between small package considerations and efficient motor designs.

3.5.2 Operation, Control and Acoustic Noise

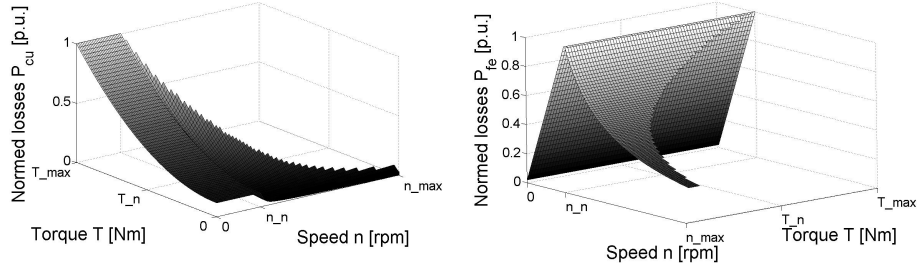
IMs produce iron and copper losses in stator and rotor, even though the iron losses within the rotor are generally low, see Fig. 3.4. Copper losses vary slightly with speed. However, they significantly increase at torques being higher than the design torque T_n - overload region - having an increase of the torque current component I_q . In contrast, iron losses are closely related to the supply frequency f , reaching a maximum at the base speed and decreasing within constant power range. An overload operation might affect the iron losses by a slight increase of the machine flux. The necessary machine flux ϕ_n needs to be induced by the magnetizing current I_d causing an increased stator current I_n at no-load. This lowers the power factor $\cos(\varphi)$ and requires a slight oversizing of the converter. Considering a machine's design point, the subsequent relations are valid

$$I_n = \sqrt{I_d^2 + I_q^2}, \quad (3.7)$$

$$P_{cu} \propto I_n^2, \quad (3.8)$$

$$P_{fe} \propto B^2 f_n. \quad (3.9)$$

One of the major advantages of IMs is their efficient performance at high speed applications. The flux reduction at constant power region causes the magnetization current I_d to shrink resulting in lower machine losses. Therefore, IMs show convincing efficiencies of 90% and more within this region. Another significant argument for the use of IMs is their good fail-safe behavior. No-load and short circuit of motor windings (three-phase, two-phase) represent uncritical motor states. In either case, there is no disturbing torque acting on the rotor shaft.

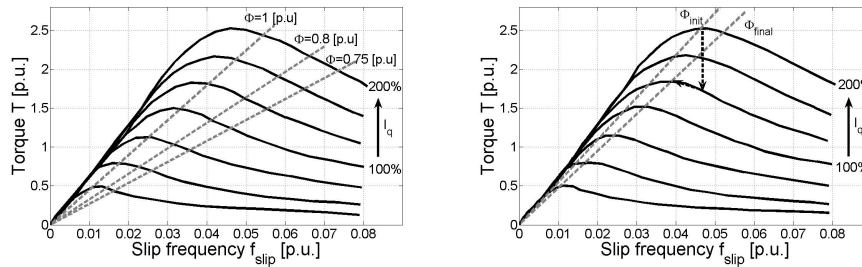


a) Stator copper losses.

b) Stator iron losses.

Figure 3.4: Normed copper and iron losses of an IM stator.

Operational optimization is one of the main issues at automotive traction drives. The optimizing process therefore concentrates either on the electromechanical design or on the operative influence of the torque output by the machine flux ϕ and the torque building current component I_q . The latter seems to be very attractive as existing motor dimensions do not necessarily have to be changed. The optimization criteria are different and need to be considered by the underlying motor requirements concerning efficiency and dynamic behavior. In case of high torque dynamics, the control will focus on maximum torque per stator ampere. This demand can be achieved by a constant flux control at constant torque region. Considering a constant flux level, a field oriented machine produces a torque which is linearly related to the slip frequency [NL96].



a) Constant flux control.

b) Variable flux control.

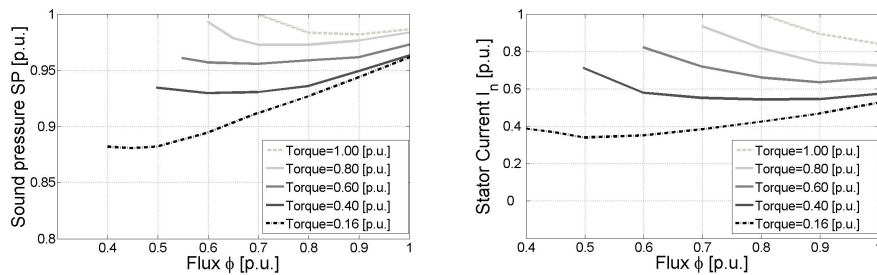
Figure 3.5: Comparison of different control approaches concerning efficiency. The operation strategies have opposing effects on machine efficiency and machine dynamics [NL96].

Fig. 3.5a shows the selection of flux level (dotted lines) for maximum torque per stator ampere. The flux lines should be selected to intersect the peak of the desired current (solid lines) at a maximum. The control approach focuses on short operation allowing to realize a minimum system reaction time. High dy-

dynamic motor requirements basically require higher saturation levels which cause the motor losses to increase. In contrast, high motor efficiency is characterized by continuous operation with minimal losses for given torque demands. Thus, the efficiency of IMs can be increased by a proper adjustment of the machine flux as a function of the load. Typically, this results in a flux reduction at part load condition having a flux level being proportional to the torque demand and inversely proportional to the speed [NL96]. Fig. 3.5b conveys two different flux and torque current levels for the same power output. Unfortunately, there is no general rule for the adjustment of machine flux and torque current, as these factors heavily depend on the MMFs of the motor.

Variable flux control can be associated with an individual adjustment of flux level for a given torque and speed. Indeed, computing time and dead time are higher compared to constant flux control which means that motor dynamics decrease and lack in case of high torque inputs.

The acoustic noise radiation is an individual characteristic of each machine and is strongly related to the mechanic design of the motor. However, it can significantly be influenced by a variable flux control at IMs. Takahashi and Noguchi observed a 10dB to 15dB noise reduction measured at an unloaded motor which was operated under 33% of the rated flux level ϕ_n [XZH00a]. Therefore, the optimal flux level for the lowest noise emissions increases with the load [ZH07]. This statement can figuratively be seen in Fig. 3.6a. Secondly, the flux levels causing minimum losses need not necessarily be the same as for the lowest noise emissions. According to Fig. 3.6, this discrepancy becomes obvious by comparing the corresponding flux levels for minimum sound pressure and minimum stator current.



a) Sound pressure [XZH00b].

b) Stator current [XZH00a].

Figure 3.6: Comparison of sound pressure and stator current at different loads.

3.5.3 Fault Tolerance

Electromagnetic faults which may occur in IMs can be classified by (i) winding open circuit, (ii) winding short circuit (phase-ground or within the phase) or

(iii) winding short circuit at the terminals.

Basically, fault tolerance means that the machine is capable of continuing its operation in case of any fault incidence. System efficiency is typically reduced at faulted operation, since it represents an unusual operating condition. Motor losses are assumed to be of secondary concern as long as the motor drive is thermally stable. Having a three-phase machine, the copper losses are highly effected under unbalanced two-phase operation, as they can easily reach twice the value compared to healthy state condition [LFL93]. Providing low machine losses requires an almost sinusoidal MMF distribution. This can be achieved by the use of more than one slot per pole and phase, $q > 1$ [LEV08]. Concentrated winding topologies are considered to have $q < 1$, therefore, three-phase IMs are normally designed to have a distributed stator winding providing an almost sinusoidal MMF distribution with sinusoidal phase currents.

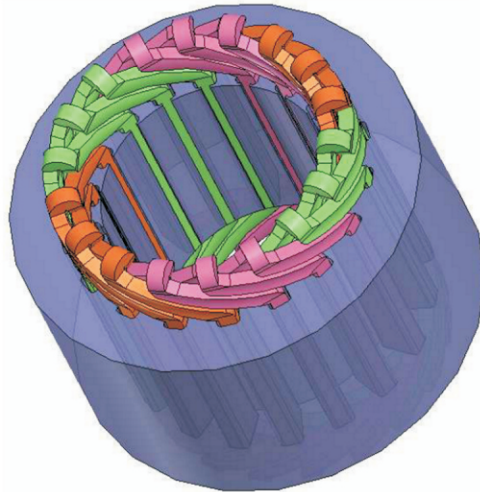


Figure 3.7: Distributed two-layer winding topology induction machines [ST05].

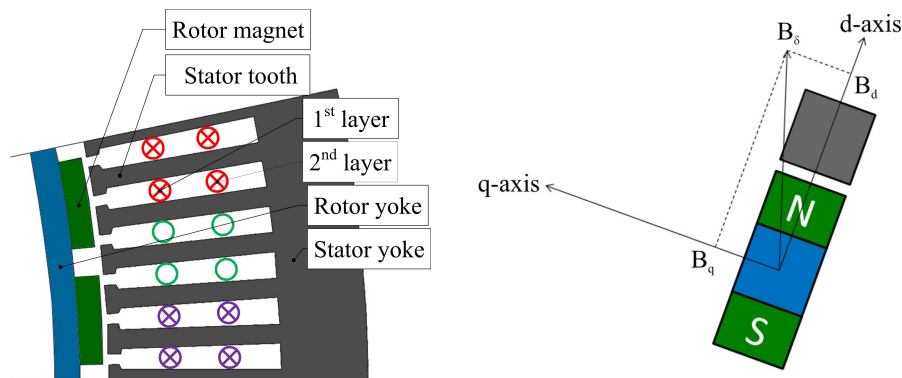
The distributed phase windings of an IM are closely, mutually coupled and therefore not inherently tolerant of motor winding faults. Considering star connected three-phase machines without a neutral connection, open circuit faults of phases would result in high pulsating torques since the motor would have only one controllable phase current left. The starting torque capability can still be maintained if the neutral point is joined to the mid point of the DC link of the inverter drive. In fact, this allows to adjust two independent phase currents required to produce a rotating magnetic field if the rotor is stationary [GBS⁺04]. The number of phases m is related to the reliability and system stability of the motor drive. Therefore, the higher the phase number m , the lower the reduction of the MMF θ in case of a fault for the same phase currents. Achieving the same torque output as in a healthy condition leads to inevitably to higher phase

currents which might endanger the machine due to overtemperature.

Considering a winding short circuit, the back-EMF driven fault current will be limited by the resistance and the inductive reactance of the shortened turns. The air gap flux is reduced once due to a fewer number of effective turns and once by the opposing MMF generated by the shortened windings. This leads to the fact that the torque building current component I_q will gradually increase for providing a constant torque output. Generally, the larger the number of shortened windings, the higher the air gap flux reduction and the lower the fault current [GBS⁺04].

3.6 Surface Permanent Magnet Synchronous Motors

During the last decades, permanent magnet synchronous motors (PMSM) have become one of the major favorites in automotive propulsion, as they convince by their extraordinary high efficiencies. The first concept was introduced by Wilson and Trickey in 1962. The motor had a classic three-phase stator and a rotor with surface mounted magnets producing a rectangular air-gap flux distribution [WZZC04].



a) Active machine components.

b) Magnetization directions.

Figure 3.8: Active machine components and a rotor fixed coordinate system along different magnetization directions.

Fig. 3.8a represents the active machine components of a three-phase synchronous machine having two slots per pole and phase and a two layer winding topology. For illustration purposes, Fig. 3.8b introduces a rotor fixed coordinate system. Three-phase values are thereby reduced on two operation values being orthogonal to each other. The positive d-axis points along the main magnetization

direction of a north pole, the corresponding q-axis is shifted by an electric angle of $\frac{\pi}{2}$ [BOU07].

3.6.1 Sizing

The electromagnetic torque output T results due to the interaction of the phase back-EMFs U_p and phase currents I . The torque T is proportional to the supply voltage U_S and inversely proportional to the angular frequency ω and the d-axis inductance L_d . Considering two different torque parts being either dependent (T_s) or independent (T_r) of the flux linkage, the following torque dependencies can be given [RIE06]

$$T \propto \frac{U_S U_p}{\omega^2 L_d}, \quad (3.10)$$

$$T = \frac{3}{2} p \left(\underbrace{\psi_d I_q}_{T_s} - \underbrace{(L_q - L_d) I_d I_q}_{T_r} \right), \quad (3.11)$$

where ψ_d is the flux linkage between the stator winding and the rotor magnets. The variables L_d, L_q and I_d, I_q are the inductances and currents along the main magnetization direction (d-axis) and the 90° shifted axis (q-axis) respectively. According to Equ. (3.11), the torque output can be enhanced by either increasing ψ_d or the inductance difference $L_q - L_d$. This can basically be done through a reduction of the leakage flux by means of flux focusing. Flux focusing techniques are a thing of their own, representing another sensitive design issue for PMSMs having interior mounted magnets. As the subsequent content concentrates on PMSMs having surface mounted magnets, flux focusing is not of prime interest. Flux focusing is therefore not commented furthermore¹. The inductance difference $L_q - L_d$ represents a further important design and optimization parameter. In case of a high torque output, meaning high overload capacity, the objective is to achieve a low L_d inductance. In contrast, long constant power ranges focus on a high L_d and a low L_q inductances providing significant reluctance torque caused by the flux weakening current component. In fact, an increased d-axis inductance L_d can be achieved by providing flux guides for the d-axis flux, hence a low L_q can be achieved by providing airspace flux barriers or interpole magnets and vice versa [SMW93]. The saliency ratio² ζ is a well known parameter for the quantification of L_d and L_q . The corresponding equation reads:

$$\zeta = \frac{L_d}{L_q} \begin{cases} \text{surface mounted} & 0.8 - 0.9 \\ \text{inset mounted} & > 1 \end{cases} \quad (3.12)$$

¹Information on this subject is given in [MVP08].

²The values were given in [PUR06].

Classification

PMSMs having surface mounted magnets can be realized by either directly fixing the magnets on the rotor surface or having them inset. This classification is very useful as the location of the magnets has an impact on the inductance and therefore on the overload capacity of the motor. The relative permeability of modern rare earth magnets, such as Neodymium-Iron-Boron (NdFeB) is only slightly above unity, as a consequence the air-gap width becomes very long at PMSMs with affixed magnets. This makes the d-axis inductance smaller, which has a substantial effect on the motor's overload capability. As the pull-out torque T_{po} is inversely proportional to L_d , this rotor configuration shows a high maximum torque, cf. Equ. (3.10). Thereby, the pull-out torque is typically in the range of 4p.u. to 6p.u., which is quite impressive and advantageous for a compact motor design [PUR06].

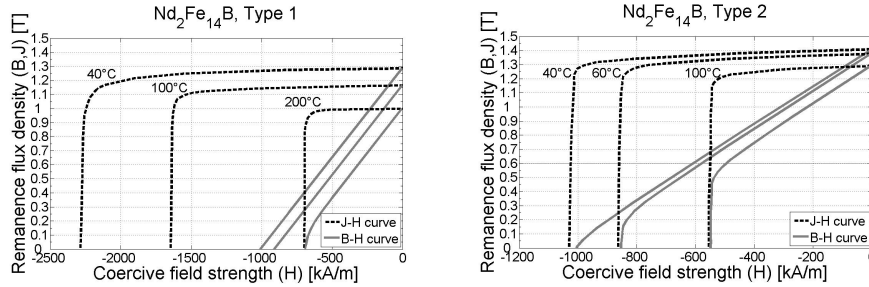
PMSMs having inset mounted magnets naturally have a higher d-axis inductance L_d which might be useful for higher speed applications. Therefore, the pull-out torque capability of this rotor configuration is considerably lower compared with PMSMs having affixed magnets and varies according to the design. However, it need to be at least 1.5p.u. according to the standard IEC60034 – 1 given in [OVE04a].

Magnet Material

NdFeB is a commonly known magnet material which is primarily used at high efficiency drives in automotive applications. The specific energy product BH_{max} represents the stored energy within a magnet volume and is proportional to the product of remanence flux density B_r and coercive field strengths H_c . In practice, NdFeB magnets have energy products up to $400 \frac{\text{kJ}}{\text{m}^3}$, which basically allow very compact motor design variants [PJHN08]. The major limitation concerning the application of NdFeB is its limited temperature tolerance and its corrosion sensitivity. They normally are very brittle which makes them very sensitive to mechanical shocks or tensile stress. While the Curie temperature of NdFeB materials is about 300°C , its maximum operating temperature is considerably lower and limited to about 200°C depending on the composition technique. [RS85]. However, today's commercial available NdFeB magnets have a remanence flux density B_r of 1.5T, nonetheless, their maximum operating temperature limit is below 100°C [PUR06].

Magnet warming decreases the remanence flux density which immediately leads to a current increase for a given torque output. However, excessive machine warming will probably lead to permanent damages of the rotor. The magnetization curves of magnets show a significant decrease of the coercive field strength H_c at increasing magnet temperatures, see Fig. 3.9. Hence, the inflection point, meaning a rapid sag of the remanence flux density, comes very close to the operating point. A possible excess of the opposing field of the coercive field strength

produced by the magnetic circuit and the magnetizing electric loading A_d needs to be prohibited. This could eventually cause an irreversible demagnetization of the magnets.



a) The type 1 magnet can be operated up to 200°C. A 60°C temperature increase leads to a flux density decrease of 10%.

b) Type 2 magnet is supposed to be operated below 100°C. A 20°C temperature increase results in 10% flux density reduction.

Figure 3.9: NdFeB magnets are typically operated in the second quadrant having negative currents. The inflection point of the $J - H$ curve characterizes the operating point at which the polarization J is irreversibly lost.

3.6.2 Operation, Control and Acoustic Noise

As far as the stator is concerned, PMSMs have copper and iron losses. Their specific characteristic is quite similar to those of IMs shown in Fig. 3.4. However, the rotor losses are different as there are no copper losses. The iron losses tend to be very small. They mainly arise due to air-gap permeance harmonics which induce eddy currents on the rotor iron sheet and on the magnet material. Although these losses are very small, they might cause a significant heating of the magnets. The electric conductivity of NdFeB is only a tenth compared with iron, as a consequence eddy currents may have a serious impact on the losses and therefore on the magnet temperature. It is particularly important to consider rotor eddy current losses at highly utilized PMSM drives having a high number of pole pairs p , high stator slot openings and whose windings span a fractional pole pitch with nearly equal pole and slot numbers [IZH05].

PMSM are generally classified according to their back-EMF waveform, being either sinusoidal or trapezoidal. Furthermore, they can be classified according to their control strategy. Brushless DC (BLDC) drives have almost rectangular phase currents commutated properly to the flat portion of the trapezoidal back-EMF. Brushless AC (BLAC) drives have sinusoidal phase current waveforms [ZSH06]. In order to maximize a machine's torque density and to minimize its torque pulsations, PMSMs with trapezoidal back-EMF are frequently

operated in BLDC mode. PMSMs with sinusoidal back-EMF are mostly operated in BLAC mode [ZH07]. Mainly due to the phase current waveforms, BLDC drives are known to have higher harmonic content. Therefore, acoustic noise reduction mostly considers this kind of control strategy. There are quite a lot of reasons to cause vibrations and acoustic noise in a motor drive system. However, examining the motor itself, torque ripples are the main reason. Torque ripples consist of two main components - cogging torque and electromagnetic torque fluctuation [LYJ08]. Cogging torque results due to the interaction of the permanent magnets and the slotted iron structure of the stator. It manifests by the tendency of the rotor to align itself in a stable position even when the machine is not energized. There are many publications on cogging torque reduction in literature - like stator teeth notching³ or stator teeth pairing⁴. Information on these issues is given on the corresponding footnotes. Electromagnetic torque fluctuation is caused by mismatches between of the back-EMF and the phase currents associated with the motor dynamics. Generally speaking, the noise amplitude is not only related to the torque ripples, but also in close relation to the mechanical system resonance frequency. Therefore, the noise radiation becomes higher at a higher matching of torque fluctuation and system resonance frequency [LYJ08].

Having a look on the individual operation ranges, PMSMs show a relatively high efficiency within the constant torque region ($n < n_n$). Due to the permanent excitation of the rotor, the flux building current component I_d is very low resulting in a high power factor $\cos(\varphi)$. A high portion of the stator current I can be used directly for the torque output T . This advantage reverses when entering the constant power region ($n > n_n$). The machine flux ϕ needs to be decreased complying with the voltage limit of the intermediate circuit. Contrary to constant torque region, the flux weakening requires an additional current component I_d causing the machine efficiency to decrease. Considering a given stator current I , the torque building current I_q decreases with higher speeds. Higher speed ranges therefore mean high demagnetization currents I_d resulting in bad machine efficiencies. The maximum flux weakening capability could be achieved when PMSMs are designed to have a 1p.u. d-axis inductance L_d [SL88],

$$\frac{L_d I_n}{\psi_d} = 1. \quad (3.13)$$

A relation of one would theoretically result in an infinite flux-weakening capability. In fact, for most PMSMs, the relation $\frac{L_d I_n}{\psi_d}$ is smaller than 1 since the d-axis inductance is relatively low due to the permeability of the magnets itself being approximately equal to 1. A potential increase of the flux-linkage ψ_d would result in a higher peak torque at constant torque region but a lower flux-weakening capability. However, the higher the ratio given in Equ. (3.13), the higher the flux-weakening capability. Considering a specific current, the flux linkage ψ_d needs either to be lowered or the d-axis inductance L_d is increased.

³Information on this subject is given in [ZWS07].

⁴Information on this subject is given in [ZBL08].

3.6.3 Fault Tolerance

Short-circuit faults at PMSMs may have serious impacts on their fault tolerance, since the control of phases gets disabled. Alternating torques arise which are strongly related to the short-circuit fault current I_{sc} . Fault currents are limited by the phase reactance X_S and phase resistance R_S . Hence, achieving limited fault currents requires a machine design with a large leakage inductance L_{SR} by controlling the depth and width of the slot opening [JMH96]. Therefore, the slot depth is designed to be approximately one half of the tooth width, with the slot width chosen according to the required inductance. The per-phase synchronous reactance should be typically higher than 1p.u., which means the short-circuit current I_{sc} under a single-phase fault is not greater than the rated phase current I_n [AT09].

A low magnetic isolation causes faulted currents in phases to induce large interference voltages in other phases which makes an adequate control of them more complicated. Hence, a further requirement concerning fault tolerant motor operations is a low mutual coupling between the phases. Unlike IMs, three-phase PMSMs - mostly BLDC drives - are frequently designed to have concentrated windings. Concentrated winding topologies might mitigate this problem since each winding is placed around one single tooth, see Fig. 3.10. Not only the possibility of a phase to phase fault is reduced by this physical separation but also the mutual coupling between the phases is low. Besides that, a physical separation of windings ensures a good thermal isolation between the phases. A higher thermal isolation can be achieved if each slot contains only a single phase. In fact, every slot remains fully filled, the remaining teeth without coils are still utilized as flux return paths [MJHC96].

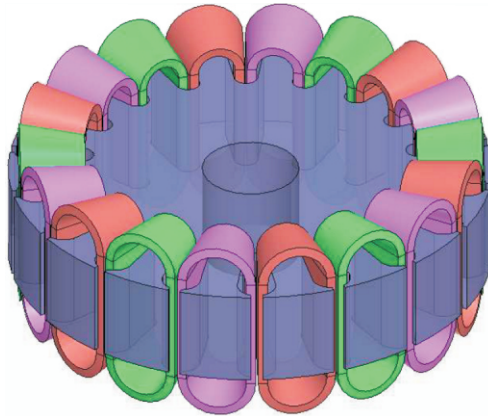


Figure 3.10: Concentrated winding topology for a low mutual coupling between the individual phases [ST05].

Considering open-circuit conditions, iron losses must be limited as they might cause thermal problems. In this case, pulsating braking torques arise which are related to the machine parameters. Therefore, it is desirable to have a low magnet flux linkage ψ_d and a high ratio of $\frac{L_q}{L_d}$ [WJH02].

4

AC Motor Design

Chap. 4 gives a more detailed description of the basics of the implemented design methodology (DM) for a fast and reliable computation and evaluation of IMs and PMSMs with surface mounted magnets. According to Fig. 1.2, the introduced DM takes the VDI model as a basis and concentrates on “Domain Specific Optimization” issues of electric machines. The first part of the chapter introduces generally accepted fundamental design parameters representing the basis for the introduced design approach. The second part of the chapter concentrates on the introduction of the DM exemplified by the sizing of an air-cooled IM and PMSM. The content emphasizes the individual choice of design parameters for the machines used as in-wheel motors at the rear axle.

4.1 Design Fundamentals

The design process is generally known to be an iterative process. It tries to handle geometric, operational and dynamic requirements on the one hand, costs, thermal and fail-safe behavior on the other hand. The first stage of the design process aims at the estimation of the basic geometric dimensions under predefined design conditions. A second design stage considers additional design criteria such as thermal restrictions or motor control aspects. In all cases, unwanted thermal warming of the active machine components needs to be avoided. One of the major sizing parameters concerning the thermal utilization of an electric machine is its corresponding current sheet or electric loading.

4.1.1 Current Sheet and Electric Loading

Considering the limiting case of infinitely small slots, the slot current can be depicted by a current sheet along the stator area. This current sheet is generally known as electric loading A and is strongly related to the cooling condition and the main size of the motor. The electric loading A can be considered by a magnetizing component A_d and a torque building component A_q and varies within a range of $20 \frac{\text{kA}}{\text{m}}$ to $60 \frac{\text{kA}}{\text{m}}$ for a three-phase machine [FIS06]

$$A = \sqrt{A_d^2 + A_q^2}, \quad (4.1)$$

$$\underbrace{20 \leq A \leq 60}_{\text{air} \rightarrow \text{water}} \left[\frac{\text{kA}}{\text{m}} \right]. \quad (4.2)$$

The phases of a motor are locally displaced by an angle φ_p , the time displacement is determined by the angle φ_t . Phase current and electric loading are physically related to each other by the stator area of one phase [BIK99]. The variables read

$$\varphi_p = \frac{2\pi}{mp}, \quad \varphi_t = \frac{2\pi}{m}, \quad \varphi_e = p\varphi_m, \quad (4.3)$$

$$i(t) = \sqrt{2}I \cos(\omega t + \varphi). \quad (4.4)$$

The electric angle φ_e over a pole pitch is known to be 180° , thus, the pole pair number p specifies the relation between the electric angle φ_e and the mechanical angle φ_m . The spatial and time depending electric loading A of an m phase motor drive can be given by:

$$\begin{aligned} A(\varphi_m, t) &= \sum_{\nu=1}^{\infty} \frac{2m\omega_{ph}\sqrt{2}I}{d_\delta\pi} \xi_w \cos(\nu p\varphi_m - \omega t - \varphi) \\ &= \sqrt{2}A\xi_w \cos(\varphi_e - \omega t - \varphi)_{\nu=1} \end{aligned} \quad (4.5)$$

The insertion of single conductors into different slots and layers basically results in a discrete distribution of the electric loading, which may cause higher order losses and parasitic torques. A reduction of these effects can be achieved by an adequate choice of the slot pitch τ_{sp} and the coil pitch τ_{cp} respectively. Having a discrete electric loading, the fundamental wave and the higher order waves face a distribution factor ξ_d , mainly depending on τ_{sp} and a chord factor ξ_c , strongly related to τ_{cp} . The winding factor ξ_w , shown in Equ. (4.5), is defined by

$$\xi_{w\nu} = \xi_{d\nu}\xi_{c\nu}. \quad (4.6)$$

The winding factor $\xi_{w\nu}$ is a design related winding parameter reflecting the correlation of a field wave with the induced phase voltage in the stator. In case of a high electromagnetic utilization of the machine (cf. Sec. 4.1.3), the winding factor of the fundamental should be very close to one, $\xi_{w\nu} \rightarrow 1$. Achieving a low harmonic content it is desirable to have $\xi_{w\nu} \rightarrow 0$.

Distribution Factor

Considering Q_S numbers of stator slots, there is a slot angle α_{sl} between two neighbored slots corresponding to the slot pitch $\tau_{sp} = \frac{2\pi}{Q_S}$. This angle causes the slot currents to be summed up time-delayed reducing the magnitude of the electric loading A . The distribution factor ξ_{dv} can be given in case of a single or double layer winding with a constant zone angle of $q\alpha_{sl}$ by [VOG88]:

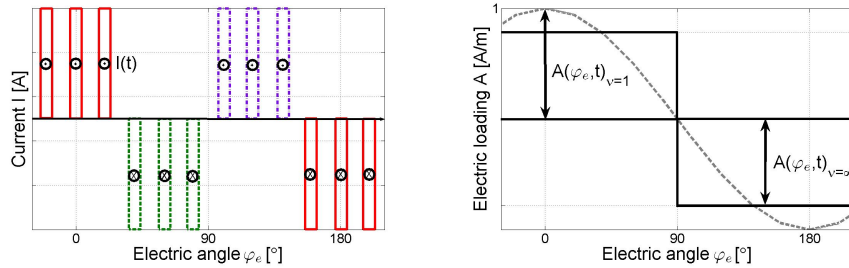
$$\begin{aligned} \alpha_{sl} &= p\tau_{sp} \\ \xi_{dv} &= \frac{\sin(q\nu\frac{\alpha_{sl}}{2})}{q\sin(\nu\frac{\alpha_{sl}}{2})} \end{aligned} \quad (4.7)$$

Chord Factor

The effect of the chord factor ξ_{cv} is very similar to that of the distribution factor. It considers the difference between the coil pitch τ_{cp} and the pole pitch τ_{pp} , which may result in a reduction of higher order losses. However, the magnitude of the electric loading decreases in case of $\tau_{cp} < \tau_{pp}$. The chord factor ξ_{cv} is a function of the mentioned variables τ_{cp} and τ_{pp} and is specified by [VOG88]:

$$\xi_{cv} = \sin\left(\nu\frac{\tau_{cp}\pi}{\tau_{pp}2}\right) \quad (4.8)$$

Fig. 4.1 depicts a single layer winding with three slots per pole and phase ($q_S = 3$) having a chord factor of one. The height of the bars conveys the existing phase current amplitudes (Fig. 4.1a), the corresponding electric loading A together with its sinusoidal fundamental wave is shown in Fig. 4.1b.



a) Phase currents.

b) Electric loading.

Figure 4.1: Illustration of a single layer winding with three slots per pole and phase ($q_S = 3$) and the corresponding electric loading A .

Considering RMS values of Equ. (4.5), the relation between the current and the electric loading results in [MVP08]

$$A = \frac{2m\omega_{ph}I}{\pi d_\delta} = \frac{m\omega_{ph}I}{p\tau_{pp}}, \quad (4.9)$$

where $2m\omega_{ph}$ denotes the total number of serial connected conductors and τ_{pp} represents the stator pole pitch of the motor. The number of turns per phase ω_{ph} is mainly determined by the induced phase voltage, the supply frequency f_n and the machine flux ϕ_n .

4.1.2 Magnetomotive Forces and Air Gap Fields

The appearance of electric and magnetic fields is based on the fundamental equations of electrostatics and magnetostatics, known as Maxwell equations. There is an easier approach giving a relation between electric and magnetic characteristics - ‘‘Ampère’s Circuit Law’’. In order to give a short insight on the basic principles, a simplified magnetic circuit is assumed in form of a C-shaped iron core. The iron core is supposed to have constant cross sections and is constantly excited by a conductor loop on the opposite side of the air gap. Thus, having constant flux densities, the MMF θ can be given by means of two different magnetic potential differences shown by Equ. (4.10). The main path of integration is right in the middle of the cross sections and consists of the air gap distance x_δ and the distance through the iron core x_{fe} . The variables \hat{B}_δ and \hat{B}_{fe} denote the peak values of air gap flux density and the iron cores flux density respectively.

$$\begin{aligned} \theta &= \oint_x H \cdot dl = \theta_\delta + \theta_{fe} \\ &= \frac{\hat{B}_\delta}{\mu_0} x_\delta + \frac{\hat{B}_{fe}}{\mu_0 \mu_{fe}} x_{fe} \end{aligned} \quad (4.10)$$

Basically, there are two different ways of generating MMFs. Focusing IMs, MMFs arise due to the magnetizing electric loading A_d . This may even be the case at PMSMs, however, they mostly generate MMFs by their magnets. In fact, Equ. (4.11) is equally valid for both motor topologies. The right side of Equ. (4.11) considers the magnetizing electric loading A_d along the radial length l_δ of the air gap diameter d_δ . The electric loading A_d can either be field building (IM, PMSM) or field weakening (PMSM).

$$\theta = \oint_x H \cdot dl = \int_{d_\delta \pi} A_d \cdot dl_\delta = r_\delta \int_{2\pi} A_d \cdot d\varphi_m \quad (4.11)$$

Substituting Equ. (4.5) into Equ. (4.11), the spatial and time dependent MMF results in

$$\begin{aligned}\theta(\varphi_m, t) &= r_\delta \sum_{\nu=1}^{\infty} \sqrt{2} A \frac{\xi_{w,\nu}}{p\nu} \sin(p\varphi_m - \omega t - \varphi), \\ \theta(\varphi_m, t) &= \sqrt{2}\theta \sin(\varphi_e - \omega t - \varphi)_{\nu=1}, \quad \theta = \frac{r_\delta}{p} A \xi_w,\end{aligned}\quad (4.12)$$

where θ represents the RMS value of the MMF. Equ. (4.12) assumes an ideal permeance of the iron sheet, meaning $\mu_{fe} = \infty$, which causes the magnetic potential difference θ_{fe} of Equ. (4.10) to be zero. In fact, the total MMF is located in the air gap. Considering Equ. (4.10) to Equ. (4.12), the air gap flux density B_δ can now be given by Equ. (4.13).

$$\begin{aligned}B_\delta(\varphi_m, t) &= \frac{\mu_0}{2\delta} \sqrt{2}\theta \sin(p\varphi_m - \omega t - \varphi)_{\nu=1} \\ &= \sqrt{2}B \sin(\varphi_e - \omega t - \varphi), \quad B = \frac{\mu_0}{2w_\delta} \theta\end{aligned}\quad (4.13)$$

Equ. (4.13) describes the air gap flux density B_δ generated by the electric loading A of the motor. In fact, it reflects the magnetic excitation of an IM. The derivation of the air gap flux density of PMSMs differs from the previous example, as the computation of the MMF considers an additional component $\theta_m = H_m h_m$ depending on the magnetic excitations H_m and the heights h_m of the magnets.

4.1.3 Electromagnetic Utilization

The derivation of the electric loading A depending on the current waveform was shown in Sec. 4.1.1. The electric loading A of a motor can also be explained by the slot geometry, the slot pitch τ_{sp} and the current density J_{cu} of the winding material. Assuming a rectangular stator slot, the electric loading A results in

$$A = k_{sl} J_{cu} h_{sl} \frac{w_{sl}}{\tau_{sp}} = \underbrace{\sqrt{k_{sl} A J_{cu} \frac{w_{sl}}{\tau_{sp}}}}_{\text{constant}} \underbrace{\sqrt{h_{sl}}}_{\text{variable}}, \quad (4.14)$$

where k_{sl} denotes the slot fill factor, J_{cu} is the copper current density and h_{sl} and w_{sl} represent the slot height and the slot width respectively [MUE94]. The slot pitch τ_{sp} describes the lengths of one slot-tooth combination. The slot fill factor $k_{sl} = \frac{J_{sl}}{J_{cu}}$ is defined as the relation between slot current density and copper current density. The first factor of Equ. (4.14) is more or less constant assuming a predefined slot pitch and a constant product of $A J_{cu}$ (Equ. (4.15)). This product characterizes the electric utilization of the motor and is strongly related to the cooling conditions. The second factor reflects the basic geometric dependency of the electric loading $A \propto \sqrt{h_{sl}}$. Therefore, the higher the slot height h_{sl} , the higher the allowable current loading A . In case of copper windings, it can be

given within the following range [VOG88]:

$$\underbrace{100 \leq AJ_{cu} \leq 300}_{\text{air} \rightarrow \text{water}} \left[\frac{\text{kA}}{\text{m}} \frac{\text{A}}{\text{mm}^2} \right] \quad (4.15)$$

The magnetic utilization is related to the cross sections of the magnetic parts. In fact, the cross sections have to have a suitable dimension in order to prevent unwanted high local flux densities along the flux path. Considering a given slot pitch, the flux ϕ_t needs to pass one tooth. As a consequence, the tooth flux density is higher by the factor of $\frac{\tau_{sp}}{w_t}$ compared to the local air gap flux density B_δ . Tooth flux densities higher than 2.2T lead to high magnetic field strengths and therefore high MMFs. Indeed, this causes air gap flux densities B_δ to be within 0.5T to 1.1T [MUE94].

$$A_{fe} = k_{fe} w_{fe} l_{fe} \geq \frac{\phi}{B_{max}} \begin{cases} B_{t,max} & = 2.2\text{T} \\ B_{\delta,max} & = 1.1\text{T} \\ B_{y,max} & = 2.0\text{T (Stator)} \\ B_{y,max} & = 1.8\text{T (Rotor)} \end{cases} \quad (4.16)$$

The variable k_{fe} denotes the iron fill factor, w_{fe} and l_{fe} represent the iron width and the stack length respectively. Stator yoke flux densities may be up to 2.0T, rotor yoke flux densities are up to 1.8T [MUE94] [HUB11].

The nominal output torque is influenced by two parameters, the air gap radius r_δ and the mean shear force density σ_n . Therefore, the force density σ_n represents the mean force F_δ across the active area (Sec. 4.1.4) and describes the relation between the air gap diameter d_δ , and the product of the q-component of the electric loading A_q and the air gap flux density B_δ ,

$$\sigma_n = \frac{F_\delta}{d_\delta \pi l_{fe} k_{fe}} = \frac{1}{2} \hat{A}_q \hat{B}_\delta. \quad (4.17)$$

Similar to Equ. (4.15), shear force densities are tightly coupled with the existing cooling conditions. Known from experience, air cooled motors allow shear force densities up to approximately $13 \frac{\text{kN}}{\text{m}^2}$. Water cooled motor types allow much higher force densities, which may reach $30 \frac{\text{kN}}{\text{m}^2}$ for jacket cooling and $50 \frac{\text{kN}}{\text{m}^2}$ for direct winding cooling.

$$\frac{P_i}{n} = C_u d_\delta^2 l_{fe} k_{fe} \Rightarrow C_u = \frac{P_i}{d_\delta^2 n l_{fe} k_{fe}} = \pi^2 \sigma_n \quad (4.18)$$

Equ. (4.18) introduces the inner power P_i and the utilization factor C_u of a motor. Thus, the air gap diameter d_δ has squared influence on the corresponding torque, given by the first part of Equ. (4.18). The nominal torque T_n of a motor is the dominant characteristic concerning, size, volume and weight. The utilization factor C_u describes the electromagnetic utilization of the material, see Fig. 4.2.

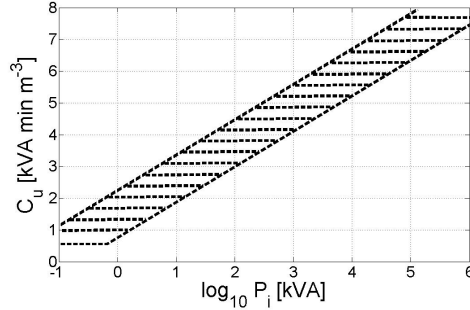


Figure 4.2: Utilization factor C_u for all motor types as a function of the inner power P_i . The factor represents a mean value, neglecting extremely bad and extremely good cooling [MUE94].

As this factor is mainly determined by the electric loading A , the utilization factor C_u is strongly related to the machine size and the cooling methods.

Designing highly utilized motors basically results in relatively small motor dimensions. This causes current densities $J_{al,cu}$ and flux densities $B_{t,y}$ to be on upper ranges of technical feasibility. As copper and iron losses increase with the square of $B_{t,y}$ and $J_{al,cu}$ respectively, the efficiency decreases rapidly. Therefore, a tradeoff between high utilization at small motor sizes and high efficiency at bigger motor sizes exists.

4.1.4 Lorentz Force and Torque Development

Electric motor types are based on the physical fact that electric charge moving within a magnetic field is effected by forces, called Lorentz forces. Static charge is not affected. There exists a well defined relationship between the electric charge I , the air gap flux \mathbf{B}_δ and the resulting Lorentz force \mathbf{F}_δ . The force \mathbf{F}_δ is perpendicular to I and \mathbf{B}_δ , its action can be given by the right-hand rule. The equation reads:

$$\mathbf{F}_\delta = I (\mathbf{l}_{fe} \times \mathbf{B}_\delta) \quad (4.19)$$

The electric charge transmits the force onto the surface of the conductor being moved towards the air gap. Combining Equ. (4.9) and Equ. (4.19) the differential Lorentz force $d\mathbf{F}_\delta$ results in

$$d\mathbf{F}_\delta = A r_\delta d\varphi (\mathbf{l}_{fe} \times \mathbf{B}_\delta), \quad (4.20)$$

$$d\mathbf{T} = \mathbf{r}_\delta \times d\mathbf{F}_\delta. \quad (4.21)$$

Assuming a sinusoidal current waveform (Equ. (4.4)) of the electric loading A and the air gap flux density B_δ , the effective torque output T of the motor can

be expressed as follows [BIK99]:

$$\begin{aligned}
T(t) &= \int_0^{2\pi} d\Gamma d\varphi_m \\
&= 2B_\delta Ar_\delta^2 l_{fe} \int_0^{2\pi} \cos(p\varphi_m - \omega_1 t - \varphi_1) \cos(p\varphi_m - \omega_2 t - \varphi_2) d\varphi_m \\
&= 2\pi B_\delta Ar_\delta^2 l_{fe} \cos(\underbrace{\omega_2 t + \varphi_2}_\alpha - \underbrace{(\omega_1 t + \varphi_1)}_\beta)
\end{aligned} \tag{4.22}$$

Equ. (4.22) shows that the torque output T can be given by the inner product of the air gap flux density $B_\delta = f(\omega_2, \varphi_2)$ and the electric loading $A = f(\omega_1, \varphi_1)$. It is maximal if the difference between the angles (α, β) is minimal. Moreover, the torque output is constant if ω_1 equals ω_2 .

4.1.5 Loss Characterization and Computation

According to [OVE04b], electric motors have several loss sources which can basically be divided into current dependent and current independent losses. The latter consist of iron losses P_{fe} , bearing losses and air friction losses. Current depending losses denote copper losses P_{cu} in stator windings (IM, PMSM) and the rotor windings (IM). PMSMs do not have any copper losses in the rotor, the rotor iron losses are comparatively small. In fact, there exists a third loss part known as supplementary load losses. These losses represent an overall summary of losses due to eddy currents, high-order harmonics and the electric commutation.

In order to ease the subsequent considerations, the losses of the active machine parts are given in per-unit form. The equation for the stator losses P_S is equally valid for IM and PMSM, the rotor losses P_R are valid for the IM only. High order losses of the PMSM rotor are not considered ($P_{R,PMSM} = 0$). The corresponding equations read

$$P_S = C_{S1} \left(\frac{I_S}{I_{Sn}} \right)^2 + C_{S2} \left(\frac{\phi}{\phi_n} \right)^2 \frac{f}{f_n} + C_{S3} \left(\frac{\phi}{\phi_n} \right)^2 \left(\frac{f}{f_n} \right)^2, \tag{4.23}$$

$$P_R = \underbrace{C_{R1} \left(\frac{I_R}{I_{Sn}} \right)^2}_{P_{cu}} + \underbrace{C_{R2} \left(\frac{\phi}{\phi_n} \right)^2 \frac{f_{slip}}{f_n} + C_{R3} \left(\frac{\phi}{\phi_n} \right)^2 \left(\frac{f_{slip}}{f_n} \right)^2}_{P_{fe}}, \tag{4.24}$$

where f and f_{slip} denote the supply frequency and the slip frequency respectively [WH10]. The constants C_{S1} and C_{R1} are proportional to the phase resistances $R_{S,R}$ and the phase currents squared $I_{S,R}^2$. They can be evaluated by

$$P_{cuS} = m R_S I_S^2, \tag{4.25}$$

$$P_{cuR} = m R'_R I_R'^2. \tag{4.26}$$

The variables denoted with an apostrophe represent rotor values respectively transformed to stator level. The phase resistances $R_{S,R}$ are depending on the relative temperature increase $\Delta T = T - T_{20}$ related on a 20°C reference temperature T_{20} . Considering a linear temperature coefficient α_T , the phase resistances result in [CAR08]:

$$R_{S,R} = R_{S_{20},R_{20}}(1 + \alpha_T \Delta T) \quad (4.27)$$

The variables $R_{S_{20}}, R_{R_{20}}$ are based on a 20°C reference temperature and are proportional to the mean winding length l_w , the conductor cross section A_w and the corresponding conductor resistivity ρ [VOG88]:

$$R_{S_{20}} = \rho_{cu} \frac{\omega_{ph} l_w}{a A_w} \quad (4.28)$$

$$R_{R_{20}} = \frac{Q_R}{m} \left(R_b + \frac{1}{2 \sin^2\left(\frac{\alpha_{el}}{2}\right)} R_r \right) \quad (4.29)$$

$$R_b = \rho_{cu} \frac{l_{fe}}{A_b} \quad (4.30)$$

$$R_r = \rho_{cu} \frac{2\pi(r_{oR} - \frac{h_{slR}}{2})}{Q_R A_r} \quad (4.31)$$

Equ. (4.30) shows the bar resistance of the cage, Equ. (4.31) represents the corresponding resistance of a ring segment between two neighboring bars. Iron losses represent the second group of loss sources. They can generally be split up into hysteresis losses and eddy current losses. Therefore, sheet suppliers usually specify so-called overall toll values ν_{10}, ν_{15} , which are given for a reference flux density of either 1T or 1.5T at a frequency of 50Hz. According to [FIS06], the iron losses P_{fe} can be computed by

$$P_{fe} = m_{fe} \nu_{ref} \left(\frac{B}{B_{ref}} \right)^2 C_f C_b, \quad (4.32)$$

where the values C_f and C_b represent the iron losses depending on the supply frequency f and the degradation coefficient due to production processes respectively:

$$C_f = \left(\frac{f}{f_{ref}} \right)^{1.6} \quad (4.33)$$

$$C_b \approx 1.3 \quad (4.34)$$

Indeed, motor loss models often use the approach shown in Equ. (4.32), as the detailed determination of the loss constants C_{S2}, C_{S3} and C_{R2}, C_{R3} require at least two different loss measures at two different frequencies. Using the approach above, the iron losses P_{feS}, P_{feR} of Equ. (4.23) and Equ. (4.24) are reduced on the consideration of hysteresis losses only. The determination of the copper and

iron loss coefficients is based on the evaluation of Equ. 4.25 to Equ. 4.34.

$$P_{cuS,cuR} = C_{S1,R1} \left(\frac{I_{S,R}}{I_{Sn}} \right)^2 \quad (4.35)$$

$$P_{feS,feR} = C_{S23,R23} \left(\frac{\phi}{\phi_n} \right)^2 \left(\frac{f}{fn} \right) \quad (4.36)$$

Designing motors leads to the question on how to choose the relation between copper and iron losses. However, the maximum efficiency can be obtained by designing similar iron and copper losses [WZZC04]. The predominant part of the rotor losses arise through the torque building current component I_q . The rotor slip frequency f_{slip} at the design point tend to be low, thus, the losses are mainly dominated by the copper losses. The analytic derivation of the existing mechanical losses is generally hard to analyze, however, there exist some basic dependencies which allow a valid approximation. The mechanical losses are modeled according to [MVP08]:

$$P_m = C_m v^2 d_{oR} (l_{fe} + 2l_{axR}) \quad (4.37)$$

$$C_m = \begin{cases} 8 \dots 10 & \text{surface aeration} \\ 15 & \text{internal cooling airflow} \end{cases} \quad (4.38)$$

Equ. (4.37) reflects the basic relations. Thus, the overall mechanical losses P_m are proportional to the friction surface and the circumferential speed v squared. The variable l_{axR} depicts the axial length of the short circuit ring. The constant C_m is known to be an empirical value which has been gained by experience. Supplementary load losses mainly arise at applied loads, thus, their analysis concentrates on the computation of the current depending loss component. This component represents a general term which summarizes loss parts that cannot be assigned directly to a specific loss group. They basically arise due to high-order harmonics. Following [OVE04b], the supplementary load losses are assumed to be 0.5% of the rated input power at mains operation. As the motors are operated by converters, the modeling approach considers an additional frequency dependency, moreover, the losses are related on the rated machine power. According to [FIS06], the additional load losses P_{add} can be given by

$$P_{add} = C_{add} \left(\frac{I}{I_S} \right)^2 \left(\frac{f}{fn} \right)^2 P_n, \quad (4.39)$$

$$C_{add} = 0.0075. \quad (4.40)$$

Mechanical as well as supplementary load losses have a squared influence of the rotational speed. These losses are dominant at high speed drives which might have a considerable impact on the choice of the air gap size, (Equ. (4.103) et seq.).

4.1.6 Leakage Analysis and Evaluation

The electromagnetic energy conversion is not supported by the entire magnetic field. In fact, some flux components do not cross the air gap and therefore represent no valid linkage between stator and rotor. These flux parts are known as leakage inductance. The leakage inductance L_σ results by the sum of five subcomponents [PUR06]:

- Coil end leakage inductance L_c
- Tooth tip leakage inductance L_t
- Slot leakage inductance L_{sl}
- Harmonic leakage inductance L_δ
- Skew leakage inductance L_χ

In case of PMSMs with surface mounted magnets, two further subcomponents should be mentioned considering the

- Magnet-to-Magnet inductance L_{m2m} and the
- Magnet-to-Rotor inductance L_{m2r} .

Assuming a given MMF θ , leakage inductances lower the air gap flux density B_δ . Moreover, they used to raise the machine losses by inducing losses into ferromagnetic parts, often regarded as supplementary load losses (Sec. 4.1.5 et sqq.). The leakage inductance L_σ is inversely proportional to the torque output, thus, providing high torque densities generally requires a low leakage inductance. Contrary to that, high machine efficiencies and low torque ripples require a high leakage inductance representing a further tradeoff in machine sizing.

Coil End Leakage Inductance

Coil end leakages depend on the winding type, the shape of the coil endings and the configuration of the iron parts. Stator and rotor currents cause a 90° shifted flux distribution which induces eddy currents on the neighboring ferromagnetic parts. The analytic computation of the coil end leakage is difficult due to an enormous range of input parameters. Hence, its computation is frequently based on some basic physical relations and leakage permeance values which have been gained by experimental data. The leakage inductance is approximated by [VOG88]:

$$L_c = \frac{2}{p} \mu_0 \omega_{ph}^2 \tau_{cp} \lambda_c \quad (4.41)$$

The variables λ_c and τ_{cp} represent the coil leakage permeance value and the coil pitch respectively.

Slot and Tooth Tip Leakage Inductance

Slot leakage happens if some flux lines close through the slot without crossing the air gap. The corresponding leakage inductance is entirely defined by the slot geometry and consists of several part components. The tooth tip leakage arises when the MMF creates a magnetic potential difference on the neighboring teeth at both sides of the slot. The leakage permeance value $\lambda_{sl,t}$ is therefore depending on the relation of the slot opening width and the air gap size. According to [VOG88], the entire slot and tooth tip leakage $L_{sl,t}$ can be evaluated by:

$$L_{sl,t} = \frac{2}{p} \mu_0 \omega_{ph}^2 \tau_{cp} \frac{\lambda_{sl,t}}{q} \quad (4.42)$$

Basically, the leakage permeance value $\lambda_{sl,t}$ is higher, the higher the slot conductor and the lower the slot width. Moreover, its value increases at small slot opening widths. Consequently, slots with wide openings should be applied. As IMs uses small air gap sizes increased slot openings might enhance the harmonic content which lowers the motor efficiency.

Harmonic Leakage Inductance

Because the implemented algorithm focuses on a fundamental wave approach, the harmonic leakage inductance is entirely neglected. Nevertheless, the subsequent content gives a short overview of its basic computation. The harmonic leakage inductance considers the discrete distribution of the stator and rotor windings in slots. This discretization of the electric loading A causes the air gap field to be basically stepwise rather than sinusoidal. High order harmonics are introduced, their amount is summarized by the harmonic leakage factor σ_δ . The harmonic leakage inductance L_d results in [PUR06]

$$L_\delta = \sigma_\delta L_d, \quad (4.43)$$

$$\sigma_\delta = \sum_{\nu=-\infty, \nu \neq 1}^{\nu=+\infty} \left(\frac{\xi_\nu}{\nu \xi_1} \right)^2, \quad (4.44)$$

where ν is the ordinal number of the harmonic frequency and ξ_ν represents the corresponding winding factor. Generally speaking, the higher q , the more sinusoidal the air gap field distribution and the lower the harmonic leakage inductance.

Skew Leakage Inductance

Stator and rotor slots are often assembled in a skew position in order to reduce the influences of permeance harmonics caused by slots [PJHN08]. Skew position therefore means that the slot conductors are put at an angle being higher or lower than 90° relative to the sheet edge. The geometric offset is mostly given

in relation to the slot pitch τ_{sp} . Usually the slots of the stator stack are straight and the slots of the rotor are skewed. However, it is of course possible to skew the stator slots instead. Skewing basically weakens the electromagnetic coupling, as some flux parts created by the stator do not penetrate the rotor winding. The skew leakage inductance L_χ is given in relation to the magnetizing inductance L_d as

$$L_\chi = (1 - \chi^2)L_d, \quad (4.45)$$

$$\chi = \frac{\sin \frac{\gamma}{2}}{\frac{\gamma}{2}}, \quad (4.46)$$

where γ and χ denote the skew angle and the reduction of the induced voltage between skewed and unskewed conductor respectively. The skew angle depends on the predefined application scenario, however, the cant from one end of the stack to the other should be around one slot pitch.

Magnet-To-Magnet and Magnet-To-Rotor Inductance

Considering permanent excited rotors having surface mounted magnets, two leakage flux types can be distinguished. One type specifies the magnet-to-magnet leakage L_{m2m} , the other portion specifies the magnet-to-rotor-iron leakage L_{m2r} . Their permeances λ_{m2m} and λ_{m2r} can respectively be given by [RL04]

$$\lambda_{m2m} = \frac{\mu_0 l_{fe}}{\pi} \ln \left(1 + \frac{\pi w_\delta}{w_{tR}} \right), \quad (4.47)$$

$$\lambda_{m2r} = \frac{\mu_0 l_{fe}}{\pi} \ln \left(1 + \frac{\pi w_\delta}{h_{mR}} \right) \text{ for } w_\delta < \frac{w_{tR}}{2}, \quad (4.48)$$

where l_{fe} , w_δ and w_{tR} denote stack length, air gap size and the iron tooth width in case of an inset magnet configuration. Equ. (4.48) is a valid expression for w_δ being smaller than $\frac{w_{fe}}{2}$ which is usually true. Both permeances are higher the higher the stack length of the laminated sheets and the higher the air gap size w_δ . Moreover, the magnet-to-magnet reluctance $R_{m2m} = \frac{1}{\lambda_{m2m}}$ is higher the smaller the iron bridge between the magnets. The magnet-to-rotor-iron reluctance $R_{m2r} = \frac{1}{\lambda_{m2r}}$ increases at small magnet heights. Many models exist in literature describing how the reluctances are linked with the air gap flux density B_δ .

$$B_\delta = f(w_m, w_{fe}, R_{m2m}, R_{m2r}) \quad (4.49)$$

However, there is a somewhat easier approach for surface mounted magnet motors in [HAN94]. Equ. (4.127) gives the basic relation on how to determine the d-axis air gap flux density component B_d for the resulting MMFs along the ideal path of integration. The effective d-axis flux density crossing the air gap can be

given by considering an additional correction factor σ_c .

$$B_d = \sigma_c B_r \left(1 - \frac{H_m}{H_c} \right) \quad (4.50)$$

$$\sigma_c = \frac{C_l C_f}{1 + C_r \frac{\mu_{rec}}{C_p}} \begin{cases} 0.9 \leq C_l < 1.0 \\ 1.0 \leq C_r < 1.2 \\ C_f = \frac{A_m}{A_\delta} \\ C_p = \frac{w_m}{w_\delta} \end{cases} \quad (4.51)$$

The constants C_f , C_p , C_l and C_r denote flux focusing, permeance, leakage and reluctance factor respectively. The first two constants depend on design values, therefore C_f and C_p determine the cross section relation and the length relation between the magnets and the air gap respectively. In practice, the constants C_l and C_r are hardly computed analytically as their evaluation is too difficult. Their values are chosen from empirical data which are usually within the ranges given in Equ (4.51). The variable μ_{rec} considers the characteristic recoil permeability of the magnet material.

4.1.7 Overload Capability

The subsequent sections analyze the basic relations concerning IM and PMSM overload capabilities and give background information on their computation.

Induction Motors

The pull-out torque capability of IMs can be derived by a common simplified circuit, shown in Fig. 4.3.

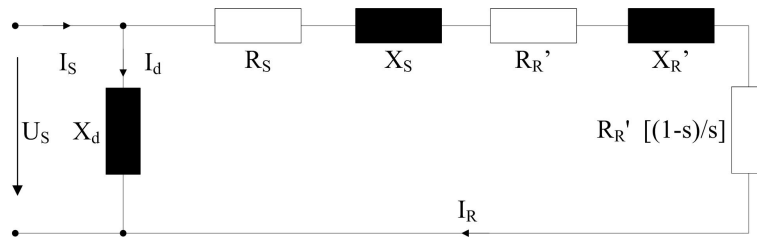


Figure 4.3: Simplified circuit model for overload considerations [PUR06].

The air gap voltage is supposed to be the terminal voltage neglecting any voltage drop at the stator. The mechanical power output P_{mech} can basically be given by the air gap power P_δ minus the corresponding slip power P_R in the rotor:

$$P_{mech} = P_\delta - P_R = P_\delta - P_\delta s \quad (4.52)$$

Considering the valid expressions of the rotor losses as a function of the per unit slip s , the torque output T_{mech} and the corresponding rotor current I_R can respectively be represented by

$$T_{mech} = \frac{P_{mech}}{\omega_{mech}} = \frac{mpR'_R I_R^2}{\omega_n s}, \quad (4.53)$$

$$I_R = \frac{U_S}{\sqrt{(R_S + \frac{R'_R}{s})^2 + (X_S + X'_R)^2}}. \quad (4.54)$$

Equ. (4.52) shows the slip dependency of the rotor losses P_R . Assuming a per unit slip of $s = 1$, the entire air gap power is converted into rotor losses, representing a short-circuited transformer. Thus, the pull-out slip s_{po} can be given by the equalization of air gap power P_δ and rotor losses P_R . The relative angular slip frequency ω_{po} results by the multiplication of the pull-out slip s_{po} and the angular frequency ω_n given by

$$m \frac{R'_R}{s_{po}} I_R^2 = m \sqrt{R_S^2 + (X_S + X'_R)^2} I_R^2, \quad (4.55)$$

$$s_{po} = \frac{R'_R}{\sqrt{R_S^2 + (X_S + X'_R)^2}} = \frac{\omega_{po}}{\omega_n}. \quad (4.56)$$

The pull-out torque T_{po} can generally be given by the fraction of the air gap power P_δ and the angular slip frequency ω_{po} . Substituting Equ. (4.54) into Equ. (4.26), the torque relation can be specified as

$$T_{po} = \frac{m}{\omega_{po}} \frac{U_S^2}{(R_S + R'_R)^2 + (X_S + X'_R)^2} R'_R. \quad (4.57)$$

The pull-out torque T_{po} is directly proportional to the stator voltage U_S squared and inversely proportional to the phase impedance. Hence, considering constant power range ($n > n_n$) having a limited stator voltage U_S , the pull-out torque decreases inversely proportional to the angular frequency ω_n squared. As the phase resistances of stator and rotor are far lower than the phase leakages, they might be neglected for the torque computation without tainting the result. However, increasing the overload capability of IMs basically requires a low leakage design which can be realized by one of the equations mentioned in Sec. 4.1.6.

Permanent Magnet Synchronous Motors

PMSMs mounted magnets basically provide two kinds of torques. The predominant part of the torque output is given by the synchronous torque T_s which depends on the magnetic excitation and therefore on the magnet characteristics. The second torque part T_r is independent of the magnetic excitation and is due to the different permeances in d- and q-direction. The maximum operative pull-out torque T_{po} can be derived by the model presented in Fig. 4.4.

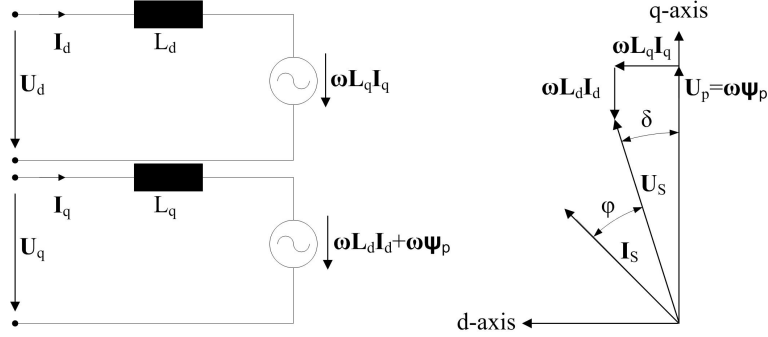


Figure 4.4: Simplified circuit models for the d- and q-axis. Stator resistances and stray reactances are not considered.

For simplification, the stator resistance and the stator reactance are neglected for the subsequent explanations. The basic equation of the torque output T is commonly known and is given by [RIE06]

$$T = \frac{3}{2}p(\psi_d i_q - \psi_q i_d). \quad (4.58)$$

The presentation of the torque output related on the synchronous generated voltage U_p , the terminal voltage U_S and the angular displacement δ requires the consideration of decoupled equations in d- and q-direction respectively. These quantities read:

$$\psi_S = \sqrt{\psi_d^2 + \psi_q^2} \quad (4.59)$$

$$u_S = \sqrt{U_{Sd}^2 + U_{Sq}^2} \quad (4.60)$$

$$\psi_d = L_d i_d + \frac{u_p}{\omega_n} \quad (4.61)$$

$$\psi_q = L_q i_q \quad (4.62)$$

Considering steady state conditions, the voltage equations can be depicted very simply representing the coupled voltage components only. Their corresponding current components can be evaluated analytically by the vector diagram shown in Fig. 4.4.

$$u_{Sd} \Big|_{\frac{d}{dt}=0} = -\omega_n \psi_q = u_S \sin(\delta) \quad (4.63)$$

$$i_{Sd} \Big|_{\frac{d}{dt}=0} = \frac{u_p - u_S \cos(\delta)}{\omega_n L_d} \quad (4.64)$$

$$u_{Sq} \Big|_{\frac{d}{dt}=0} = \omega_n \psi_d + \omega_n \psi_p = u_S \cos(\delta) \quad (4.65)$$

$$i_{Sq} \Big|_{\frac{d}{dt}=0} = \frac{u_S \sin(\delta)}{\omega_n L_q} \quad (4.66)$$

Substituting Equ. (4.59) and Equ. (4.66) into Equ. (4.58) the torque relations can be given by [RIE06]:

$$T = \frac{3}{2} \frac{p}{\omega_n} (i_{Sd} u_{Sd} + i_{Sq} u_{Sq}) \quad (4.67)$$

$$= \frac{3}{2} \frac{p}{\omega_n} \left[\frac{u_p - u_S \cos(\delta)}{\omega_n L_d} u_S \sin(\delta) + \frac{u_S \sin(\delta)}{\omega_n L_q} u_S \cos(\delta) \right] \quad (4.68)$$

$$= \frac{3}{2} \frac{p}{\omega_n} \left[\frac{u_p u_S}{\omega_n L_d} \sin(\delta) + \frac{u_S^2}{2} \left(\frac{1}{\omega_n L_q} - \frac{1}{\omega_n L_d} \right) \sin(2\delta) \right] \quad (4.69)$$

Using RMS values, the pull-out torque capability results in:

$$T_s = 3p \frac{U_p U_S}{\omega_n^2 L_d} \sin(\delta) = T_{s,po} \sin(\delta) \quad (4.70)$$

$$T_r = \frac{3}{2} \frac{p}{\omega_n^2} U_S^2 \left(\frac{1}{L_q} - \frac{1}{L_d} \right) \sin(2\delta) = T_{r,po} \sin(2\delta) \quad (4.71)$$

As stated in Sec. 3.6.1, the pull-out torque capability is mainly influenced by the d-axis inductance L_d , the stator supply voltage U_S and the inductance difference $L_q - L_d$. According to Equ. (4.70), the synchronous torque T_s decreases inversely proportional to the angular frequency ω_n at constant power region ($n > n_n$). The reluctance torque part T_r is affected by the doubled angular displacement δ . Indeed, this causes the total torque output to be highest at a tilt angle δ being lower than $\frac{\pi}{2}$. The tilt angle results from a superposition of the synchronous and reluctance torque part for $\delta = [-\pi \dots \pi]$ evaluating the angle at the maximum torque output. The corresponding polar wheel angle at the design point is determined according to Equ. (4.66).

4.2 Design Methodology

The DM aims at a valid and time-efficient design approach for IMs and PMSMs trying to minimize the computation time for a conceptual evaluation of the motors concerning dimensions and operational characteristics. The presented equations are valid for IM and PMSM sizing issues and allow a computation of dimensions, masses and operational characteristics of the machines. The given DM is valid for each kind of cooling conditions. However, the DM will be exemplified by an air-cooled IM and an air-cooled PMSM having equal outer stator and inner rotor diameters. In order to demonstrate the correctness of the DM, the resulting design and operational characteristics of the machines have been compared with those of the electric motor manufacturer THIEN eDrives GmbH [THI11].

4.2.1 Assumptions

The analysis and computation of the designed IM and PMSM will be done under the following simplifications:

- The DM focuses on a fundamental wave approach only.
- The algorithm considers parallel teeth only.
- There exists a constant current density within the slots. Skin effects in the wires are not considered.
- The motor parameters are supposed to be phase values transformed to stator level.

4.2.2 Sizing Examples

The following sections focus on the sizing of a three-phase radial field orientated inner-rotor IM and PMSM. The motors are supposed to be used within a wheel rim at the rear axle of a vehicle. Due to package and mechanical stability considerations, the maximum outer stator diameter d_{oS} was defined by 170mm. The design concentrates on a high electromagnetic utilization of the machines providing a thermally stable continuous operation for a nominal power P_n of 5.25kW at a base speed n_n of 3000rpm. Both machines are operated up to 12000rpm. The design specifications of IM and PMSM are shown in Tab.4.2. Their values have been derived from the system specifications of the underlying automotive traction application given in Sec. 6.3.

Pole Pair Number

The physical dimensions and the number of pole pairs p specify the air gap flux density B_δ and the rated machine flux ϕ_n . Assuming the same saturation levels, high pole machines have lower yoke heights, as the lower machine flux ϕ_n can be carried over a thinner yoke (cf. Sec. 3.5.1). However, iron losses and cooling requirements increase, as the angular frequency ω_n is p times higher than the mechanical angular frequency ω_m . Hence, there is a tradeoff between small motor dimensions and high motor efficiencies. Focusing on IMs, higher pole pair numbers might be sensitive to the power factor which decreases significantly. According to that, the choice of the pole pair number at IMs is advantageously limited to $p = 4$ [CWBR04].

Both machines are designed as four-pole machines which represents a good compromise between the resulting dimensions and the reachable motor efficiencies.

Flux Density, Stack Length and Shear Force Density

The peak value of the air gap flux density \hat{B}_δ for the IM is specified at 0.9T which represents a common specification for IM designs (0.88 – 0.92T). Considering PMSMs, the magnet wheel induction \hat{B}_p is lower resulting in 0.8T. The local tooth flux densities $\hat{B}_{tS,tR}$ represent one of the main sizing parameters. In case of air cooling, they should be chosen to be within 1.77–1.8T for stator and rotor. For this reason, the relative tooth width parameter $\frac{w_t}{w_{sl}}$ is introduced providing information on how to portion tooth width w_t and slot width w_{sl} within the slot pitch τ_{sp} . The corresponding equation for the stator reads:

$$\tau_{sp} = \frac{(d_{iS} + h_{tS})\pi}{Q_S} \quad (4.72)$$

The peak value of the yoke flux densities should be chosen to be around 1.55 – 1.60T for the stator and 1.45 – 1.65T for the rotor for an air-cooled machine. According to Sec. 4.1.3, there are some guidance values on how to choose shear force densities for a thermally acceptable operation. Considering conceptual machine design studies, the shear force density σ_n is mostly selected by experimental data depending on an achievable air gap diameter d_δ for a certain number of pole pairs p . Therefore, having a maximum stator diameter of 170mm, the air gap diameter d_δ should be chosen to be within 100mm to 110mm for an air-cooled four-pole machine [HUB11].

Stator diameter d_{oS} [mm]	Air gap diameter d_δ [mm]	
	$p = 2$	$p = 3$
170	100 – 110	110 – 120
200	120 – 130	130 – 140
240	150 – 160	160 – 170
270	170 – 180	180 – 190
300	190 – 200	200 – 210

Table 4.1: Suggested air gap diameter range d_δ depending on stator diameter d_{oS} and the number of pole pairs p [HUB11].

Tab. 4.1 gives a design suggestion on how to choose the air gap diameter d_δ depending on the number of pole pairs p and a maximum outer stator diameter d_{oS} of air-cooled machines. Hence, the start value of the shear force density σ_n was selected to be $13 \frac{\text{kN}}{\text{m}^2}$ for the IM and $17 \frac{\text{kN}}{\text{m}^2}$ for the PMSM. The corresponding start value of the air gap diameter was selected to be 103mm. Considering the given values, the stack length can be approximated by

$$l_{fe} = \frac{2T_n}{\sigma_n \pi d_\delta^2}, \quad (4.73)$$

with T_n denoting the design torque. The individual stack lengths of the four-pole machines eventually resulted in 80mm for the IM and 65mm for the PMSM.

Number of Stator Slots per Pole and Phase

The design variable q characterizes the number of stator and rotor slots per pole and phase. Considering the given outer stator diameter d_{oS} the upper range of q is physically limited by the smallest mechanically possible slot pitch τ_{sp} . Choosing higher values for q generally attenuates high order air gap flux densities and is advantageous concerning motor noise and motor efficiency. Because of that, q should be chosen to be a whole-number value and should be selected higher than two if possible [BIK99].

According to this, the variable q_S of the stator was selected to three for both motor types. The individual adjustment of q_R of the rotor depending on q_S for the IM is given in Sec. 4.2.3.

Slot and Iron Fill Factor

The slot fill factor k_{sl} is a matter of the implemented winding design. Moreover, it is affected by the present supply voltage considering a given internal power. Low voltage applications tend to have slightly higher slot fill factors compared to high voltage applications [VOG88]. They do have bigger wire diameters which might lead to a higher utilization of the slot space. The slot fill factor k_{sl} reads:

$$k_{sl} = \frac{J_{sl}}{J_{cu}} \begin{cases} \text{low voltage,} & 0.3 \leq k_{sl} \leq 0.5 \\ \text{high voltage,} & 0.2 \leq k_{sl} \leq 0.4 \end{cases} \quad (4.74)$$

The slot fill factors k_{sl} of around 42% given in Tab. 4.2 represent reference values which are assumed to be achievable for the present application at a voltage level of 250V. The iron fill factor k_{fe} denotes a correction factor of the active magnetic cross section. It depends on the insulating medium and varies within the range of 0.95 – 0.97 [NER06].

Current Density

According to [HUB11] and [VOG88], the stator copper current density J_{cu} for self-cooled machines is around $3 - 8 \frac{\text{A}}{\text{mm}^2}$ for both motor types. In case of a copper winding, the current density of the IM rotor can basically be within the same range if thermally stable. Aluminium cages allow a slightly lower range ($3 - 6.5 \frac{\text{A}}{\text{mm}^2}$), as the volume conductivity of aluminium $\frac{1}{\rho_{al}}$ is lower compared with copper [FB07]:

$$\frac{1}{\rho_{cu}} = 58 \frac{\text{Smm}^2}{\text{m}} \quad (4.75)$$

$$\frac{1}{\rho_{al}} = 37 \frac{\text{Smm}^2}{\text{m}} \quad (4.76)$$

The copper current density for the stator was iterated to comply with the maximum stator diameter of $d_{oS} = 170\text{mm}$ on the one hand and to get a thermally stable winding temperature of not higher than 125°C on the other hand. The IM rotor uses an aluminium cage. Its current density was iterated to get a thermally stable cage temperature of not higher than 165°C . Therefore, the shown current densities in Tab. 4.2 are based on a thermal model introduced in Sec. 5.3.

Slot Opening Width and Slot Opening Height

The design of slot openings influences the stator and rotor leakage. Thus, according to Sec. 3.5.1 and Sec. 3.6.1, the design of slot opening width w_r and slot opening height h_r is sensitive on the pull-out torque capabilities of the machines.

The corresponding dimensions of the slot openings have been obtained by the considerations given in Sec. 4.1.6 having a special focus on a low slot and tooth tip leakage induction $L_{sl,t}$. The slot opening widths and heights in Tab. 4.2 are given relative to the tooth width. They have been designed in order to meet the requirements for the insertion of slot conductors and the pull-out torque which should be upon 34Nm for a minimum battery voltage of 250V .

Parallel Branches and Number of Conductors per Slot

Besides the given sizing factors, the design process has to consider the electric motor supply system. The most important two parameters to be adjusted are the number of parallel branches a and the number of conductors per slot ω_{sl} . Especially low voltage applications require a careful choice of ω_{sl} if a high number of stator slots should be realized with a small number of serial connected windings. The intermediate circuit voltage is directly coupled with the battery voltage representing a load-dependent voltage level. The design process therefore needs to consider the minimal available battery voltage of 250V .

The motors are designed with a two layer distributed winding having 20 conductors per slot and a coil pitch of $1 : 8$. The coil pitch τ_{cp} has been selected according to the statements given in Sec. 4.1.6 trying to get a low L_c and $L_{sl,t}$. Focusing on machine efficiencies, the most undesirable harmonics are the third harmonic and multiple of it as they used to increase machine losses and do not contribute anything to the electromagnetic torque output. Both motor types are therefore star connected to eliminate the third harmonic.

Sheet Material

Fig. 4.5 shows the magnetic excitation characteristics and the corresponding iron losses of two different electric sheets frequently used in electric machines. Both sheets meet the requirements given in the European standard DIN EN10106.

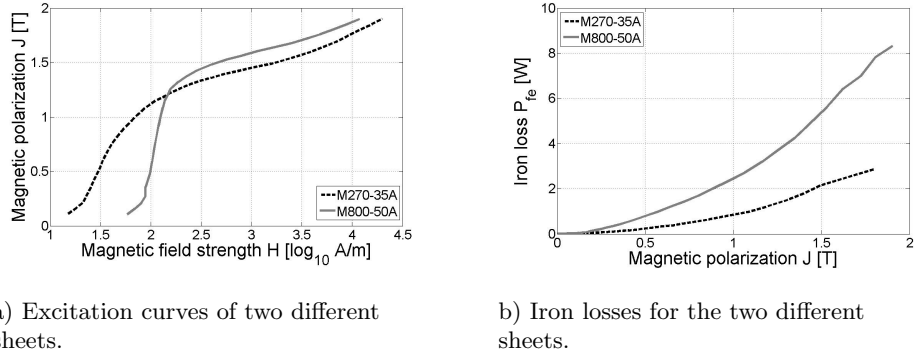


Figure 4.5: Characteristics of two different electric sheets [THY11].

The notation of the illustrated sheets provides information on their material qualities and sizes. Thus, “M270-35A” specifies an electric sheet having 0.35mm thickness and a maximum loss of 2.7W at 1.5T and 50Hz. The same statement is valid for the second sheet “M800-50A”. This sheet provides lower magnetic field strengths at higher saturation levels of the machine which is quite beneficial concerning small motor sizes. However, its loss characteristic is worse compared to the first one. Thicker sheets naturally have higher losses as the eddy currents face a wider cross section. In fact, it is a matter of cost meaning lower material quality for lower prizes and vice versa. The given sheets reflect the basic tradeoff at machine sizing - either small motor sizes at higher losses or large sizes at lower losses.

The design of IM and PMSM uses the “M800-50A” sheet as the compliance with the maximum stator diameter of 170mm is of prime interest. The material design parameters represent generally accepted values found in the literature [MAG11], [VOG88], [BOE07]. The design parameters are given in Tab. 4.2.

General Design Parameters	IM		PMSM	
Design torque T_n [Nm]	17.2		17.4	
Air gap flux density, B_δ [T]	0.9		0.8	
Shear force density σ_n [$\frac{N}{m^2}$]	13410		16940	
Number of pole pairs p [-]	2		2	
Supply frequency f_n [Hz]	100		97	
Phase number m [-]	3		3	
Air gap size - one sided w_d [mm]	0.4		1	
Stack length l_{fe} [mm]	80		65	
Iron fill factor k_{fe} [%]	97		97	
Slot/Yoke Design Parameters	Stator	Rotor	Stator	Rotor
Slot conductor density J_{cu} [$\frac{A}{mm^2}$]	7	3.6	8	-
Slot number Q [-]	36	28	36	-
Slot fill factor k_{sl} [%]	42	100	42	-
Slots per pole and phase q [-]	3	$2\frac{1}{3}$	3	-
Tooth width relation [%] basis: slot pitch (IM) $\frac{w_t}{w_{sl}}$ basis: pole pitch (PMSM) $\frac{w_m}{\tau_{pp}}$	43.9	55.4	41.9	95
Slot opening width relation $\frac{w_r}{w_t}$ [%]	48	20	50	-
Slot opening height relation $\frac{h_r}{w_t}$ [%]	48	40	48	-
Skewing relation $s_{\chi S,R}$ [-]	0	1.5	1.5	0
Yoke flux density, $\frac{B_y}{B_t}$ [%]	85	92	70.5	80
Winding Design Parameters	IM		PMSM	
Parallel branches a [-]	2		2	
Conductors per slot ω_{sl} [-]	20		20	
Coil pitch τ_{cp} [-] 1:	8		8	
Material Design Parameters				
Conductor/Magnet density [$\frac{kg}{m^3}$]	8920	2700	8920	7500
Conductor conductivity [$\frac{Smm}{m}$]	57	32	57	0.6
Sheet density M800-50A [$\frac{kg}{m^3}$]	7800	7800	7800	7800
Remanence flux density N38SH [T]	-	-	-	1.22
Coercive field strength [$\frac{kA}{m}$]	-	-	-	840

Table 4.2: Design specification of IM and PMSM.

4.2.3 Induction Motor Design

The following content derives the basic equations for IM sizing exemplified at one single pole pitch τ_{pp} . The sections focus on the computation of the magnetic circuit and present the design stages of the DM. For evaluation reasons, the IM specified in Tab. 4.2 has additionally been computed by the electric motor manufacturer THIEN eDrives GmbH.

Assumptions

According to the considerations given in Sec. 4.2.2, the air-cooled IM is designed to have $2p = 4$ poles and uses a three-phase distributed winding with an aluminium squirrel cage. The number of rotor slots per pole and phase q_R should be close to that of the stator q_S [VOG88]. However, q_S and q_R must not be equal to each other,

$$q_R = q_S \pm \frac{2}{3}. \quad (4.77)$$

This choice is very important to obtain a low cogging torque and a low harmonic content. Experimental data showed that the slot combinations given in Equ. (4.77) are preferable [HUB11]. Therefore, the stator has 36 slots, the rotor uses 28 slots representing a number of slots per pole and phase of $q_S = 3$ and $q_R = 2\frac{1}{3}$. The rotor slots are skewed by $1.5 \tau_{sp}$.

Magnetic Circuit

The presented equations are based on an ideal sinusoidal characteristic of the air gap flux density B_δ , see Fig. 4.6. The computation of the magnetic circuit utilizes the symmetry of the design. This concept of modeling is very convenient, time-saving and eases the computations by considering one single pole only. Fig. 4.7 depicts the main path of integration at one single pole (dotted line) and presents

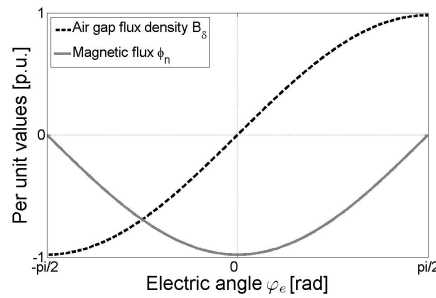


Figure 4.6: Per-unit illustration of air gap flux density B_δ and the magnetic flux ϕ_n over a pole angle of $\varphi_e = 180^\circ$.

the dimensioning variables of the machine's cross-sectional area. The stator and rotor segments are given for the mechanical angle $\varphi_m = \frac{\pi}{p}$ resulting in 90° for $p = 2$. In order to grant consistency to Fig. 4.6, the electric angle φ_e is given by its equivalent $\varphi_e = p\varphi_m$. The abbreviations used in Fig. 4.7 consist of three letters, which either specify width w , height h or a radius r of the corresponding region (slot, tooth, yoke) and component (stator, rotor). The air gap radius denotes the torque building radius and is figuratively given by r_δ . The relations read:

$$\phi_n = l_{fe}k_{fe}r_\delta \int_0^{\frac{\pi}{p}} B_\delta d\varphi_m = \frac{r_\delta l_{fe}k_{fe}}{p} \hat{B}_\delta [-\cos(p\varphi_m)]_0^{\frac{\pi}{p}} = \frac{2}{p} r_\delta \hat{B}_\delta l_{fe}k_{fe} \quad (4.78)$$

$$\hat{\phi}_y = \frac{1}{2} \phi_n = \frac{1}{p} \hat{B}_\delta r_\delta l_{fe}k_{fe} \quad (4.79)$$

$$\hat{B}_y = \frac{\hat{\phi}_y}{h_y l_{fe}k_{fe}} = \frac{r_\delta}{p h_y} \hat{B}_\delta \quad (4.80)$$

$$\hat{\phi}_t = \frac{\phi_n}{w_t S l_{fe}k_{fe}} - \mu_0 H_t \frac{w_s}{w_t} \quad (4.81)$$

$$\hat{B}_t = \hat{B}_\delta \frac{w_{sl} + w_t}{w_t} \quad (4.82)$$

Equ. (4.78) clearly shows, that the nominal machine flux ϕ_n is already defined by the air gap flux density B_δ and the corresponding geometry of the motor. The same statement can be given for the yoke flux $\hat{\phi}_y$, the tooth flux $\hat{\phi}_t$ and the corresponding densities \hat{B}_y and \hat{B}_t respectively. Tooth flux densities below 1.7T cause neighboring slot spaces to be more or less field-free [VOG88]. However, flux densities higher than 1.7T cause additional magnetic fields in the slot space influencing the tooth fluxes along the main path of integration. Equ. (4.82) depicts the tooth flux density \hat{B}_t , assuming the cumulated machine flux of a slot pitch to pass one tooth. The following considerations do not consider magnetic load shedding of teeth corresponding to a relative permeance of air μ_0 being zero.

Stator as well as rotor yokes have to carry half of the rated flux ϕ_n along one pole pitch τ_{pp} . The rated flux splits up into several part fluxes mainly crossing the excited teeth at both ends of the pole pitch. The yoke fluxes are assumed to have sinusoidal characteristics causing flux densities and magnetic field strengths to be not constant. Rotor yokes might be saturated higher if the shaft restricts the cross section for the flux. The corresponding rotor flux densities can be lowered by magnetic load shedding through proper shaft materials.

Equ. (4.83) to (4.88) show the computation of the MMFs and the corresponding magnetizing slot current density $J_{d,sl}$. The main path of the MMF is split up into five fields of integration. The equation read:

$$\theta = \oint H dl = \int H_{yS} dl + \int H_{yR} dl + 2 \left(\int H_{tS} dl + \int H_{tR} dl + \int H_\delta dl \right) \quad (4.83)$$

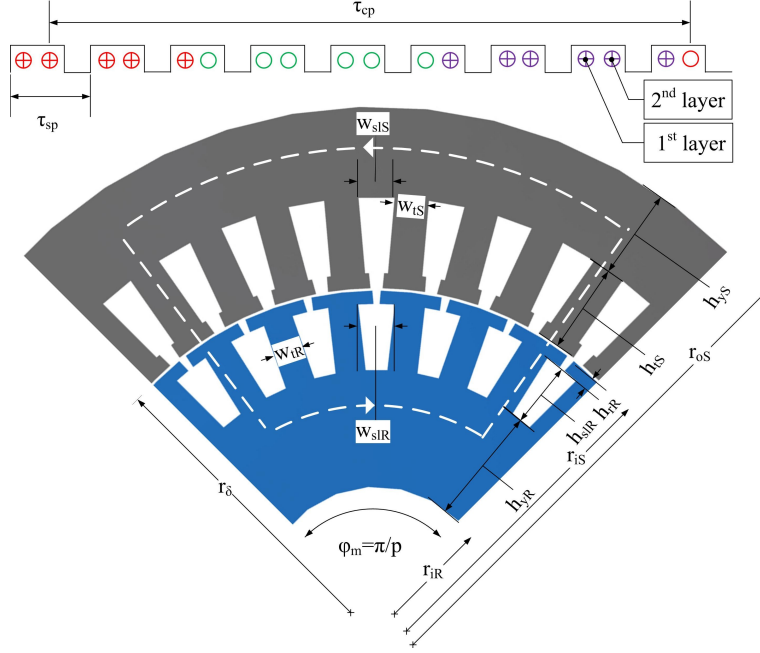


Figure 4.7: Stator and rotor segment with parallel sided teeth over a symmetric pole pitch τ_{pp} . The main path of integration is depicted by the white dotted line.

with the components

$$\begin{aligned} \int H_{yS} dl &= \int_{-\frac{\pi}{2}}^{\frac{\pi}{2}} \frac{\hat{B}_{yS}}{\mu_{fe}} \left(\frac{r_{oS} + r_{iS} + h_{tS}}{2} \right) d\varphi = \int_{-\frac{\pi}{2}}^{\frac{\pi}{2}} \frac{\hat{B}_{yS}}{\mu_{fe}} \left(r_{oS} - \frac{h_{yS}}{2} \right) d\varphi = \\ &= \left(r_{oS} - \frac{h_{yS}}{2} \right) \sum \frac{\hat{B}_{yS}}{\mu_{fe}} \Delta\varphi, \\ &= \left(r_{oS} - \frac{h_{yS}}{2} \right) \sum_{k=-\frac{N}{2}}^{\frac{N}{2}} \frac{\hat{B}_{yS}}{\mu_{fe}} \cos \left(\frac{k \pi}{N p} \right), \end{aligned} \quad (4.84)$$

$$\int H_{yR} dl = \left(r_{iR} + \frac{h_{yR}}{2} \right) \sum_{k=-\frac{N}{2}}^{\frac{N}{2}} \frac{\hat{B}_{yR}}{\mu_{fe}} \cos \left(\frac{k \pi}{N p} \right), \quad (4.85)$$

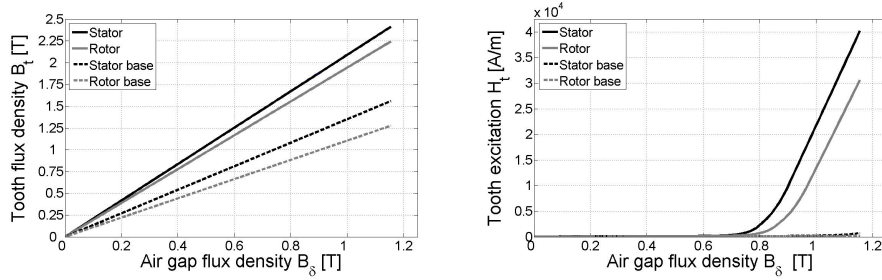
$$\int H_{tS,R} dl = \frac{\hat{B}_{tS,R}}{\mu_{fe}} h_{tS,R} = \frac{\hat{B}_{\delta}}{\mu_{fe}} \frac{w_{sI,S,R} + w_{tS,R}}{w_{tS,R}} h_{tS,R}, \quad (4.86)$$

$$\int H_{\delta} dl = \frac{\hat{B}_{\delta}}{\mu_0} w_{\delta}. \quad (4.87)$$

Hence, it can be written:

$$\begin{aligned}\theta &= \oint H dl = \int J_{d,sl} dA_{slS} = \hat{J}_{d,sl} \frac{A_{slS}}{w_{slS} + w_{tS}} \left(r_{iS} + \frac{h_{tS}}{2} \right) \int_{-\frac{\pi}{2p}}^{\frac{\pi}{2p}} \cos(p\varphi_m) d\varphi_m \\ &= \frac{2}{p} \hat{J}_{d,sl} \frac{A_{slS}}{w_{slS} + w_{tS}} \left(r_{iS} + \frac{h_{tS}}{2} \right) = \frac{2}{p} \hat{A}_d \left(r_{iS} + \frac{h_{tS}}{2} \right)\end{aligned}\quad (4.88)$$

Practically, the boundaries of the integrals are not clearly defined as they mutually influence each other. According to Fig. 4.6, the air gap flux density B_δ is maximum at both sides of the pole pitch. However, the MMFs along the teeth tend to be high causing a flattening and enlarging of the sinusoidal field characteristic. Therefore, the higher the saturation levels of the teeth, the higher the reduction of the air gap field in the center of the pole and the higher the increase of the field outside the pole center. It might have ideal sinusoidal characteristic in case of unsaturated motors. Indeed, there is an influence of the MMF along the yoke on the air gap field being higher the lower the number of pole pairs p [VOG88]. The subsequent analysis considers the individual MMFs on their own, mutual influence of the part fluxes is neglected.



a) Tooth flux densities $B_{tR,tS}$ versus different air gap flux densities B_δ .

b) Magnetic excitation $H_{tR,tS}$ for different air gap flux densities B_δ .

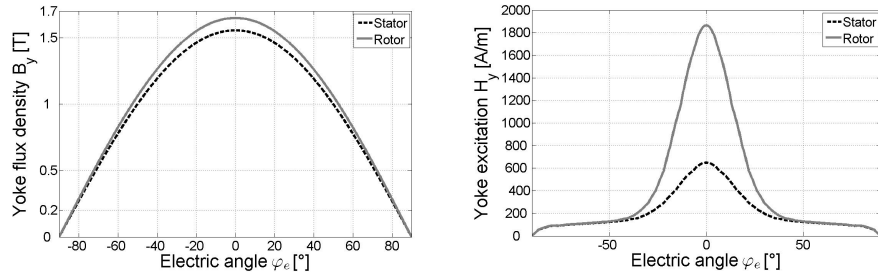
Figure 4.8: Different tooth flux densities and their corresponding magnetic excitation.

Fig. 4.8 and 4.9 show the resulting local flux densities B and their corresponding magnetic excitation H using a “M800-50A” sheet. Due to the consideration of slot openings, the tooth flux ϕ_t faces two different cross sections resulting in two different tooth flux densities B_t . The first cross section at the entrance (base) is bigger having a radial length w_{tS^1,tR^1} . The second cross section is specified in the middle of the tooth height h_t and can be given by w_{tS^2,tR^2} :

$$w_{tS^1} = \frac{2(r_{iS} + h_{rS})\pi}{Q_S} - w_{rS} \quad w_{tS^2} = \frac{2(r_{iS} + \frac{h_{tS}}{2})\pi}{Q_S} - w_{slS} \quad (4.89)$$

$$w_{tR^1} = \frac{2(r_{oR} - h_{rR})\pi}{Q_R} - w_{rR} \quad w_{tR^2} = \frac{2(r_{oR} - \frac{h_{tR}}{2})\pi}{Q_R} - w_{slR} \quad (4.90)$$

According to Fig. 4.8b, the magnetic excitation H of the sheet material is highly non-linear and increases significantly at air gap flux densities B_δ being higher than 0.9T (cf. Sec. 4.2.2).

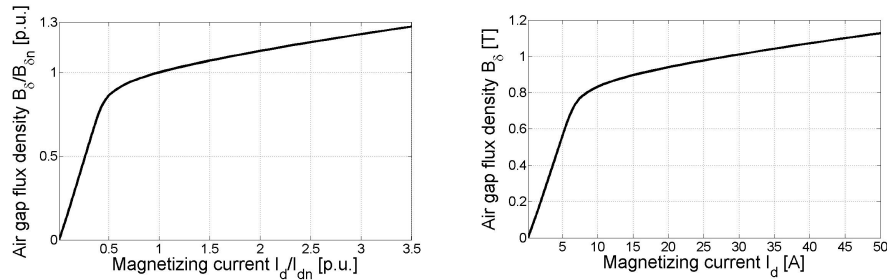


a) Yoke flux densities $B_{yR,yS}$ along a symmetric pole pitch.

b) Magnetic excitation $H_{yR,yS}$ of the yoke flux densities B_y .

Figure 4.9: Sinusoidal yoke flux densities and their corresponding magnetic excitations over a symmetric pole pitch.

According to the statements given in Sec. 4.2.2, the IM is designed to provide a fundamental air gap flux density \hat{B}_δ of 0.9T. The tooth widths were adjusted to get a flux density \hat{B}_t of 1.8T representing a high magnetic utilization of the IM. The maximum yoke flux densities of the stator \hat{B}_{yS} and the rotor \hat{B}_{yR} are 85% and 92% lower compared to their tooth flux densities resulting in $\hat{B}_{yS} = 1.53\text{T}$ and $\hat{B}_{yR} = 1.66\text{T}$. Although \hat{B}_{yS} and \hat{B}_{yR} are relatively close, their magnetic excitations differ considerably. The higher saturated rotor yoke causes a significant increase of the magnetizing excitation H_{yR} being approximately $1.2 \frac{\text{kA}}{\text{m}}$ higher compared to H_{yS} , see Fig. 4.9b.



a) Per-unit illustration of the magnetizing curve.

b) Air gap flux density \hat{B}_δ versus magnetizing current I_d .

Figure 4.10: Air gap flux density characteristic at different magnetizing currents.

Fig. 4.10 illustrates the air gap flux densities B_δ depending on the magnetizing current I_d for the “M800-50A” sheet. The MMF has therefore been transformed

to the corresponding magnetizing phase current I_d . According to Equ. (4.88), the magnetizing slot current $I_{d,sl}$ can be given by Equ. (4.91).

$$I_{d,sl} = \frac{\hat{\theta}}{2} \frac{p}{\sqrt{2}} \frac{1}{\xi_w} \frac{w_{slS} + w_{tS}}{r_{iS} + \frac{h_{slS}}{2}} \quad (4.91)$$

$$I_d = I_{d,sl} \frac{a}{\omega_{sl}} \quad (4.92)$$

$$Q_S = \frac{2\pi(r_{iS} + \frac{h_{tS}}{2})}{(w_{slS} + w_{tS})} \quad (4.93)$$

$$\omega_{ph} = \frac{Q_S \omega_{sl}}{2am} = \frac{Q_S \omega_w}{am} \quad (4.94)$$

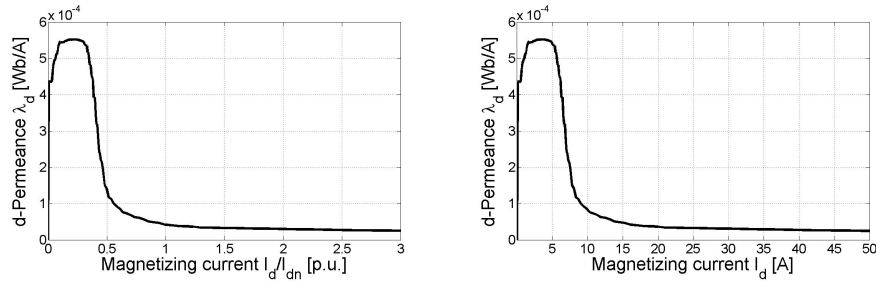
The variables ω_{sl} and Q_S denote the number of conductors per slot and the stator slot number respectively. Considering Equ. (4.91) to (4.94) the magnetizing phase current reads

$$I_d = \frac{1}{2} \frac{\pi}{\sqrt{2}} \frac{\hat{\theta}}{m \omega_{ph} \xi_w} p. \quad (4.95)$$

The corresponding characteristic of the induced phase voltage U_d is more or less equivalent to the characteristic of the air gap flux density B_δ shown in Fig. 4.10. It is proportional to the fundamental wave of the machine flux ϕ_n , the angular frequency ω_n and the number of turns per phase ω_{ph} [VOG88]. The equation reads:

$$U_d = \frac{\omega_n}{\sqrt{2}} \omega_{ph} \xi_w \hat{\phi}_n \quad (4.96)$$

Equ. (4.96) might be used as the primary equation for the determination of ω_{ph} . However, it illustrates the basic relation between machine size, winding topology and induced phase voltages.



a) Per-unit illustration of magnetizing permeance λ_d .

b) Magnetizing permeance λ_d versus magnetizing current I_d .

Figure 4.11: Magnetizing permeance of different magnetizing currents.

Fig. 4.11 shows the magnetic permeance λ_d of the IM depending on different magnetizing currents I_d . Fig. 4.11a illustrates the high magnetic utilization of

the machine as the characteristic of the permeance is already very flat around a 1p.u. magnetizing current. The computation of the phase winding inductance L_d depends on the flux linkage ψ_d and the magnetizing current $i_d = \frac{m}{2} I_d$, shown in Equ. (4.97). Assuming a constant air gap size w_δ , the main inductance of a phase winding results by the evaluation of Equ. (4.78), Equ. (4.95) and Equ. (4.96).

$$X_d = \frac{U_d}{i_d} = \frac{\omega \psi_d}{i_d} = \omega L_d \quad (4.97)$$

$$L_d = (\omega_{ph} \xi_1)^2 r_\delta l_{fe} k_{fe} \frac{1}{p^2} \frac{4}{\pi} \frac{\hat{B}_\delta}{\hat{\theta}} \quad (4.98)$$

$$\hat{\theta} = \frac{2}{\pi} \alpha_{fl} \frac{\hat{B}_\delta}{\mu_0} w_\delta \quad (4.99)$$

Equ. (4.98) shows the basic dependencies of the magnetizing inductance L_d on the choice of design parameters. Thus, the main inductance L_d is inversely proportional to the number of pole pairs squared. According to Equ. (3.6), Equ. (4.98) eventually shows the design limits of IMs, as the main inductance L_d is proportional to the power factor.

Iterative Computation

The presented DM consists of three main design stages of which each can be divided into three sub-steps. The variables are determined according to the statements given in Sec. 3.5 and Sec. 4.2.2 for IM sizing issues and Sec. 3.6 and Sec. 4.2.2 for PMSM sizing issues.

Design Stage 1: Fig. 4.12 illustrates the 1st design stage and gives a brief overview on its consecutive steps. The DM uses a predefined structure with 36 input variables shown in Tab. 4.2.

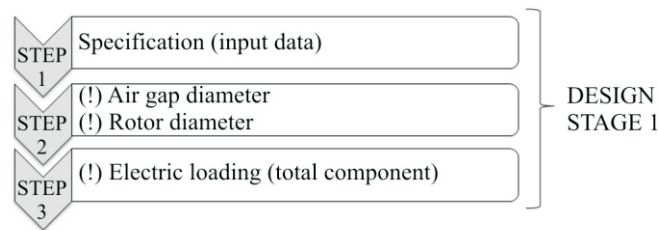


Figure 4.12: Illustration of the 1st design stage and the listing of the corresponding computation steps. The expression (!) denotes an executional step, having a (?) means that the algorithm decides on a predefined tolerance limit which step to proceed.

The iterative computation of the machine dimensions and its corresponding operational characteristics regionally starts right in the middle of the air gap

(2nd sub-step). The algorithm therefore has to have at least three input parameter in order to be able to calculate an air gap radius r_δ . These parameters are:

- Nominal design torque T_n [Nm]
- Nominal shear force density σ_n [$\frac{\text{N}}{\text{m}^2}$]
- Stack length l_{fe} [m]

The shear force density σ_n and the stack length l_{fe} are determined in accordance with Sec. 4.2.2. Referring to Equ. (4.17), the air gap diameter d_δ has squared influence on the design torque T . This statement is emphasized by Equ. (4.102), as the air gap radius r_δ is once introduced by the torque building cylinder area A_{fe} and once by the lever arm to the shaft.

$$T_n = \frac{d_\delta}{2} F_\delta; F_\delta = \sigma A_{fe}; A_{fe} = d_\delta \pi l_{fe} \quad (4.100)$$

$$T_n = \frac{1}{2} d_\delta^2 \sigma \pi l_{fe} \quad (4.101)$$

$$d_\delta^2 = \frac{2T_n}{\sigma_n \pi l_{fe}} \quad (4.102)$$

In order to compute the inner and outer diameters of stator and rotor respectively, the air gap size w_δ needs to be determined. This is frequently done by empirical data which have been gained over years. An empirical reference value of the expecting air gap size w_δ can be given by [SIN04]:

$$w_\delta = \frac{1}{4} \frac{\sqrt[4]{P_n 10^{-3}}}{1000} \quad (4.103)$$

The air gap size w_δ of the IM results in 0.4mm for a nominal power of $P_n = 5.25\text{kW}$. The lower bound of the air gap size w_δ is surely affected by tolerances resulting from manufacturing processes. Its choice also depends on the resulting rotor dimensions and the maximum mechanical speed of the motor drive. With small air gap sizes, air friction and supplementary load losses increase [BIK99].

The 3rd sub-step considers the evaluation of the electric loading A . Referring to Equ. (4.17), the peak value of torque component \hat{A}_q can be evaluated by Equ. (4.104). The magnetizing component \hat{A}_d is not known so far. In order to determine a valid start value, \hat{A}_d is estimated assuming a relative permeability of $\mu_{fe} = \infty$ (cf. Equ. (4.105)). The entire electric loading A is given by the quadratic sum of A_d and A_q .

$$\hat{A}_q = \frac{2\sigma_n}{\hat{B}_\delta}, \quad (4.104)$$

$$\hat{A}_d = p \frac{1}{\xi_w} \frac{1}{r_\delta} \int H_\delta dl, \quad (4.105)$$

$$A = \sqrt{A_q^2 + A_d^2}. \quad (4.106)$$

Design Stage 2: The 2^{nd} design stage considers again three sub-steps which are executed iteratively. The variable n represents the iterative counter.

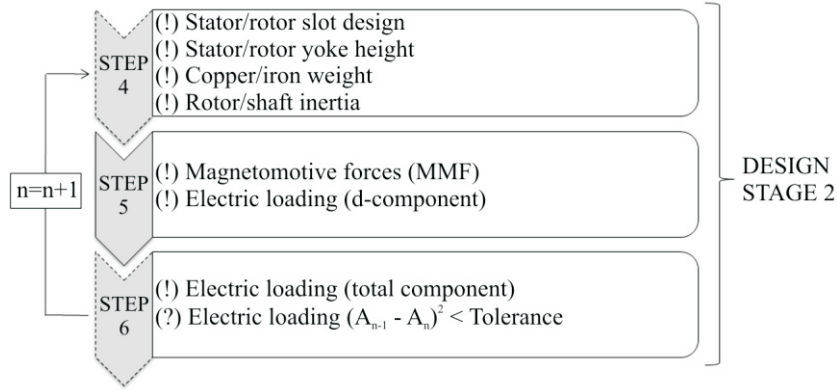


Figure 4.13: Illustration of the 2^{nd} design stage and the corresponding computational sub-steps.

The DM considers parallel sided teeth only, hence, the slot form is considered to be trapezoidal. The 1^{st} sub-step (step 4) concentrates on the computation of the slot design. Thus, the cross-sectional area of the stator slot A_{slS} and the rotor slot A_{slR} are evaluated considering the electric loading A , the air gap diameter d_δ , the slot numbers $Q_{S,R}$ and the individual slot current densities $J_{sl} = J_{cu} k_{sl}$ of stator and rotor:

$$A_{slS} = \frac{A}{J_{slS} Q_S} d_\delta \pi \quad (4.107)$$

$$A_{slR} = \frac{A}{J_{slR} Q_R} d_\delta \pi \quad (4.108)$$

The computation of the slot height h_{slS} is subsequently given for the stator only. Thus, the variable h_{slS} is determined by an algebraic equation evaluating the slot opening height h_{rS} , the slot number Q_S and the relative tooth width relation $\frac{w_t}{w_{sl}}$. The mentioned parameters represent design specifications, see Tab. 4.2. Their individual values are chosen according to the statements given in Sec. 4.2.2 and Sec. 4.2.3. The equations read

$$0 \leq \frac{w_{tS}}{w_{slS}} \leq 1, \quad (4.109)$$

$$w_{tS} = \frac{(d_{iS} + h_{tS})\pi}{Q_S} \frac{w_{tS}}{w_{slS}}, \quad (4.110)$$

$$w_{slS^1} = \frac{(d_{iS} + 2h_{rS})\pi}{Q_S} \left(1 - \frac{w_{tS}}{w_{slS}}\right), \quad (4.111)$$

$$A_{slS} = \frac{(w_{slS^1} + w_{tS})}{d_\delta} h_{slS}^2 + w_{slS^1} h_{slS}, \quad (4.112)$$

with w_{slS^1} being the slot width at the bottom of the slot trapezoid, see Fig. 4.7. The yoke flux densities $\hat{B}_{yS,yR}$ are evaluated by the specification of $\frac{B_y}{B_t}$. Their individual values should be chosen according to Sec. 4.2.2. The corresponding yoke heights $h_{yS,yR}$ are computed according to Equ. (4.80).

The axial coil width for the stator winding (distributed) and the rotor winding (squirrel cage) are estimated by the empirical formulas given in Equ. (4.113) and Equ. (4.114).

$$l_{axS} = 2w_{slS}q_S \quad (4.113)$$

$$l_{axR} = w_{slR}q_R \quad (4.114)$$

The moments of inertia of the rotating parts are evaluated by their individual diameters and masses. Copper and iron weights of the active components can now be calculated by the corresponding volumes and material densities.

The 2nd sub-step (step 5) concentrates on the computation of the magnetic circuit and evaluates Equ. (4.83) to Equ. (4.88) for the determination of the MMFs. The magnetic potential differences are strongly related to the previously calculated dimensions of teeth and yokes, their flux densities together with their corresponding magnetic excitations. In fact, having $n > 1$, the magnetizing electric loading \hat{A}_d can now be given by

$$\hat{A}_d = \frac{\hat{\theta}}{2} p \frac{1}{\xi_w} \frac{1}{r_{iS} + \frac{h_{slS}}{2}}. \quad (4.115)$$

The 3rd sub-step (step 6) concentrates on the computation of the overall electric loading A since the magnetizing component A_d might have changed for $n > 1$. The algorithm terminates if the quadratic difference of two consecutive computed electric loadings $(A_{n-1} - A_n)^2$ is lower than the tolerance limit. An excess of the tolerance limit will automatically cause a reentrance on step 4.

Design Stage 3: The 3rd design stage acts as post-processing unit evaluating the previously computed sub-steps. The parameters are transformed to phase values.

The 1st sub-step (step 7) considers the computation of the magnetizing current component I_d , the torque building current component I_q and the corresponding resistances and reactances of the phases. The power factor $\cos(\varphi)$ is evaluated by means of analyzing the corresponding relations of currents and voltages of a conventional IM phase circuit diagram.

The 2nd sub-step (step 8) concentrates on the loss computation examined in Sec. 4.1.5. The losses at the design point are given for steady state condition

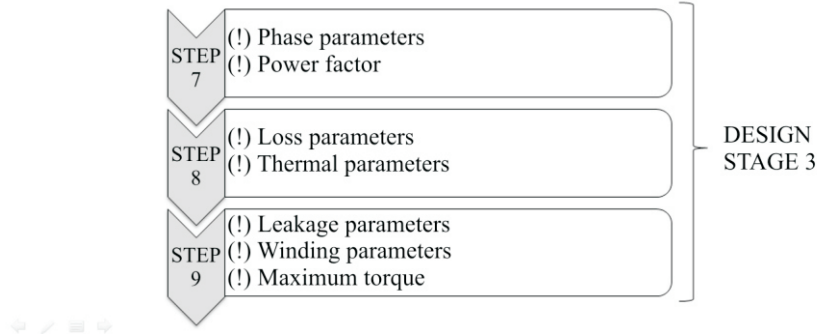


Figure 4.14: Illustration of the 3rd design stage and the listing of the corresponding computational steps.

using the thermal model being introduced in Sec. 5.3. The thermal model provides information of the thermal utilization of the machine under the given design specifications and reports whether a continuous operation at nominal power P_n is thermally stable. A non-thermally stable input specification will not automatically cause a reentrance on step 4. The adjustment of the input parameters needs to be done by the design engineer. The evaluation of optimization potentials by energy efficient control methods is considered to be part of this sub-step. Information on this issue is provided in Chap. 5.

The last sub-step (step 9) focuses on the analysis and computation of the leakage parameters and evaluates the resulting winding parameters and pull-out torque according to Sec. 4.1.6.

Discussion

Sec. 4.2.3 introduced a DM having a special focus on IM sizing issues. The presented DM uses the symmetry of design. Therefore, the computation of the magnetic circuit is reduced on one single pole which makes this concept of modeling very efficient and time-saving concerning computing time. Tab. 4.2 shows the design specification of the presented IM taking 36 input variables. The resulting machine characteristics are given by Tab. 4.3 to Tab. 4.6.

The electric loading A represents the main sizing parameter. Its computation is split up into the individual determination of a torque component A_q given by Equ. (4.104) and a magnetizing component A_d shown by Equ. (4.105) and Equ. 4.115. Although Equ. (4.78) to Equ. (4.88) are not impressively new for MMF calculation, their evaluation has been prepared to a term easing the determination of A_d . The DM turned out to be very time efficient. Considering the IM specifications in Tab. 4.2, the DM takes $n = 15$ iterations at a tolerance limit of 10^{-6} terminating in a total time of 13.1s.

Although an air-cooled IM has been used as sizing examples, the presented DM and the given equations of Sec. 4.2 do not reflect sizing issues of air-cooled IMs only. They are certainly valid for water cooled machines too. However, machine sizing focusing water cooling requires at least one basic thermal parameter set in order to decide on a thermal stable input specification. This eventually requires a redesign of an existing water-cooled machine for identifying their heat transfer coefficients (cf. Sec. 5.3).

Results and Evaluation

In order to demonstrate the correctness of the presented DM, the given IM sizing example has entirely been computed by the electric motor manufacturer THIEN eDrives GmbH. THIEN eDrives GmbH has more than 60 years of practical experience in motor sizing of IMs. Hence, their development tools have grown since then. THIEN eDrives GmbH uses an algebraic approach analyzing harmonics up to the 4th order.

The subsequent content analyzes the DM results and compares them with those of THIEN eDrives GmbH. The goal of the present section is to achieve a qualification of the given approach by determining the deviation of the DM results with those of an electric motor manufacturer.

Comparison	DM	THIEN eDrives GmbH
	Electric loading [$\frac{A}{m}$]	
Electric loading A_d	15187	16446
Electric loading A_q	21101	21100
Electric loading A	25998	26752
	Parameter [-]	
Rated current I_n [A]	27.4	27.7
Rated voltage U_n [V]	167	167
Power factor $\cos(\varphi)$ [-]	0.79	0.78
No-load current I_d [A]	15.5	15.2
Induced voltage U_d [V]	89.4	87
Reactance X_d [Ω]	5.77	5.78
Inductance L_d [mH]	9.18	9.19

Table 4.3: Comparison of the DM results - electric loadings, induced voltages, magnetizing parameters.

Referring to Tab. 4.3, the magnetizing electric loading A_d of the DM is lower compared that computed by THIEN eDrives GmbH. The presented DM represents a fundamental wave approach, contrary to that, THIEN eDrives GmbH computes harmonics up to the 4th order. Thus, the computed values naturally differ from each other resulting in a lower MMF and therefore lower A_d component for the DM result. The computed torque components A_q are very close

to each other. In fact, this is quite obvious as the shear force density σ_n and the air gap flux density B_δ must be equal for the given torque output T_n (cf. Equ. (4.104)).

Comparison	DM	THIEN eDrives GmbH
	Dimension [mm]	
Inner stator diameter r_{iS}	103	103
Stator slot height h_{slS}	15.3	17
Stator slot width w_{slS}	7.9	6.9
Stator yoke height h_{yS}	15	18.6
Outer stator diameter r_{oS}	164	170
Outer rotor diameter r_{oR}	102.2	102.2
Rotor slot height h_{slR}	12.8	17.9
Rotor slot width w_{slR}	4.9	4.7
Rotor yoke height h_{yR}	13.9	14.2
Shaft diameter d_{oS}	38	38
Stator coil width (axial) l_{axS}	25	25/35
Rotor coil width (axial) l_{axR}	14.3	11
	Area [cm²]	
Stator surface A_S	412	427
Rotor surface A_R	257	257
Cooling surface A_{cS}	1566	1623
	Mass [kg]	
Copper (stator) m_{cuS}	2.3	2.5
Iron (stator) m_{feS}	6.0	6.6
Aluminium (rotor) m_{alR}	0.7	0.6
Iron (rotor) m_{feR}	3.3	3.4

Table 4.4: Comparison of the DM results concerning component sizes and weights.

Focusing the resulting dimensions, the DM gives plausible results. The DM computes a slightly lower outer stator diameter of 164mm, mainly caused by a lower computed stator yoke. The DM uses Equ. (4.78) and Equ. (4.82) as primary equations for the evaluation of the yoke heights h_y . Hence, they are strongly related to the rated machine flux ϕ_n . In fact, the machine flux ϕ_n might be too high to some degree due to an insufficient consideration of the leakage flux ϕ_l . However, leakage flux computation is a thing of its own. The present work does not focus on a detailed leakage modeling as there are many discussions about different approaches among experts.

The comparison of the rotor slot dimensions differs more significantly. THIEN eDrives GmbH computed drop-shaped slots which cause the slot height h_{sl} to be larger due to a tapered shape. Contrary to that, the DM uses parallel teeth resulting in shorter trapezoidal slot shapes. The computed axial coil widths w_{axS} of the stator winding have equal values on both sides of the machine. They have

been computed by an empirical formula presented in Equ. (4.77). Practically, they differ from each other depending on the mounting of the terminal box. The side moved towards the terminal box has a slightly higher axial width due to the connection of the parallel branches and the integration and connection of the phases with the wires. This generally requires some additional width in axial direction which can be given by approximately 10mm at a maximum for the distributed stator winding.

The computed copper weight m_{cuS} of the stator is too small, mainly caused by a lower resulting axial coil width w_{axS} at the DM. The slightly lower stator diameter of 164mm even causes the iron weight to be smaller than that computed by THIEN eDrives GmbH. However, the rotor weights are close to each other.

Comparison	DM	THIEN eDrives GmbH
	Loss [W]	
Stator winding P_{cuS} (124°C)	372	361
Stator iron P_{feS}	157	163
Rotor cage P_{alR} (161°C)	172	158
Rotor iron P_{feR}	0	50
Mechanical loss P_m	139	141
Supplementary load loss P_{add}	63	67
Total loss P_{total}	903	940
Relative loss $P_{rel} = \frac{P_{total}}{A_{eS}}$	5765	5789
Machine efficiency η_n [%]	85.3	84.8

Table 4.5: Comparison of the DM results concerning component losses at thermal steady state condition.

The current depending losses of stator P_{cuS} and rotor P_{alR} respectively differ from those of THIEN eDrives GmbH by more than 10W. Referring to Tab. 4.6, the DM results of the stator resistances R_S as well as the rotor resistances R_R are too high. In case of the stator resistance R_S , the mean winding length l_w might be computed incorrectly. However, a more accurate computation of l_w tend to be difficult as the computation of l_w is related to the assembling of the winding topology too. Considering the rotor cage, the pitch circle of the short-circuit ring is assumed to be in the middle of the rotor slots. As mentioned previously, the DM causes a lower height of the rotor slot. Referring to Equ. (4.31), smaller slot heights cause the resistance of the short-circuit ring R_r to increase leading to a slightly higher overall rotor resistance R_R .

The fundamental wave approach of the DM naturally causes the iron losses to be lower at the stator, iron losses in the rotor are close to zero. The constants given for the mechanical and the supplementary load losses did not achieve a good correlation with that of THIEN eDrives GmbH. Hence, their constants C_m and C_{add} have been recalculated which resulting in $C_m = 52$ for the mechanical losses and $C_{add} = 0.012$ for the supplementary load losses. The overall machine

efficiency at the design point results in 85.3% for the DM and 84.8% at THIEN eDrives GmbH.

The leakage parameters represent the results given by the equations of Sec. 4.1.6. The given inductances have been transformed to their reactances and are summed up for stator and rotor respectively. It can be seen, that the analyzed values given by the DM are smaller than those computed by THIEN eDrives GmbH. However, a more accurate computation requires a more detailed look into leakage computation which is not the goal of the current thesis. The lower leakage parameters cause a higher pull-out torque which results in 61Nm for the DM and 56Nm at THIEN eDrives GmbH.

Comparison	DM	THIEN eDrives GmbH
	Value [Ω]	
Stator resistance R_S (124°C)	0.165	0.157
Stator leakage reactance X_S	0.248	0.294
Rotor resistance R_R (161°C)	0.123	0.116
Rotor leakage reactance X_R	0.360	0.355
	Parameter	
Turns per phase ω_{ph} [-]	60	60
Winding factor ξ_w [-]	0.92	0.902
Coil pitch τ_{cp} [mm]	107.8	-
Skew angle γ [°]	10.4	-
Pull-out torque T_{po} [Nm]	61	56
Pull-out slip s_{po} [-]	19	23
Pull-out speed n_{po} [rpm]	2320	2310

Table 4.6: Comparison of the DM results concerning winding and pull-out torque parameters.

4.2.4 Surface Permanent Magnet Synchronous Motor Design

The DM design stages of the PMSM are quite close to those of the IM. Thus, the current section will not address the same aspects as in Sec. 4.2.3, as many of the given approaches are equally valid for the PMSM. Sec. 4.2.4 therefore concentrates on design stage 2 and emphasizes the differences of a DM focussed on PMSMs.

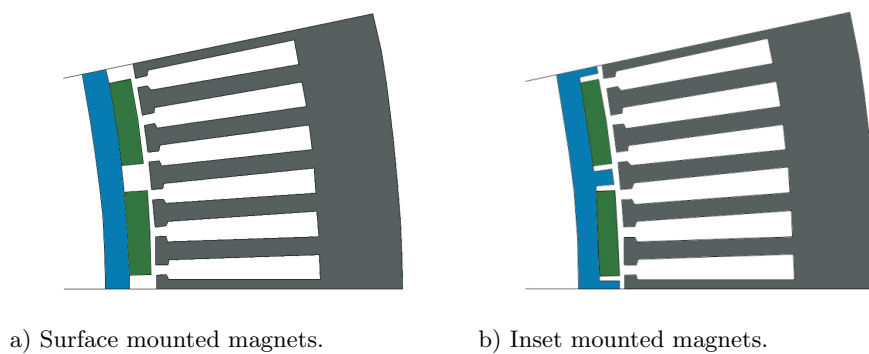


Figure 4.15: Different magnet design configurations of surface mounted PMSMs having $2p = 30$ poles [LS04].

Assumptions

The advantages of PMSMs with buried magnet configurations, like flux concentration, demagnetization protection or mechanical strength, are well-known. However, they are a world of their own and will not be investigated within this section. The given PMSM sizing example concentrates on a four-pole inner rotor configuration with inset mounted magnets, see Fig. 4.15b. The corresponding equations associated with PMSMs having surface mounted magnets are mentioned too. Acting forces on the magnets will not be examined. The stator uses 36 slots representing a slot number per pole and phase of $q_S = 3$.

Magnetic Circuit

Referring to Sec. 4.2.3, the introduced concept of modeling uses the symmetry of design. Fig. 4.17 therefore shows the magnetic circuit over one single pole corresponding to a mechanical angle of $\varphi_m = \frac{\pi}{p}$. The shown variables are the same as for the IM sizing example. The pole shown in Fig. 4.17 has a magnet coverage of 95%. The main path of integration is depicted by the white line (dotted) which is in the middle of the teeth and yokes respectively.

According to the statements given in Sec. 3.6.2, PMSMs have different permeances along the mechanical angle φ_m . These variable permeances normally cause the voltage equations to be very complex. Thus, as far as the operation of the PMSMs is concerned, it is beneficial to introduce a rotor fixed coordinate system. Three-phase values are thereby reduced on two operation values (d-,q-axis) being orthogonal to each other, see Fig. 4.16. The introduced transformation is known as “Park-Transformation” and was already introduced in 1929. The positive d-axis points along the main magnetization direction of a north pole, the corresponding q-axis is shifted by an electric angle of $\frac{\pi}{2}$ [FIS06].

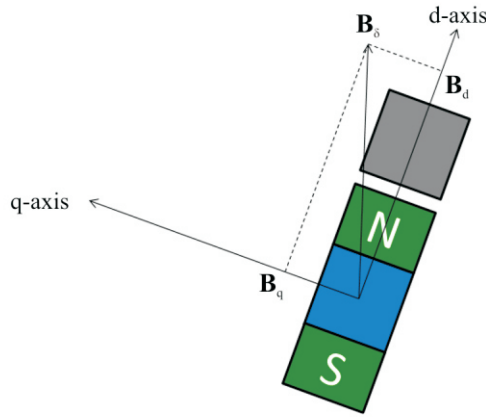


Figure 4.16: Illustration of the d- and q-component of the air gap flux density B_δ .

Unlike IMs, the sinusoidal air gap flux density \hat{B}_δ of the PMSM is introduced by the rotor magnets. However, the computation of the machine flux ϕ_n and the corresponding local flux densities \hat{B}_t and \hat{B}_y introduced in Sec. 4.2.3 are equally valid for the PMSM design approach. Thus, Equ. (4.78) to Equ. (4.82) represent the basis for the subsequent evaluation of the MMFs. Magnetic load shedding of teeth is not considered.

In accordance with the illustration of d- and q-axis, the computation of the MMF θ is split up into two components. The d-component θ_d considers the magnetization characteristic along the d-axis. The stator cross field θ_q focuses on the MMF in q-direction. Equ. (4.116) to Equ. (4.128) show the evaluation of θ_d , θ_q and the determination of B_d and B_q respectively. The equations read:

$$\theta_d = \int H_{yS} dl + \int H_{yR} dl + 2 \left(\int H_{tS} dl + \int H_\delta dl \right) + H_m h_M \quad (4.116)$$

$$\theta_q = \int H_{yS} dl + \int H_{yR} dl + 2 \left(\int H_{tS} dl + \int H_\delta dl \right) \quad (4.117)$$

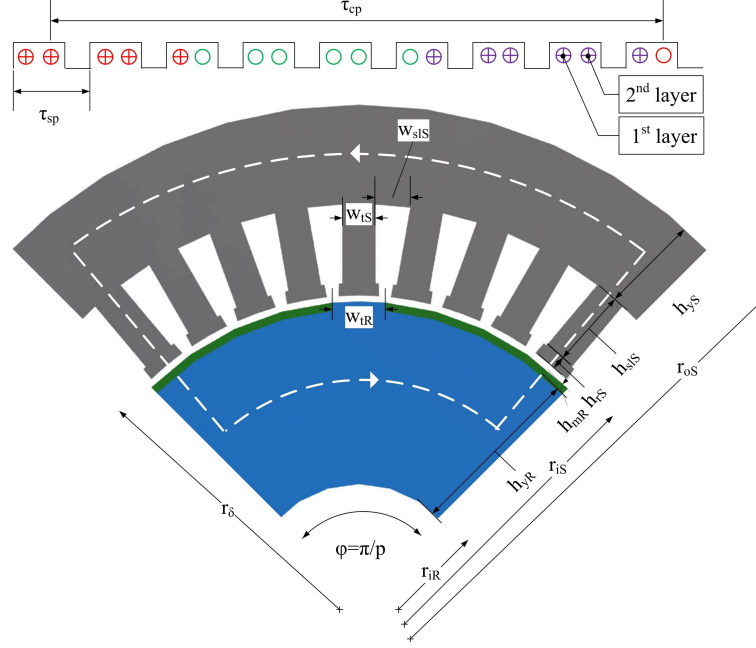


Figure 4.17: Magnetic circuit, stator and rotor segment with parallel teeth over a symmetrical pole pitch.

with the components

$$\begin{aligned}
 \int H_{yS} dl &= \int_{-\frac{\pi}{2}}^{\frac{\pi}{2}} \frac{\hat{B}_{yS}}{\mu_{fe}} \left(\frac{r_{oS} + r_{iS} + h_{tS}}{2} \right) d\varphi = \int_{-\frac{\pi}{2}}^{\frac{\pi}{2}} \frac{\hat{B}_{yS}}{\mu_{fe}} \left(r_{oS} - \frac{h_{yS}}{2} \right) d\varphi =, \\
 &= \left(r_{oS} - \frac{h_{yS}}{2} \right) \sum \frac{\hat{B}_{yS}}{\mu_{fe}} \Delta\varphi =, \\
 &= \left(r_{oS} - \frac{h_{yS}}{2} \right) \sum_{k=-\frac{N}{2}}^{\frac{N}{2}} \frac{\hat{B}_{yS}}{\mu_{fe}} \cos \left(\frac{k \pi}{N p} \right), \quad (4.118)
 \end{aligned}$$

$$\int H_{yR} dl = \left(r_{iR} + \frac{h_{yR}}{2} \right) \sum_{k=-\frac{N}{2}}^{\frac{N}{2}} \frac{\hat{B}_{yR}}{\mu_{fe}} \cos \left(\frac{k \pi}{N p} \right), \quad (4.119)$$

$$\int H_{tS} dl = \frac{\hat{B}_{tS}}{\mu_{fe}} h_{tS} = \frac{\hat{B}_{\delta}}{\mu_{fe}} \frac{w_{slS} + w_{tS}}{w_{tS}} h_{tS}, \quad (4.120)$$

$$\int H_{\delta} dl = \frac{\hat{B}_{\delta}}{\mu_0} w_{\delta}, \quad (4.121)$$

$$\theta_d = \int \hat{A}_d dl_\delta - H_m h_m, \quad (4.122)$$

$$= \underbrace{\hat{A}_d \left(r_{iS} + \frac{h_{tS}}{2} \right) \int_0^{\frac{\pi}{p}} \sin(p\varphi_m) d\varphi_m}_{\theta_w} - \underbrace{H_m h_m}_{\theta_m}, \quad (4.123)$$

$$\theta_q = \int \hat{A}_d dl_\delta, \quad (4.124)$$

$$= \underbrace{\hat{A}_d \left(r_{iS} + \frac{h_{tS}}{2} \right) \int_0^{\frac{\pi}{p}} \sin(p\varphi_m) d\varphi_m}_{\theta_w}. \quad (4.125)$$

Permanent magnets are typically driven within the second quadrant which means that their characteristic working point is within negative field strengths ($H_c < 0$). As long as there is no influencing external magnetic field, the magnets are operated in one single working point. The operating quadrant is known as demagnetization range.

The air gap flux density B_d along the main magnetization direction (d-axis) is given by the MMF θ_d shown in Equ. (4.123). Considering one single working point at constant torque region ($n < n_n$) might cause \hat{A}_d and therefore θ_w to be zero. However, operating PMSMs within their field weakening regions ($n > n_n$) requires $A_d > 0$. The corresponding relations between the machine flux characteristic ϕ and the magnetizing component I_d have already been introduced in Sec. 3.6.2.

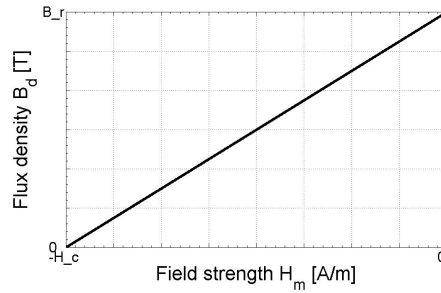


Figure 4.18: Typical operation range of permanent magnets. Reaching H_c causes the magnets to demagnetize.

The rotor magnet height h_m is determined along the d-direction equalizing the magnetic excitation θ_w with zero. According to the statements given in Sec. 3.6.2, the computation of the demagnetization characteristic requires $\theta_w > 0$. The introduced equations are based on a linear characteristic between the remanence flux density B_r and the coercive field strength H_c , shown in Fig. 4.18.

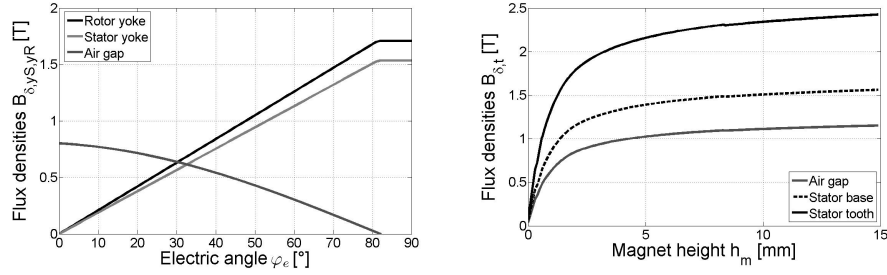
The corresponding equation for the determination of H_m reads:

$$-H_m = \frac{\theta_d - \theta_w}{h_m} \begin{cases} \theta_w = 0 & h_m \\ \theta_w > 0 & \text{demagnetization range} \end{cases} \quad (4.126)$$

Thus, the flux density components $B_{d,q}$ can be determined by:

$$B_d = B_r \left(1 - \frac{H_m}{H_c} \right) = B_\delta - k_0 \lambda_d A_d \quad (4.127)$$

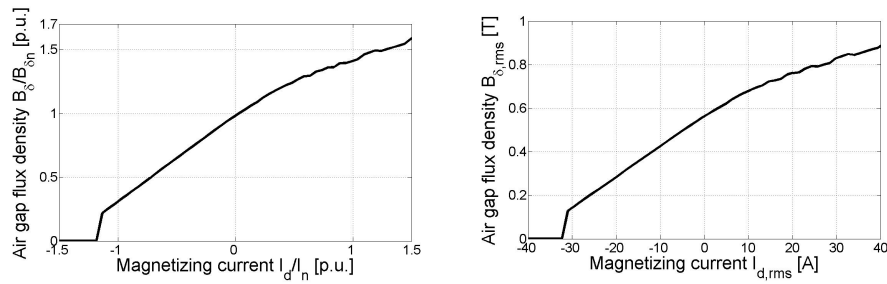
$$B_q = \underbrace{\mu_0 \frac{\int H_\delta ds}{w_\delta}}_{\text{inset mounted}} = k_1 \lambda_q A_q, \quad B_q = \underbrace{\mu_0 \frac{\int H_\delta ds}{h_m + w_\delta}}_{\text{surface mounted}} = k_1 \lambda_q A_q \quad (4.128)$$



a) Flux densities $B_{\delta,tS,tR}$ versus electric angle φ_e .

b) Flux densities $B_{\delta,t}$ versus magnet height h_m .

Figure 4.19: Local flux densities along the integration path. The flux densities are given along an electric angle of $\frac{\pi}{2}$.



a) Per-unit illustration of magnetizing curve.

b) Air gap flux density B_δ versus magnetizing current I_d .

Figure 4.20: Air gap flux density B_δ as a function of the magnetizing current I_d .

The resulting cross component B_q depends on the magnet design configuration (cf. Equ. (4.128)). Thus, synchronous rotors having inset mounted magnets basically face a smaller air gap size than synchronous rotors with exterior, meaning surface mounted magnets. This causes the reluctance torque T_r of rotors with inset mounted magnets to be higher making this magnet design configuration more beneficial for high speed applications (cf. Sec. 3.6.2).

The torque output T can be given by substituting Equ. (4.127) and Equ. (4.128) into the subsequent analytic equations:

$$T = k_2(B_d A_q + B_q A_d) \quad (4.129)$$

$$T = k_2(B_\delta + (k_1 \lambda_q - k_0 \lambda_d) A_d) A_q \quad (4.130)$$

$$T_n = k_2 B_\delta A_{qn}, B_\delta = k_0 \lambda_d A_{d,max} \quad (4.131)$$

Hence, the relative torque output $\frac{T}{T_n}$ reads:

$$\frac{T}{T_n} = \frac{B_d}{B_\delta} \frac{A_q}{A_{qn}} + \frac{k_1 \lambda_q}{k_0 \lambda_d} \frac{A_d}{A_{d,max}} \frac{A_q}{A_{qn}} \quad (4.132)$$

$$\frac{T}{T_n} = \underbrace{\frac{\phi}{\phi_n} \frac{I_q}{I_{qn}}}_{T_s} + \underbrace{\frac{\lambda_q}{\lambda_d} \frac{I_d}{I_{d,max}} \frac{I_q}{I_{qn}}}_{T_r} \quad (4.133)$$

Equ. (4.133) represents the general relation between the torque output T and its operational characteristics. Given a constant torque output, the synchronous torque part T_s gets lower the higher the reluctance torque part T_r . Differently expressed, the permeance ratio $\lambda = \frac{\lambda_q}{\lambda_d}$ may provide a significant reluctance torque T_r at higher speeds if properly designed. Surface mounted magnet rotors normally have a permeance ratio of around one ($\lambda \approx 1$), inset mounted magnet rotors provide higher permeance ratios $\lambda > 1$. As Equ. (4.127) and Equ. (4.128) implies, the values are strongly related to the local flux densities over the pole pitch, the resulting MMF θ and the choice of the air gap size w_δ .

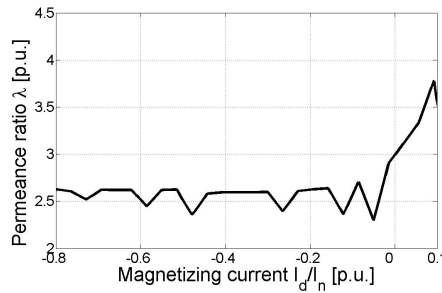


Figure 4.21: Permeance ratio λ at different magnetizing currents $\frac{I_d}{I_n}$ based on the M800-50A sheet.

Fig. 4.21 shows that the permeance ratio λ is more or less constant at a negative field current component I_{d-} . Positive field currents I_{d+} cause λ to increase due to a higher saturation along the magnetization path which lowers the d-directed permeance. Hence, highly saturated motors have a lower d-inductance L_d which basically leads to a higher peak torque capability. Contrary to that, lowering L_d might lead to a high short-circuit current I_{sc} which might constrain the field weakening capability (Sec. 3.6.2).

The rippled characteristic of λ is strongly related to the predefined tolerance limit of the iterative evaluation of the peak values of $\hat{B}_{d1,q1}$ introduced in step 4.2. Therefore, the ripple increases at lower tolerance limits due to higher variances of $\hat{B}_{d1,q1}$. In fact, it is recommendable to specify a lower tolerance limit for a first evaluation of an input specification as the algorithm will terminate faster. The tolerance limit may be adjusted towards lower values in case of a lower variance of the characteristic design values shown in Fig. 3.2.

Considering $\omega_w = 1$, the inductance $L_{d,q,1}$ corresponds to the introduced permeance λ . However, the motor inductance is determined by taking into account the winding setup having ω_w number of turns per slot,

$$L_{d,q,1} = \frac{\phi_n}{I_{sl}} = \lambda_{d,q}, \quad (4.134)$$

$$L_{d,q} = \frac{\psi_d}{I} = \frac{\omega_w \phi_n}{\frac{I_{sl}}{\omega_w}} = \omega_w^2 \frac{\phi_n}{I_{sl}} = \omega_w^2 L_{d,q,1}. \quad (4.135)$$

Iterative Computation

The flow diagram of the iterative computation algorithm for the PMSM is quite similar to that of the IM presented in Sec. 4.2.3. The DM consists of three main design stages of which design stage one and three can be divided up into three sub-steps. These design stages can be taken without any changes, hence, they will not be presented a second time. The 2nd design stage differs by one additional sub-step considering the computation of the magnet heights h_m , see Fig. 4.22.

Design Stage 2: The 1st sub-step (step 4.1) is identical to step 4 of design stage 2 given in Sec. 4.2.3. The 2nd sub-step (step 4.2) focuses on the evaluation of the magnet height h_m . Therefore, an array of different magnet heights is specified evaluating θ_d along the main path of integration. In order to analyze the saturation level of the machine by different magnet heights, the influencing external magnetic field is switched off by means of equalizing A_d with zero ($\theta_w = 0$). The magnetic circuit is determined according to Equ. (4.116) choosing $B_d = B_r$ as a valid start parameter. The local flux densities B_t and B_y are derived from Equ. (4.78) to Equ. (4.80) and Equ. (4.82).

In a first step ($u = 0$), the air gap flux density B_d is assumed to be rectangular, see Fig. 4.23. The corresponding fundamental wave of B_d is subsequently computed by analyzing the Fourier coefficients. The first order coefficient \hat{B}_{d1} can

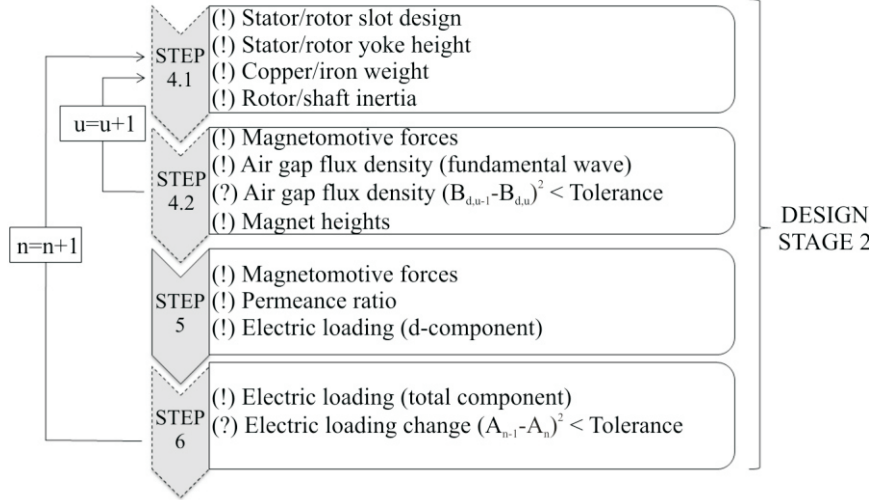


Figure 4.22: Illustration of the 2nd design stage and the corresponding sub-steps.

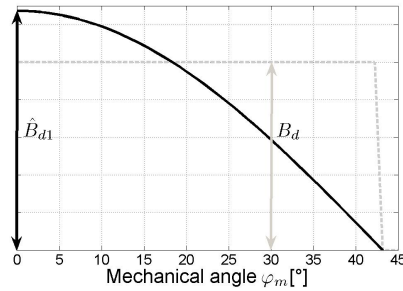


Figure 4.23: Fundamental wave of B_d along the d-direction.

be evaluated by the following equation:

$$\hat{B}_{d1} = \frac{2}{\pi} \int_0^{\frac{\pi}{2p}} \hat{B}_d \cos(p\varphi_m) d\varphi_m \quad (4.136)$$

The iteration loop u terminates if the quadratic difference of the peak value of the fundamental waves $(\hat{B}_{d1,u-1} - \hat{B}_{d1,u})^2$ is within a predefined tolerance limit. The air gap flux characteristic resulting from different magnet heights h_m is shown in Fig. 4.19b. The individual magnet height h_m is evaluated interpolating the air gap flux characteristics taking $B_d \approx B_\delta$ as input parameter, cf. Tab. 4.2.

The 3rd sub-step (step 5) analyzes $\theta_{d,q}$ for $\theta_w > 0$ and evaluates the air gap flux densities $B_{d,q}$ for different demagnetizing electric loadings A_d . The corresponding equations are identical to those previously mentioned. The permeance ratio λ

results by the fraction of d- and q-permeance, $\lambda = \frac{\lambda_q}{\lambda_d}$. Their values are derived from Equ. (4.127) and Equ. (4.128).

$$\lambda_d = \frac{\phi_d}{I_d} \propto \frac{B_d}{A_d} \quad (4.137)$$

$$\lambda_q = \frac{\phi_q}{I_q} \propto \frac{B_q}{A_q} \quad (4.138)$$

The magnetizing component A_d is determined by an interpolation of the demagnetization characteristic taking $B_d \approx B_\delta$ as input variable, see Fig. 4.20. The entire electric loading A is given by the quadratic sum of A_q and A_d shown in Equ. (4.106). The algorithm terminates if the quadratic difference of two consecutive electric loadings $(A_{n-1} - A_n)^2$ is lower than the tolerance limit.

Discussion

The present section concentrated on the 2^{nd} design stage of the DM having a special focus on the computation of the magnet height and the permeance ratio of the PMSM rotor. Corresponding to the IM approach, the present DM uses the symmetry of design. Therefore, the computation of the magnetic circuit is reduced on one single pole which makes this concept of modeling very efficient and time-saving concerning computing time. Tab. 4.2 shows the design specification of the presented PMSM taking 32 input variables. The resulting machine characteristics are given by Tab. 4.7 to Tab. 4.10.

The electric loading A represents the main sizing parameter. Unlike with IMs, the MMFs need to be computed twice. Once for the evaluation of the magnet height neglecting any influence of external fields ($\theta_w=0$) and once for analyzing the permeance ratio λ and the electric loading A assuming $\theta_w > 0$. Compared to the DM of IMs, the present DM takes more steps representing a more computationally-intensive design procedure.

The DM turned out to be very time-saving. Considering the PMSM specifications in Tab. 4.2, the DM approximately takes $u = 4$ iterations for each evaluation of θ_d and h_m at a tolerance limit of 10^{-3} . In case of the outer iteration loop, the DM takes approximately $n = 5$ iterations for each computation of λ at a tolerance limit of $(A_{n-1} - A_n)^2 < 10^{-6}$. The algorithm terminates in a total time of 24.5s.

Although an air-cooled PMSM has been used as sizing examples, the presented DM and the given equations of Sec. 4.2 do not reflect sizing issues of air-cooled PMSMs only. They are certainly valid for water cooled machines too. However, machine sizing focusing water cooling requires at least one basic thermal parameter set in order to decide on a thermal stable input specification. This eventually requires a redesign of an existing water-cooled machine for identifying their heat transfer coefficients (cf. Sec. 5.3).

Results

The designed PMSM has not been computed by THIEN eDrives GmbH, an evaluation of the DM results can therefore not be given. THIEN eDrives GmbH supported the work by giving advice on how to choose the design parameters for air-cooled PMSMs. The corresponding statements have already been given in Sec. 4.2.2. Because of this, it was possible to analyze the DM results and adapt the design approach for a valid approximation of PMSMs.

Summary	DM
	Magnetic excitation $[\frac{A}{m}]$
Electric loading A_d	3
Electric loading A_q	29564
Electric loading A	29564
	Parameter [-]
Rated current I_n [A]	30.9
Rated voltage U_n [V]	122.5
Power factor $\cos(\varphi)$ [-]	0.89
Induced voltage U_d [V]	63.1
d-Reactance X_d [Ω]	0.4
d-Inductance L_d [mH]	0.65
q-Reactance X_q [Ω]	0.89
q-Inductance L_q [mH]	1.46

Table 4.7: Summary of DM results - electric loadings, induced voltages and magnetizing parameters of the permanent magnet synchronous motor.

Summary	DM
	Loss [W]
Stator winding P_{cuS} (138°C)	466
Stator iron P_{feS}	90
Rotor magnet P_{mR} (96°C)	-
Rotor yoke P_{feR}	-
Mechanical loss P_m	80
Supplementary load loss P_{add}	63
Total loss P_{total}	699
Relative loss $P_{rel} = \frac{P_{total}}{A_{cS}}$	5394
Machine efficiency η_n	88.3

Table 4.8: Summary of the DM results concerning component losses at thermal steady state condition.

Summary	DM
	Dimension [mm]
Inner stator diameter r_{iS}	102.8
Stator slot height h_{slS}	14.7
Stator slot width w_{slS}	8
Stator yoke height h_{yS}	17.3
Outer stator diameter r_{oS}	167
Outer rotor diameter r_{oR}	100.8
Rotor magnet height h_{mR}	1.4
Rotor magnet width w_{mR}	74.2
Rotor yoke height h_{yR}	22.9
Shaft diameter d_{oS}	38
Stator coil width (axial) l_{axS}	25
	Area [cm²]
Stator surface A_S	341
Rotor surface A_R	206
Cooling surface A_{cS}	1296
	Mass [kg]
Copper (stator) m_{cuS}	2.1
Iron (stator) m_{feS}	5.4
Magnet (rotor) m_{mR}	0.2
Iron (rotor) m_{feR}	3.2

Table 4.9: Summary of the DM results concerning the computed component sizes.

Summary	DM
	Value [Ω]
Stator resistance (138°C)	0.162
Stator leakage reactance	0.245
	Parameter
Turns per phase ω_{ph} [-]	60
Winding factor ξ_w [-]	0.92
Coil pitch τ_{cp} [mm]	107.2
Skew angle γ [°]	10.4
Correction factor σ_c [-] ($C_l = C_r = 1$)	0.934
Pull-out torque T_{po} [Nm]	67
Polar wheel angle [°]	26
Tilt angle [°]	59

Table 4.10: Summary of DM results concerning winding and pull-out torque parameters.

4.2.5 Summary and Discussion

Design Method

Chap. 4 gives a detailed description of the introduced DM for a time-saving and reliable computation and evaluation of IMs and PMSMs with surface mounted magnets. The DM makes no claim to be a development tool for these kinds of machines but serve as an analytic design tool in conceptual design studies. Due to the time-saving approach, design parameters can easily be changed. Hence, the DM represents an evaluation basis illustrating the effects of the choice of characteristic design parameters (cf. Fig. 3.2) on machine dimensions and efficiencies.

The presented DMs for IMs and PMSMs are aimed at handling a minimum of necessary input specifications taking 36 input variables for the IM and 32 input variables for the PMSM, see Tab. 4.2. The DMs of both machines turned out to be very fast. Indeed, it would not be that serious taking the overall computation time of the IM and PMSM specification into account only and neglect the time effort on their adequate choice. It certainly takes some time to get a reasonable choice of input parameters which strongly depends on the experience of the design engineer. However, in case of knowing the information on IM and PMSM sizing issues given in Sec. 3.5 and Sec. 3.6 together with the choice of design specifications given in Sec. 4.2.2 it should be possible to get a valid parameter set within 30 minutes.

The DMs have been exemplified by air-cooled sizing examples of IM and PMSM. However, the given DMs are valid for each kind of cooling conditions. Designing water cooling machines requires at least one basic thermal parameter set in order to decide on a thermal stable input specification. This eventually requires a redesign of an existing water-cooled machine for identifying their heat transfer coefficients (cf. Sec. 5.3).

Design Comparison

According to the statements given in Chap. 3 and Chap. 4, the design torque T_n represents the main sizing parameter of an electric machine, not the power P_n . Moreover, it was generally concluded that there is a tradeoff between small machine dimensions and high machine efficiencies (cf. Sec. 4.2.2). A compendium of design and operational characteristics for IM and PMSM is given in Tab. A.1 and Tab. A.2.

Tab. 4.11 gives an overview of IM and PMSM results concerning machine sizes and operational characteristics considering the design specifications in Tab. 4.2. The computed values are once given as absolute values and once given relatively to each other. The IM denotes the basis for the comparison, i.e. the 100% value.

According to Tab. 4.11 the PMSM provides significant advantages regarding the resulting machine sizes. Thereby, the PMSM convinces by 12% less active weight

Summary	IM		PMSM	
Stator diameter d_{oS} [mm]	164	100%	167	+2%
Stack length l_{fe} [mm]	80	100%	65	-19%
Active length l_{act} [mm]	130	100%	118	-9%
Active weight ¹ m_{act} [kg]	12.2	100%	10.8	-12%
Torque density [$\frac{Nm}{kg}$]	1.41	100%	1.61	+14%
Moment of inertia ² J_{EM} [gm ²]	4.3	100%	3.1	-28%
Stator loss P_{cuS} [W]	372	100%	466	+25%
Total loss P_{total} [W]	903	100%	699	-23%
Relative loss P_{rel} [$\frac{kW}{m^2}$]	5.8	100%	5.4	-7%
Nominal Efficiency η_n [%]	85.3	-	88.3	+3%

¹ Weight of all electromagnetic parts.

² Moment of inertia of rotor without shaft.

Table 4.11: Comparison of IM and PMSM.

and 9% less active length. Considering the given design torque T_n , the torque density is 14% higher than that of the IM. Due to the fact that the MMFs are mainly provided by the magnets, a high portion of the electric loading A can be used for torque production. This allows a higher shear force density σ_n by means of a shorter stack length. The PMSM has a 19% shorter stack which causes the moment of inertia of the rotor to be 28% lower compared to the IM. The total losses of the PMSM are 23% lower resulting in a rated machine efficiency of 88.3%. The efficiency of the IM is 85.3% and therefore 3% lower.

The relative machine losses P_{rel} consider the fraction of the total losses P_{total} and the stator cooling surface A_{cS} being $5.8 \frac{kW}{m^2}$ for the IM and $5.4 \frac{kW}{m^2}$ for the PMSM. According to [MAN89], air-cooling can be applied up to a value of $6 \frac{kW}{m^2}$. In fact, this shows the high electromagnetic utilization of both machines. IM and PMSM do not reach this upper limit, although the IM is very close to that. Therefore, the higher the value of P_{rel} , the lower the resulting machine efficiency η_n .

In conclusion, from a purely design point of view concerning dimensions, masses and nominal efficiencies, the PMSM provides advantages for the use in automotive traction applications. However, machine efficiencies beyond the design point have not been considered so far. In order to get an insight on this subject, Chap. 5 compares IM and PMSM at their resulting efficiency maps and presents active component temperatures for continuous and short-term operation. Chap. 6 concentrates on an in-wheel motor application within a parallel hy-

brid power train. The machines are respectively compared to each other by their resulting cycle efficiencies within the New European Driving Cycle (NEDC).

5

AC Motor Operation

Chap. 5 presents the resulting efficiencies of the IM and PMSM design specifications introduced in Chap. 4. It gives an overview of their individual advantageous operation ranges and compares their operational characteristics at different control methods. Furthermore, Chap. 5 provides information on the benefit of energy efficient control methods at different operation ranges and presents active component temperatures at continuous and short-term operation.

Chap. 5 is supposed to serve as an additional evaluation basis on how to specify design specifications for a certain automotive traction application. It is part of design stage three introduced in Sec. 4.2.3 and Sec. 4.2.4.

5.1 Assumptions

The individual optimization potentials of IM and PMSM are based on their evaluated loss coefficients shown in Tab. 5.1. The computation of minimum machine losses for each load point is implemented by a MATLAB® optimizer [MAT11]. Different control methods typically change the dynamic behavior of a machine, however, research work on converter modeling and machine dynamics is not considered.

According to [OVE04a], ten different operation modes (S1...S10) are distinguished. The presented active component temperatures are based on an external ventilation and will be given for continuous operation (S1) and short-term operation (S2) only. The designed machines use the highest insulation class “H”

having a limit temperature of 180°C. The overtemperature characteristic will be given for the stator winding and the rotor cage/magnet.

Loss Coefficients	IM	PMSM
Stator copper $C_{cuS} = C_{S1}$ [-]	371.8	473.4
Stator iron C_{feS} [-]	157.4	90.4
Rotor cage $C_{alR} = C_{R1}$ [-]	260.7	-
Rotor iron C_{feR} [-]	3.9	-

Table 5.1: Per-unit loss coefficients of the designed IM and PMSM.

5.2 Energy Efficient Control Methods

Automotive applications normally require motors to be operated within wide speed ranges facing different loads. Hence, conventional control structures should be reconsidered and adapted according to the application scenario of the motors.

Energy efficient control methods concentrate on taking a minimum of necessary power for a given load. As far as the constant torque region is concerned, two different control methods can be distinguished - constant flux (CFC) and variable flux control (VFC) methods¹.

5.2.1 Assumptions

Sec. 5.2.2 and Sec. 5.2.3 do not focus on the introduction of new control approaches of IM and PMSM as there exists many literature upon this subjects². The subsequent sections examine the resulting efficiency maps and optimization potentials of the IM and PMSM design specifications given in Tab. 4.2.

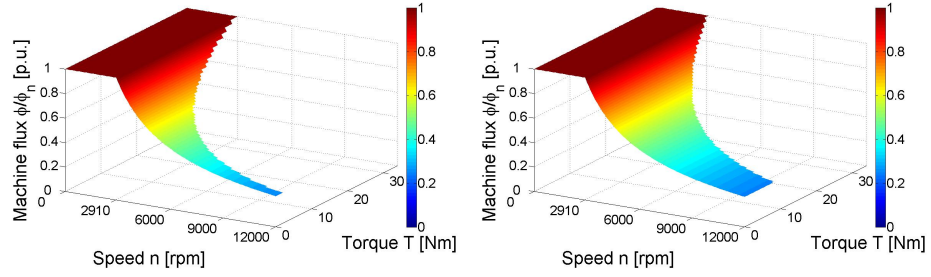
5.2.2 Constant Flux Control Method

Considering constant flux control (CFC), the machine flux $\phi = \phi_n$ is kept constant within constant torque region. As long as the machine is operated below the base speed n_n , CFC can be reduced to a current control of I_q . The control method cannot be applied at constant power region as the induced voltage U_d would exceed the maximum intermediate voltage U_i . Thus, the machine flux ϕ is decreased by approximately $\frac{1}{\omega}$. Because of this, a valid torque output T at the doubled base speed requires the doubled torque building current I_q .

¹The used abbreviations are not literally known among experts, as they represent an arbitrary definition of the author. They characterize the basic control strategy as both definitions can be used for each motor respectively.

²Information on this subject is given in [SUL11], [NL96], [PZZHH04], [CMS+10]

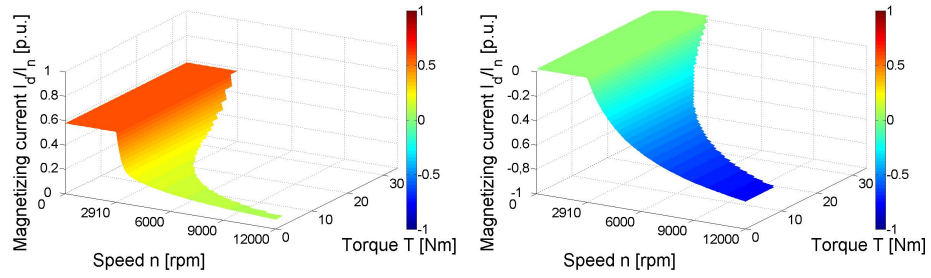
Fig. 5.1 illustrates the per-unit flux $\frac{\phi}{\phi_n}$ of the speed-controlled IM and PMSM introduced in Tab. 4.2. Both machines have different pull-out torque characteristics (cf. Sec. 4.1.7).



a) IM.

b) PMSM.

Figure 5.1: Per-unit illustration of the machine flux at constant flux control.



a) IM.

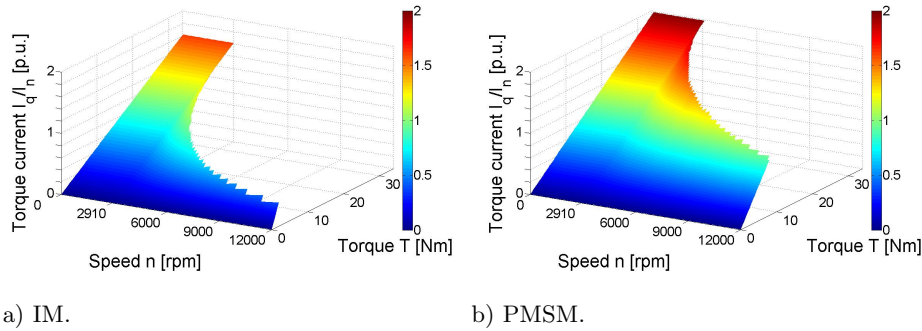
b) PMSM.

Figure 5.2: Per-unit illustration of the magnetizing current as a function of torque and speed.

Fig. 5.2 illustrates the corresponding magnetizing current component I_d . Positive components I_{d+} denote field building currents which are the case at IMs and PMSMs. Negative current components I_{d-} denote field weakening currents which means that they are opposing the machine flux induced by the rotor magnets. Thus, they exclusively happens at PMSMs (cf. Sec. 3.6.2 and Sec. 4.2.4).

In case of the designed IM, the machine flux ϕ needs to be raised by the stator current which requires approximately 58% of the rated current I_n at constant torque region. In fact, the field building current I_{d+} decreases significantly at constant power region due to the highly non-linear magnetization curve given in Fig. 4.10. Doubling the base speed n_n causes I_{d+} to decrease down to 14% of the rated stator current I_n . PMSMs normally have low magnetization currents at constant torque region, as the magnetic excitation is mainly provided by the

magnets (cf. Sec. 3.6.2 and Sec. 4.2.4). However, entering constant power region generally requires additional field weakening current I_{d-} in order to keep the induced voltage U_d within limits. Considering the present PMSM, a flux decline of half of the nominal flux ϕ_n results in a field weakening current I_{d-} of 52% of the overall stator current I_n .

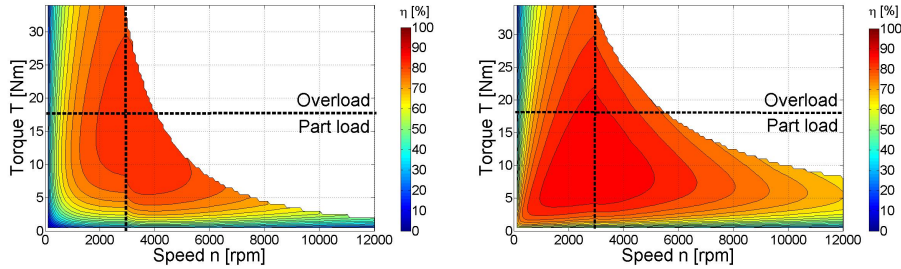


a) IM.

b) PMSM.

Figure 5.3: Per-unit illustration of the torque current over the full torque-speed profile.

Fig. 5.3 represents the torque building current components I_q given in per-unit form. Focusing constant torque region, their characteristic is linear depending on the applied load, hence, the torque output is predominately provided by I_q . A flux decline at constant power region causes I_q to increase slightly.



a) IM.

b) PMSM.

Figure 5.4: Motor efficiencies of the designed electric machines.

Fig. 5.4 shows a comparison of the computed motor efficiencies at CFC and thermal steady state condition. The intersection point (dotted lines) shows the individual design points of the machines. The PMSM shows convincing characteristics at part load region (e.g. $\eta = 87.5\%$ at 5Nm and 1000rpm). The efficiency η becomes generally worse within overload region ($T > T_n$) and field weakening region ($n > n_n$). Contrary to that, the designed IM shows worse

efficiencies within constant torque region, especially at low part load regions. The machine losses within this region tend to be high as the high saturation level is provided constantly. As far as the constant power region is concerned, the IM efficiency increases as the field building current I_{d+} decreases. In fact, the IM has its best characteristic at higher speeds having a maximum efficiency of 87.4% at 14Nm and 3400rpm. Fig. 5.5 shows the individual advantageous operations ranges of IM and PMSM (shaded in green).

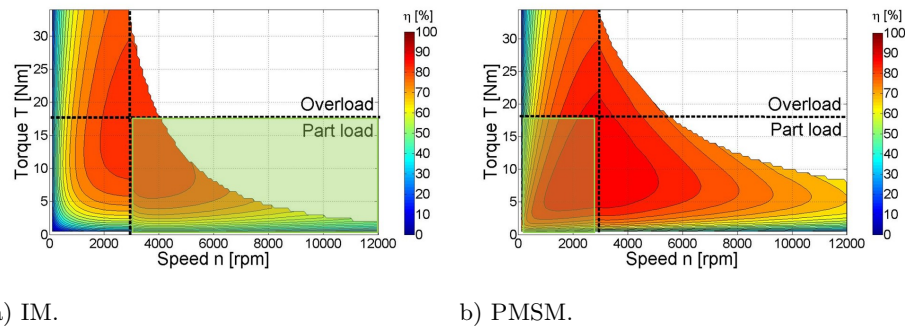


Figure 5.5: Advantagous operation ranges of IM and PMSM.

5.2.3 Variable Flux Control Method

Variable flux control (VFC) is characterized by minimized losses for a given torque output T . Therefore, the control variables $\phi = f(I_d)$ and I_q are determined to get the highest achievable machine efficiency. IMs tend to provide significant optimization potential as the machine flux ϕ and the magnetizing current component I_d can directly be adjusted by the stator current I_n . In fact, part loads do not necessarily require the flux to be controlled on its rated value ϕ_n [NL96].

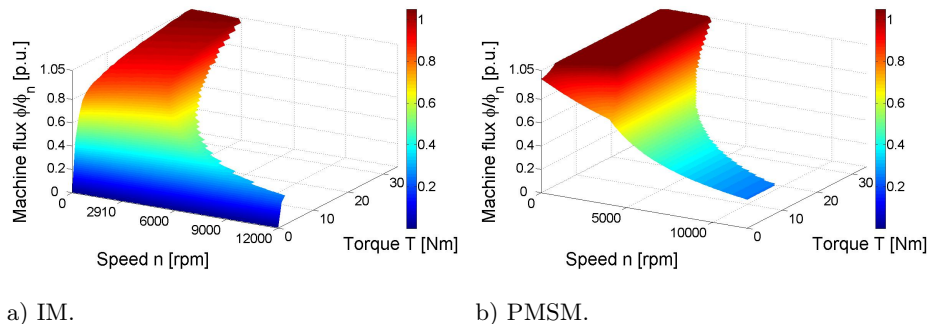


Figure 5.6: Per-unit illustration of the machine flux at variable flux control.

Considering the present IM, VFC causes a flux reduction at part loads which is lower the lower the torque output T , see Fig. 5.6. Therefore, providing half of the rated torque results in 83% of the rated flux ϕ_n for optimized efficiency. A tenth of the rated torque T_n requires no more than 41% of ϕ_n . Loss minimization at PMSMs happens by adjusting the magnetizing current I_d trying to enhance the achievable reluctance torque T_r for a given torque output T (cf. Sec. 4.2.4). The PMSM shows a maximum reluctance torque T_r at a flux decline at very low part load regions, see Fig. 5.6b. The machine flux ϕ is reduced to 79% at 1Nm and 2910rpm. The VFC method is commonly known in industry and is frequently denoted as *Maximum-Torque-Per-Ampere (MTPA)* operation.

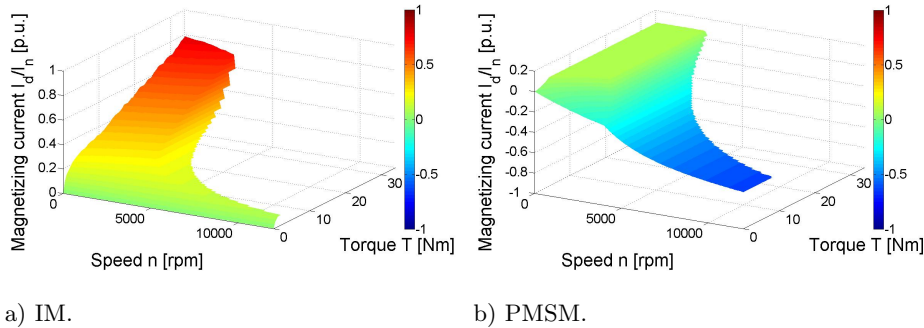


Figure 5.7: Per-unit illustration of the magnetizing current component as a function of torque and speed at VFC.

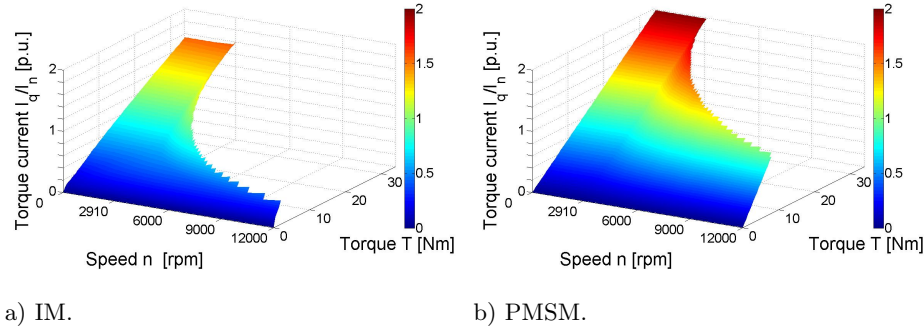
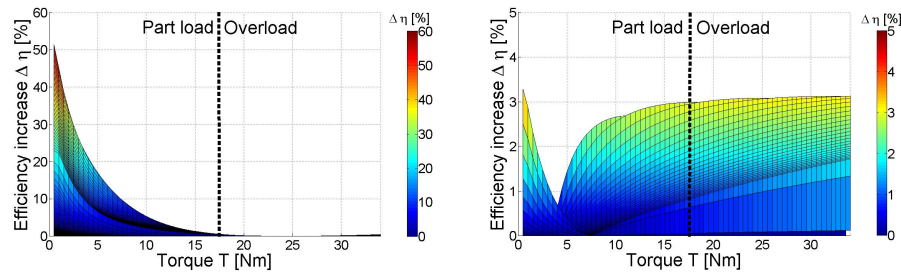


Figure 5.8: Per-unit illustration of the torque building current component over the full torque-speed profile at VFC.

Fig. 5.7 and Fig. 5.8 show the corresponding current components I_d and I_q . The values of the magnetizing currents I_{d+} , I_{d-} depend on the machine flux ϕ . Their relation is given by the individual magnetization curves of IM and PMSM presented in Chap. 4. The rated magnetizing current I_{dn} of the IM is now 43% of the rated current I_n . The maximum torque output T_{max} at the base speed

n_n causes the magnetizing current I_d to be 59% of I_n . The magnetizing currents of the PMSM are low and constant over a wide range at constant torque region. Part load operation causes the field current I_{d-} to be 17% of the rated current I_n at 1Nm and 2910rpm.



a) IM.

b) PMSM.

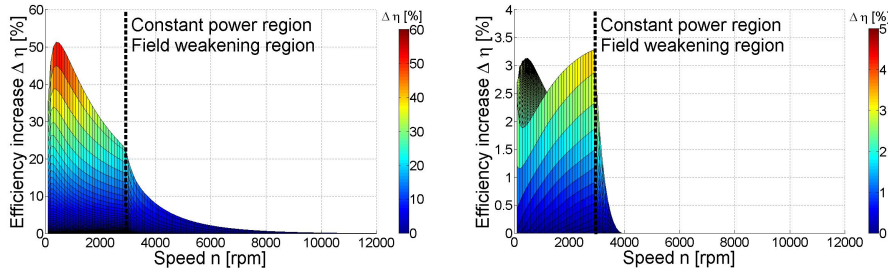
Figure 5.9: Absolute motor efficiency increases at different loads achieved by VFC.

Fig. 5.9 depicts the absolute efficiency increases caused by VFC for the designed machines. Therefore, CFC acts as a reference representing the basic motor efficiency. It is clearly shown that the VFC method has a tremendous impact on the efficiency of both motors.

Considering IMs, the influence is generally higher the lower the load requirements and reaches up to 50% at very low part load conditions. The overload region shows less influence by the VFC method. This is not surprising, as the designed IM is highly utilized in terms of high teeth and yoke flux densities. Raising the machine flux ϕ much higher than the rated flux ϕ_n would result in undue magnetic field strengths. Hence, torques being higher than the design torque ($T > T_n$) are therefore predominately provided by the current component I_q , which is quite similar to the CFC method. Consequently, there can only be achieved a low efficiency increase within the overload region for the IM. The given results and statements are supported by the research work of [ISDK08].

In contrast, the designed PMSM shows a relevant efficiency rise within the entire load range. The maximum efficiency difference is up to 3% at part load region. The resulting values represent less than a tenth of the achieved efficiency increases at the IM. However, this may not lead to misinterpretation as the efficiencies of the PMSM at CFC method are higher by far compared to the IM within constant torque region. The implemented VFC method leads to efficiency enhancements at part load regions and low speeds. In the present case can be achieved efficiency increases up to 3.5% around a speed of 500rpm. Higher speeds cause the efficiency increases to shrink having approximately 1% around the base speed. Fig. 5.10 gives an overview of the absolute efficiency increases at different speeds for both motors.

Generally speaking, the influence of VFC methods on both machines is lower the higher the speed. Entering the field weakening region ($n > n_n$) restricts the flux adjustment possibilities as the flux ϕ needs to be decreased due to the voltage limit. The flux ϕ decreases inversely proportional with the speed. In fact, there exist some optimization potentials for IMs, as the flux ϕ may be further reduced at part load region. Regarding the PMSM, the VFC method causes a very low impact on the losses at constant power region. Both control methods, meaning CFC and VFC, use reluctance torque T_r . However, the flux presettings at constant power region require field currents which are equal for both control methods. Differently expressed, CFC and VFC methods become similar at field weakening entrance. The optimization potential therefore mostly concentrates on constant torque region.



a) IM.

b) PMSM.

Figure 5.10: Absolute motor efficiency increases of the designed motor types at different speeds achieved by VFC.

5.3 Active Component Temperatures

The present section focuses on the analysis of the thermal utilization of active components such as windings, iron stacks and permanent magnets considering the design specifications given in Tab. 4.2. According to Sec. 4.2.3 and Sec. 4.2.4, the presented DMs of IM and PMSM require at least one basic thermal parameter set in order to decide on a thermal stable input specification.

The computation of the active component temperatures is based on a transient thermal model introduced in [TSKT04]. Therefore, the current section will not focus on the verification of the differential equation, but use the previously mentioned work as a basis for identifying the conductive and convective heat transfer coefficient h and k respectively shown in Fig. 5.11. For evaluation reasons, the air-cooled sizing example of the IM has been computed by THIEN eDrives GmbH too. Thus, it was possible to derive a basic air-cooling parameter set by identifying h and k between the modeled thermal mass points. As far as the PMSM is concerned, the heat transfer coefficients of the stator are quite similar

to that of the IM. The corresponding parameters for the rotor have been gained by experimental data from THIEN eDrives GmbH.

Although the heat transfer coefficients have been derived from the air-cooled sizing examples of Sec. 4.2.2, they should be valid for other air-cooled variants of IMs and PMSMs too. Therefore, it should be clearly mentioned that the derivation of a basic parameter set for air-cooled or water-cooled machines needs to be evaluated only once.

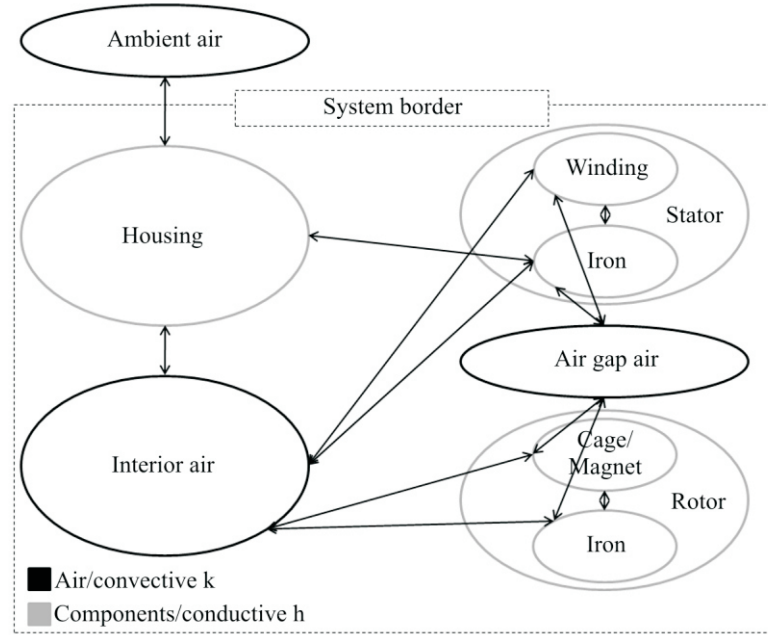


Figure 5.11: Thermal interaction of the active components of the electric machine.

Fig. 5.11 shows the mutual thermal influence of eight thermal mass points being used for the evaluation of the overtemperatures of the active components. According to [OVE04b], the maximum temperature T_{ref} of the ambient air must be lower than 40°C for an altitude of site below 1000m. The temperature rise $\Delta T = T - T_{ref}$ of the active components is given relative to the temperature T_{ref} . The subsequent equation specifies the thermal approach given by [TSKT04]:

$$\underbrace{m_i c_{p,i} \frac{dT}{dt}}_{\text{Stored heat}} = \underbrace{\sum P_{total,i}}_{\text{Generated heat}} - \underbrace{hA_{h,i}\Delta T_{h,i} - kA_{k,i}\Delta T_{k,i}}_{\text{Transferred heat}} \quad (5.1)$$

The variables m_i and $c_{p,i}$ denote the individual masses and the heat capacities of the components. The coefficients h and k represent an average conduction

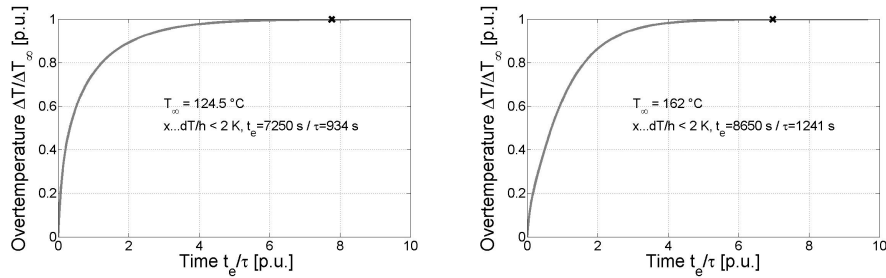
heat transfer coefficient between two different components and an average convection coefficient between the component and the ambient air. The variables $P_{total,i}$, $A_{h,i}$ and $A_{k,i}$ denote the total losses in the active components and the interfacing thermal convective and conductive cross-sections respectively. The expressions $\Delta T_{h,i}$ and $\Delta T_{k,i}$ represent the temperature differences between two coupled thermal masses.

Operation Modes	Applied Power [kW]
Continuous operation S1	5.25 @ 2910rpm
Short-term operation S2	10.5 @ 2910rpm

Table 5.2: Applied power at different operation modes.

5.3.1 Continuous Operation

Having continuous operation (S1), the motors are operated at nominal power P_n causing the machines to reach a thermal steady state condition, see Tab. 5.2. Thermal steady state condition requires ΔT to be below 2K within a time interval of one hour [OVE04a].



a) Stator winding (IM).

b) Rotor cage (IM).

Figure 5.12: Overtemperature characteristic of stator winding and rotor cage at continuous operation (S1).

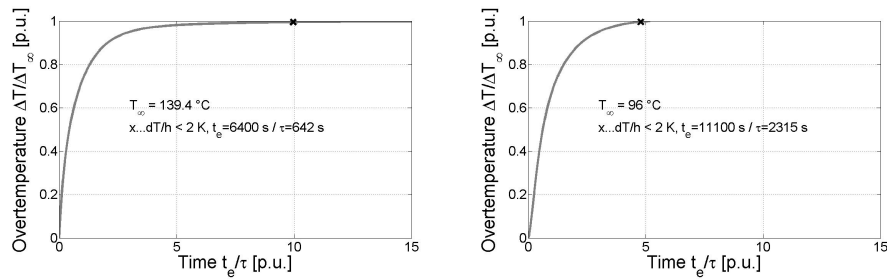
Fig. 5.12 and Fig. 5.13 illustrate the individual overtemperatures ΔT of stator winding and rotor cage/magnet at external ventilation. The heating time constants of the stator winding τ_{hS} and the rotor cage τ_{hR} are computed by solving Equ. (5.1) resulting in an exponential characteristic [GHV03]:

$$\frac{\Delta T}{\Delta T_{\infty}} = 1 - e^{-\frac{t}{\tau_h}} \Rightarrow \tau_h = -\frac{t}{\ln(1 - \frac{\Delta T}{\Delta T_{\infty}})} \quad (5.2)$$

Fig. 5.12b shows a strong thermal strain of the IM rotor cage resulting in a maximum overtemperature ΔT_{∞} of 122°C. The computed steady state temperature

is reached after two hours and 24 minutes, representing a heating time constant τ_{hR} of approximately 21 minutes. The rotor cage and the housing are thermally coupled to each other via at least one additional thermal mass point. In fact, this slows down the heat dissipation causing a higher stored heat energy.

The heat transfer from the stator winding to the housing is obviously better as the stator stack is directly pressed into it. Thus, the maximum overtemperature ΔT_∞ is lower resulting in 84.5°C. The stator winding reaches its thermal steady state condition earlier. The heating time constant τ_{hS} is approximately five minutes lower compared to the rotor cage.



a) Stator winding (PMSM).

b) Rotor magnet (PMSM).

Figure 5.13: Overtemperature characteristic of stator winding and rotor magnet at continuous operation (S1).

According to Sec. 4.2.4, the PMSM is designed to have a higher slot current density J_{sl} compared to the IM. The stator winding of the PMSM is therefore thermally utilized stronger which can be seen by a higher winding temperature rise ΔT_∞ of 99.4°C. Referring to Sec. 4.2.5, the relative losses P_{rel} of the PMSM are $5.4 \frac{\text{kW}}{\text{m}^2}$ which is 7% lower compared to the IM having $5.8 \frac{\text{kW}}{\text{m}^2}$. Thus, the stator winding of the designed PMSM is expected to reach its thermal steady state condition faster in case of a given cooling power. The heating time constant τ_{hS} is approximately five minutes lower compared to the IM.

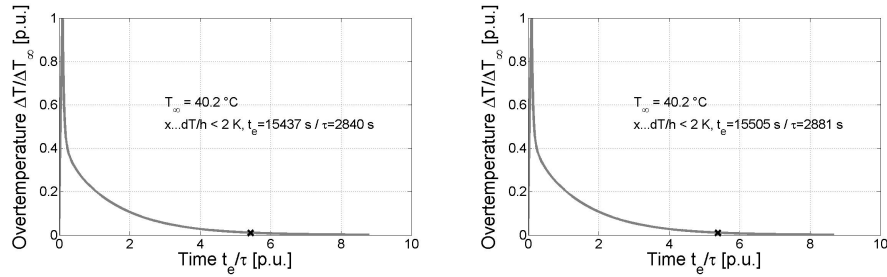
Due to the fundamental wave approach of the DMs presented in Sec. 4.2.3 and Sec. 4.2.4, the magnet and rotor stack temperatures are expected to rise more slowly. The given statement can obviously be seen in Fig. 5.13b, as the absolute temperature rise time t_e of the rotor magnets is nearly twice the time of the stator winding. The maximum temperature rise ΔT_∞ of the magnets can be given by approximately 56°C.

Maximum overtemperatures	IM	PMSM
Stator winding ΔT_∞ [°C]	84.5	99.4
Rotor cage/magnet ΔT_∞ [°C]	122	56

Table 5.3: Maximum overtemperatures for the active components of IM and PMSM.

5.3.2 Short-term Operation

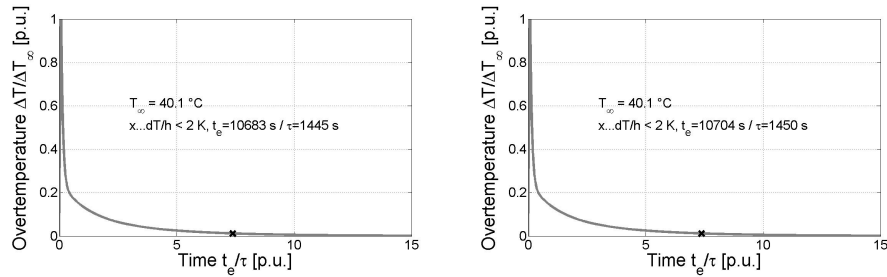
Short-term operation is characterized by maximum power operation P_{max} . Having reached the maximum insulation temperature, the motor goes in power-off state. The duration of an S2-operation does not cause the motor to reach its thermal steady state condition [OVE04a].



a) IM - rotor cage (CFC).

b) IM - rotor cage (VFC).

Figure 5.14: Influence of CFC and VFC methods on overtemperature of rotor cage at short-term operation (S2).



a) PMSM - stator winding (CFC).

b) PMSM - stator winding (VFC).

Figure 5.15: Influence of CFC and VFC control methods on overtemperature of stator winding at short-term operation (S2).

Fig. 5.14 and Fig 5.15 present the overtemperatures ΔT of the thermal critical active components of IM and PMSM based on external ventilation. The figures illustrate the influence of the VFC method on the individual overload capability of the motors, taking the rotor cage for the IM and the stator winding for the PMSM. The corresponding values of $\tau_{cR,cS}$ are based on Equ. (5.1) resulting in [GHV03]:

$$\frac{\Delta T}{\Delta T_{\infty}} = e^{-\frac{t}{\tau_c}} \Rightarrow \tau_c = -\frac{t}{\ln\left(\frac{\Delta T}{\Delta T_{\infty}}\right)} \quad (5.3)$$

According to Fig. 5.14 and Fig. 5.15, the cooling time constants τ_{cR} , τ_{cS} are more than twice as high as the heating time constants τ_{hR} , τ_{hS} . This is not unusual, as the heat dissipation of the active components is reduced on natural convection at power-off state extending the cooling down process. The results correspond to the statements given in [HVB99].

The CFC IM shows an overload duration of 277s at $P_{max} = 10.5\text{kW}$. The VFC IM shows an additional overload duration of 8s. Hence, the CFC and the VFC IM tend to be very similar at the S2-operation. Indeed, this is quite obvious as the IM is designed to be highly saturated. Because of this, the machine flux ϕ can only be slightly increased at VFC. The maximum torque output T_{max} is predominantly provided by the torque building current $I_q \approx I_R$ which is quite similar to CFC. Thus, the rotor cage reaches the maximum temperature of 180°C almost at the same time.

The CFC PMSM shows an overload duration of 122s. As stated in Sec. 5.2.3, there can only be achieved low efficiency increases within the overload region for the VFC PMSM. The efficiency gains are very poor and can be given by 1% at 34Nm and 2910rpm. In fact, they do not lead to a significant extension of the overload duration, which results in 124s for the VFC PMSM.

Maximum overload duration	IM	PMSM
Constant flux control (CFC) [s]	277	122
Variable flux control (VFC) [s]	285	124

Table 5.4: Maximum overload duration of CFC and VFC for IM and PMSM.

5.4 Summary and Discussion

Design Method

In conclusion, Sec. 5.2 and Sec. 5.3 serve as an additional evaluation basis for the DMs presented in Sec. 4.2.3 and Sec. 4.2.4. The analysis and optimization of operation ranges and the implemented thermal model are part of the 3rd design stage acting as post-processing unit.

Referring to Fig. 4.13 and Fig. 4.22, there is no explicit feedback from step 8 to step 4 (IM) and step 4.1 (PMSM) which means that a non-thermally stable design specification will not automatically cause a change of the input variables shown in Tab. 4.2. The design specifications have to be adapted manually. Thus, in case of a too high overtemperature of stator or rotor winding

- lower the nominal copper density J_{cu}
- lower the nominal shear force density σ_n
- lower the number of pole pairs p
- increase the relative tooth width $\frac{w_t}{w_{sl}}$
- increase the stack length l_{fe}

for a given design torque T_n and supply frequency f_n . Overtemperatures of magnets must be checked by their individual $B-H$ curves. In case of a too high overtemperature, the magnet type need to be changed by means of adapting the values of remanence flux density B_r and coercive field strength H_c .

Although the present investigations concentrated on air-cooled sizing examples of IM and PMSM, the given DMs are valid for each kind of cooling conditions. Designing water cooling machines requires at least one basic thermal parameter set in order to decide on a thermal stable input specification. This eventually requires a redesign of an existing water-cooled machine for identifying their heat transfer coefficients.

Design Comparison

Sec. 5.2.2 to Sec. 5.2.3 investigate CFC and VFC methods of the designed IM and PMSM and present their resulting efficiencies. CFC is based on constant saturation levels at constant torque region. VFC adjusts the machine flux level ϕ focusing on minimum machine losses for a given torque output T .

Both machines show a significant efficiency increase at the introduced VFC method. The efficiency increase $\Delta\eta$ of the designed IM is inversely proportional to the torque output T and reaches up to 50% at very low part loads

($T < T_n$). In case of the PMSM, VFC leads to a better utilization of the available reluctance torque T_r . This results in lower losses for a given torque output T by means of a more convenient current distribution of I_d and I_q . The designed PMSM shows the highest efficiency increases $\Delta\eta$ at low speeds and low torque outputs, which can approximately be given by 3% to 3.5%.

As far as the temperatures are concerned, VFC tends to cause some additional thermal strain on the IM rotor as a possibly decreased flux ϕ needs to be compensated by a higher torque current $I_q \approx I_R$. Thus, CFC and VFC are very close to each other at S2-operation which becomes even obvious at the resulting overload durations t_{ol} .

Tab. 5.5 gives a short summary of the individual heating and cooling time constants for IM and PMSM at different control methods. Considering the stator windings, the heating time constant of the PMSM τ_{hS} is 31% lower mainly caused due to 7% lower relative loss $P_{rel} = 5.4 \frac{\text{kW}}{\text{m}^2}$. The strong thermal utilization of the PMSM requires an earlier power-off state, hence, the PMSM shows a 56% lower peak power duration compared to the IM.

Heating time constant	IM		PMSM	
Stator winding τ_{hS} [s]	934	100%	642	-31%
Rotor cage/magnet τ_{hR} [s]	1241		2315	
Cooling time constant, CFC	IM		PMSM	
Stator winding τ_{cS} [s]	-		1445	
Rotor cage/magnet τ_{cR} [s]	2840		-	
Overload duration t_{ol} [s]	277	100%	122	-56%
Cooling time constant, VFC	IM		PMSM	
Stator winding τ_{cS} [s]	-		1450	
Rotor cage/magnet τ_{cR} [s]	2881		-	
Overload duration t_{ol} [s]	285	100%	124	-56%

Table 5.5: Thermal time constants and overload durations of IM and PMSM.

In conclusion, from a purely operational point of view, the VFC IM provides significant advantages for the use within an automotive traction applications. Its part load efficiencies can be increased significantly, therefore, the IM comes very close to the PMSM within that region. Beside that, the IM provides high efficiencies within the field weakening region and has a two times higher overload duration compared to the PMSM at S2-operation. Fail-safe characteristics have not been considered so far. A compendium of these characteristics is given in Tab. A.2.

6

In-Wheel Motor Application

Chap. 6 concentrates on an in-wheel motor application of the sized IM and PMSM designed in Chap. 4. A hybrid power train is set up in the vehicle simulation program veDYNA® providing all necessary mechanical and electrical propulsion and supply components for the use of the motors at the rear axle of the vehicle [DYN11]. The operation of the individual motors is considered by their speed-controlled efficiency maps introduced in Chap. 5. Chap. 6 concentrates on the investigation of the energy consumption of IM and PMSM, representing fuel saving potentials by VFC methods. Moreover, the present chapter gives a tendency of suitability of IM and PMSM for different application scenarios.

6.1 Assumptions

The research focuses on a medium sized parallel hybrid power train topology, having an ICE in the front and two in-wheel motors at the rear axle of the vehicle. The following sections concentrate on the cycle efficiencies of the motor types and compare the results of IM and PMSM. The motors are designed to be integrated within a 16inch wheel rim. The assembly of motor and gear drive is coupled to the drive shaft via a clutch element. The determination of the electric motor cycle efficiencies and the corresponding fuel consumption of the vehicle will be given for the New European Driving Cycle (NEDC) consisting of a city cycle section (ECE15) and an urban cycle section (EUDC). In order to allow a valid comparison of the machines, the final state-of-charge (SOC) of the battery is restored to its initial condition at the end of the cycle. All auxiliary

consumers of the vehicle are assumed to be switched off.

6.2 Vehicle Dynamics Model

The simulation program veDYNA® integrates and implements the numerical simulation of a full vehicle model. Thereby, a full vehicle model combines driving and steering components which basically allows a vehicle to follow a spatial trajectory. The veDYNA model consists of a fully parameterized multi-body system including component models for power train, steering and tyre dynamics, see Fig. 6.1. The vehicle body has three translational and three rotational degrees of freedom. However, up to 30 degrees of freedom per axle are considered in case of geometrically modeled suspensions [EBSB07]. The simulation program allows to implement components at different levels of detail. Hence, the highly nonlinear elastokinematics of the individual axle types can be depicted by either look-up tables or by detailed geometric models including control arms, drag links and bushings.

The spatial motion of the vehicle is described by minimum coordinates \mathbf{y}_{VB} giving the vehicle body position in inertial coordinates as well as its roll, pitch and yaw angles. In addition, generalized velocities \mathbf{z}_{VB} are introduced giving the translational and angular speeds in the vehicle reference frame. The use of generalized velocities is very advantageous as the equations of motion become very compact. The individual bodies such as front or rear axle are specified by position \mathbf{y}_{FA} , \mathbf{y}_{RA} and velocity vectors \mathbf{z}_{FA} , \mathbf{z}_{RA} relative to the vehicle reference system [EBSB07]. The transformation between the inertial system and the vehicle reference frame is described by the subsequent kinematic equations

$$\begin{pmatrix} \dot{\mathbf{y}}_{VB} \\ \dot{\mathbf{y}}_{FA} \\ \dot{\mathbf{y}}_{RA} \end{pmatrix} = \begin{pmatrix} \mathbf{C}_{VB} & 0 & 0 \\ 0 & \mathbf{I} & 0 \\ 0 & 0 & \mathbf{I} \end{pmatrix} \begin{pmatrix} \mathbf{z}_{VB} \\ \mathbf{z}_{FA} \\ \mathbf{z}_{RA} \end{pmatrix}, \quad (6.1)$$

where \mathbf{I} and \mathbf{C}_{VB} denote the identity matrix and the transformation matrix between the time derivative of the position vector \mathbf{y}_{VB} and the vector of generalized speeds \mathbf{z}_{VB} respectively. Considering the Newton-Euler equations

$$\begin{aligned} m_i a_i &= F_i^c + F_i^a, \\ J_i \alpha + \omega \times J_i \omega &= T_i^c + T_i^a, \end{aligned}$$

with the translational and rotational accelerations a_i and α_i the dynamic equations read:

$$\underbrace{\begin{pmatrix} \mathbf{M}_{BB} & \mathbf{M}_{BF}^T & \mathbf{M}_{BR}^T \\ \mathbf{M}_{BF} & \mathbf{M}_{FF} & \mathbf{0} \\ \mathbf{M}_{BR} & \mathbf{0} & \mathbf{M}_{RR} \end{pmatrix}}_{\mathbf{M}_{vehicle}} = \underbrace{\begin{pmatrix} \dot{\mathbf{z}}_{VB} \\ \dot{\mathbf{z}}_{FA} \\ \dot{\mathbf{z}}_{RA} \end{pmatrix}}_{\dot{\mathbf{z}}_{vehicle}} \underbrace{\begin{pmatrix} \mathbf{Q}_{VB} \\ \mathbf{Q}_{FA} \\ \mathbf{Q}_{RA} \end{pmatrix}}_{\mathbf{Q}_{vehicle}} \quad (6.2)$$

The symmetrical mass matrix $\mathbf{M}_{vehicle}$ includes the contributions of the masses m_i and the moments of inertia J_i of the individual bodies referenced with the

index i . The vector $\mathbf{Q}_{vehicle}$ holds the constrained and applied forces (F_i^c , F_i^a) and torques (T_i^c , T_i^a) [HIR11]. The tyre force computation in veDYNA is based on the modeling approach of TMeasy. The model uses a semi-physical method which simplifies the analytical description of acting tyre forces and torques [EBSB07].

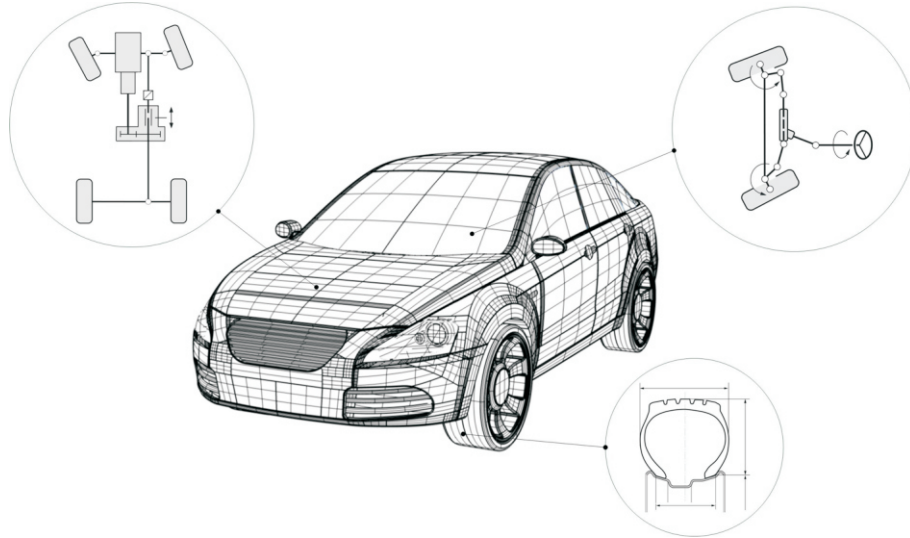


Figure 6.1: Full vehicle model of veDYNA including component models for power train, steering and tyre dynamics.

6.3 In-Wheel Motor System Specification

The electric motors are supposed to substitute a conventional all-wheel drive (AWD) concept on the rear axle of a passenger car. For packaging reasons, the motors are integrated into a 16inch wheel rim. The design study focuses on the use of a conventional brake system, thus, the maximum outer stator diameter d_{oS} is restricted to 170mm. The design specifications of the electric motors have been evaluated by an analysis of the torque distribution of a conventional AWD concept resulting in 400Nm at a maximum per wheel up to a vehicle speed of 30km/h. The motors are designed to provide additional torque up to a vehicle speed of 120km/h.

According to Sec. 4.2.2, high torque demands within restricted volumes used to cause high machine losses. Thus, there is a tradeoff between small motor dimensions on the one hand and high machine efficiencies on the other hand. Because of this, it is recommendable to integrate a gear box. Not only the design torque T_n is lowered which is the main sizing factor at electric machines but also

the thermal utilization of the machine is reduced. However, high gear ratios increases the maximum speed n_{max} which might be sensitive to the mechanical stability of the rotor.

In fact, the gear ratio cannot be selected independently. There are some guidance values on how to check whether n_{max} is within a valid range. Considering the design of IM and PMSM with surface mounted magnets, the circumferential speed v_c of the rotor should be chosen to be within [HUB11]:

$$70 \leq v_c \leq 120 \frac{\text{m}}{\text{s}} \quad (6.3)$$

Referring to Tab. 4.1, the outer rotor diameter d_{oR} should be selected to be within 100 – 110mm for an outer stator diameter of $d_{oS} = 170\text{mm}$ and $p = 2$. Considering the outer rotor diameter $d_{oR} = 103\text{mm}$, the maximum overspeed $n_{os} = 1.2 * n_{max}$ and Equ. (6.3), the gear ratio was selected to be 11.5 resulting in

$$v_c \approx 76 \frac{\text{m}}{\text{s}}. \quad (6.4)$$

Considering Equ. (6.3), it might be suggestive to choose a higher gear ratio. However, the given gear ratio of 11.5 is maximum in case of integrating gear box and electric motor within one housing facing an outer diameter of approximately 170mm.

The electric power train does not consider a step-up converter. Hence, the terminal voltage of the battery U_b corresponds to the intermediate circuit voltage U_i representing a load depending voltage level. The motors are therefore designed for a minimum voltage of 250V.

Design specification	Wheel	Electric Motor
Maximum power P_{max} [kW]	10.5	10.5
Maximum torque T_{max} [Nm]	400	35
Nominal torque T_n [Nm] ¹	200	17.5
Nominal speed n_n [rpm]	250	2875
Maximum speed n_{max} [rpm]	1030	11845
Maximum overspeed n_{os} [rpm]	-	14215
Minimum battery voltage U_b [V]	-	250

¹ Assuming an overload factor of two.

Table 6.1: System design specifications for the in-wheel motor configuration.

6.4 Power Train Architecture

The present section gives an overview of the hybrid power train architecture and the corresponding “on-demand” (OD) strategy of the power train components. Therefore, the front axle of the vehicle is propelled mechanically whereas the rear axle of the vehicle is driven electrically and works as additional torque supplier. The rear axle provides 800Nm up to a vehicle speed of 30km/h. Thus, electric driving is basically possible within city cycles. Both axles are electrically coupled via the battery system, figuratively shown by the dotted lines. Front and rear axle propulsion are mechanically coupled via the road only.

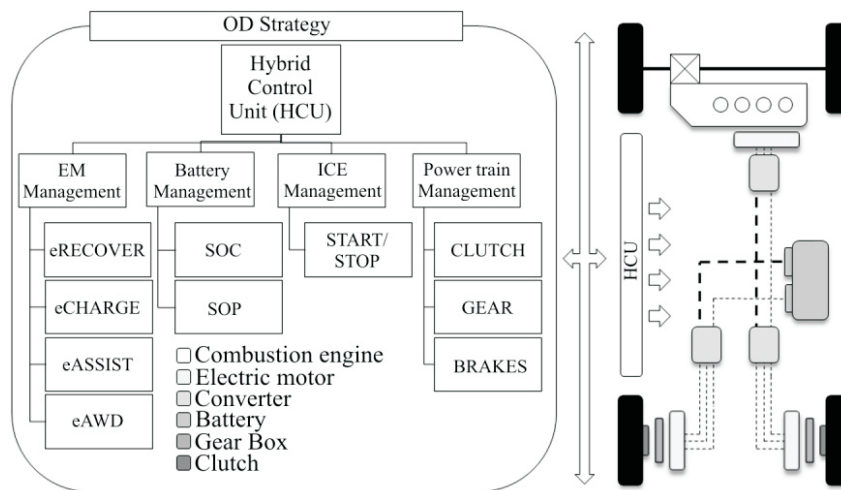


Figure 6.2: Power train architecture and “On-demand” strategy of the hybrid vehicle.

Fig. 6.2 illustrates the interfaces between the component management systems and the superior hybrid control unit (HCU). This unit manages the communication, the individual component states and the operation ranges of the power train components.

As far as the electric motor management system is concerned, there are four different modes. The operation modes are listed according to their priority. At any time there is only one mode put on active state by the HCU. The mode “eRECOVER” has the highest priority trying to recover electric power at braking. The mode “eASSIST” provides a torque boost function. The torque contributions at the rear axle are therefore higher the lower the dynamics of the load requirements from the driver. Thus, the present mode enables full electric driving at city cycles up to a vehicle speed of 30km/h. Having “eCHARGE” on active state means that the battery is on low state-of-charge ($SOC \leq 30\%$). In order to prevent unfavorable serial efficiency chains, the operation mode “eASSIST” is disabled until the SOC of the battery has reached a valid operation

range (SOC=70%). The operation mode “eAWD” has the lowest priority. The function is triggered by an increasing front tyre slip ($s_{ft} \geq 1.5\%$). The operation mode represents a basic functionality of the vehicle. Hence, it cannot be switched off by the “eCHARGE” strategy. The operation modes are depicted in Fig. 6.3.

The battery management system considers a second interface providing the maximum duration of the peak power, given by means of the state-of-power (SOP). As far as the power train management systems are concerned there is one interface for starting and shutting down the engine, one for adjusting clutch and gear position and one for activating the mechanical brakes. Switching off the ICE causes a minimum power-off state of 6s. Afterwards, the ICE can either be switched on due to insufficient torque settlements of the in-wheel motors, by underrunning a 30% SOC of the battery, or by exceeding a vehicle speed of 25km/h at the horizontal. The clutch is controlled to provide torque at the front axle depending on the operating state of the ICE. A summary of the vehicle data is given in Tab. 6.2.

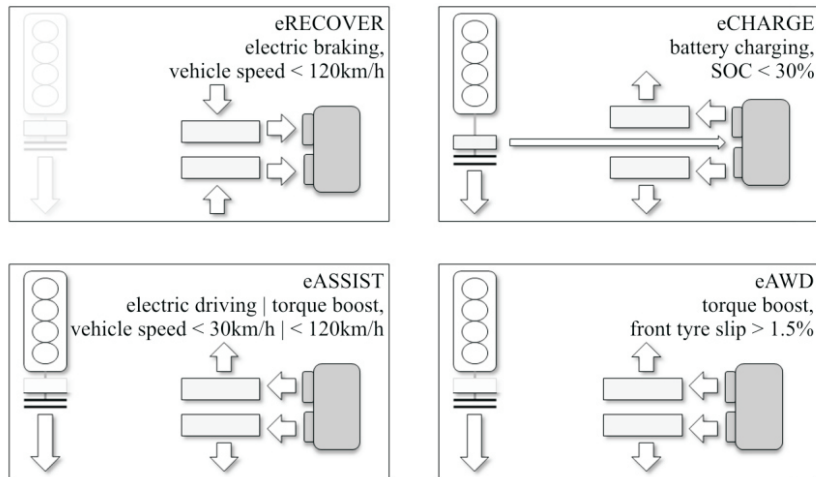


Figure 6.3: Electric motor operation modes; (white shaded) inactive components; (white) battery; (red) electric motor; (blue) internal combustion engine

Vehicle	Value
Vehicle mass m_v [kg]	1600
Drag value c_d [-]	0.32
Front area A_f [m ²]	2.2
Wheel rim d_r [inch]	16
Effective tyre radius r_e [m]	0.31

Table 6.2: Vehicle data of the parallel hybrid power train topology.

6.5 Power Train Components

The following content gives a short introduction of the external implemented power train components. The internal components of the vehicle dynamics program veDYNA® will not be commented as they are considered by their individual equations of motions which are solved internally, see Sec. 6.2. The moments of inertia of the additional mechanical components in the wheels are adapted as they are necessary for the computation of the equations of motions within veDYNA®.

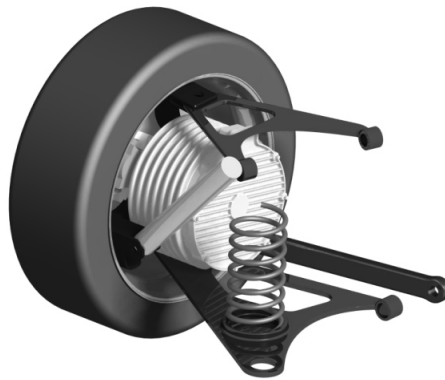


Figure 6.4: Motor package study at a double wishbone suspension with an adapted spring damper system [RNA11].

Internal Combustion Engine

The introduced hybrid power train architecture uses a four-cylinder compression ignition engine with a maximum power output of 77kW, see Tab. 6.3. The ICE is considered by a steady state performance map having a maximum efficiency of 41.7% at 222Nm and 2143rpm. The dynamics of the ICE are considered by a PT1 element.

Battery System

The battery is considered by a single cell approach considering a voltage source and a RC-circuit. Indeed, it is very convenient to concentrate on cell levels as the parameters are much easier to identify. The OD strategy of the hybrid power train architecture mainly causes a short-term operation of the electric machines which results in short but high power drains of the battery cells. Due to cell lifetime considerations, the time duration of the power drains is limited. The operation ranges are therefore specified by 40% of the standard capacity. In

order to satisfy the power requirements of the motor types, the battery uses 106 cells in series and two cells in parallel, each having a nominal capacity of 3600mAh. Thereby, the battery provides a nominal voltage of 350V.

Electric Motor and Converter

The electric motors as well as their converters have been modeled separately. The efficiencies of the electric machines are considered by their individual performance maps given in Sec. 5.2. The machine dynamics are specified by a PT1 element. The active component temperatures are based on the approach given in Sec. 5.3. The modeling of the corresponding converters is given by efficiency maps modeled according to the approach of [JAE95].

Gear Box

According to the statements given in Sec. 6.3, both motors use a dual-stage gear drive with a gear ratio of 11.5. The gear box is considered by a steady state performance map having a maximum efficiency of 96%. Its dynamics are considered by a PT1 element.

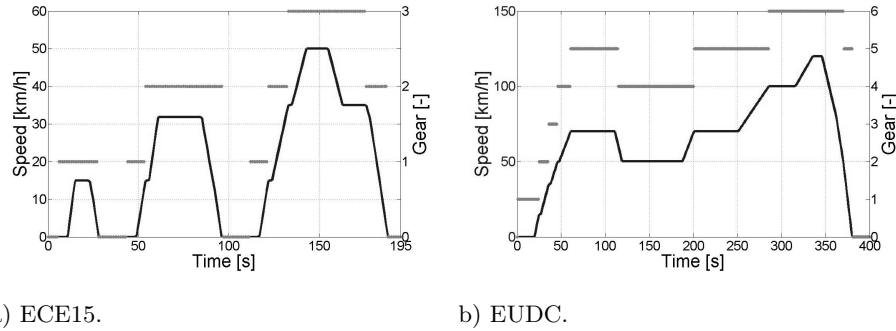
Tab. 6.3 gives an overview of the used power train components.

Components	Value
Maximum engine power P_{max} [kW]	77 at 4400rpm
Maximum engine torque T_{max} [Nm]	250 at 2500rpm
Rated starter engine power P_n [kW]	9.4
Rated in-wheel motor power P_n [kW]	2x5.25
Rated battery voltage U_i [kWh]	350
Rated battery energy E_n [kWh]	2.5, 40% usable
Maximum discharge current $I_{dc,max}$ [A]	296
Maximum charge current $I_{c,max}$ [A]	140

Table 6.3: Power train data of the parallel hybrid power train topology.

6.6 New European Driving Cycle

Driving cycles define vehicle speed as a function of the cycle duration. Therefore, gear shift information has to be taken into account in order to get comparable and reproducible results. The New European Driving Cycle (NEDC) is well known in automotive industry. At present, the NEDC represents the standard European test procedure for fuel consumption measurements. The NEDC has a total cycle time of 1180s and consists of four consecutive city cycle sections (ECE15) and a subsequent interurban part (EUDC). Both cycle sections are known to be modal cycles and can be characterized by piecewise constant speeds and constant accelerations. The maximum speed is 120km/h, the maximum acceleration is around 1m/s^2 . The subsequent investigations on fuel consumptions will be given for the ECE15 and the EUDC, figuratively shown by Fig. 6.5. Constant vehicle accelerations do not effectively represent real-world driving patterns. Therefore, the NEDC should be considered somehow critically.



a) ECE15.

b) EUDC.

Figure 6.5: City and urban cycle parts of the NEDC.

6.6.1 On-Demand Operation Strategy

The distribution of the driving torque between the front and the rear axle is managed by a causal relation of weighted vehicle speeds. The driver torque T_{tot} is entirely provided by the rear axle if the relative changes between the weighted moving average speeds $\text{WMA}(v_{t1})$ at time t_1 and $\text{WMA}(v_{t2})$ at time t_2 are zero. The distribution function d considers a memory of 1s. The corresponding axle torques T_{fa} and T_{ra} can be given by:

$$T_{fa} = d T_{tot} \quad (6.5)$$

$$T_{ra} = (1 - d) T_{tot} \quad (6.6)$$

$$d = \frac{|\text{WMA}(v_{t2}) - \text{WMA}(v_{t1})|}{\text{WMA}(v_{t1})}$$

Figure 6.6 illustrates the distribution function d for the rear axle torque T_{ra} and represents its normed values $T_{ra}/T_{ra,max}$ for the ECE15 and the EUDC. According to Fig. 6.6, the implemented hybrid power train strategy uses the cycle dynamics for the torque distribution. Constant speeds are predominantly provided by the rear axle. Transient cycle sections are provided by both axles representing an electrical AWD concept.

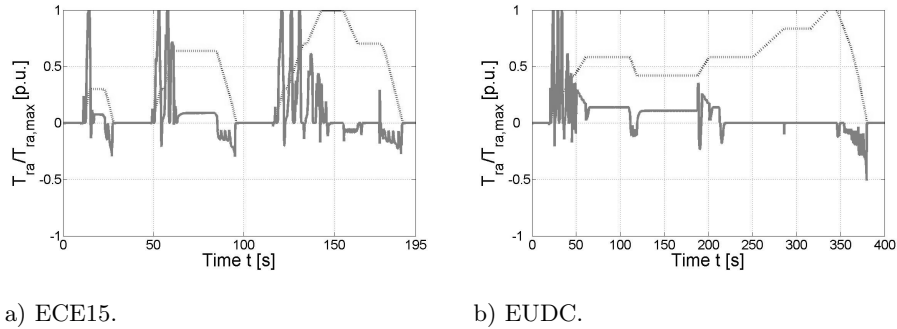


Figure 6.6: Normed rear axle torque during NEDC caused by the implemented hybrid power train strategy.

6.6.2 European City Cycle

Fig. 6.7 illustrates the motor operation distribution of the designed IM and PMSM used as OD torque supplier at the rear axle. The pull-out torque characteristics of the machines differ from each other, therefore, a common operation range is specified allowing valid motor operation points only.

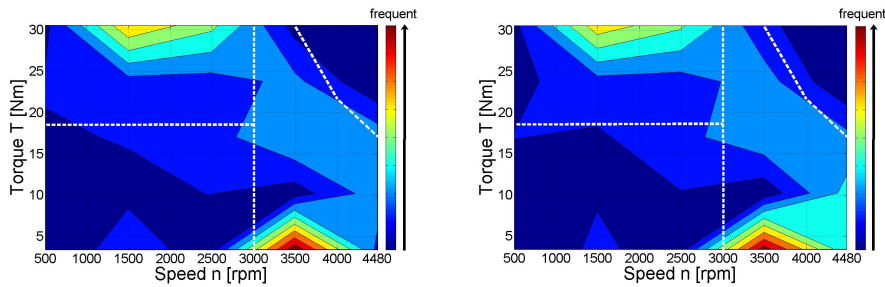


Figure 6.7: Motor operation distribution at the ECE15. The white dotted lines represent the individual operation ranges of the electric motors.

It is clearly shown, that the machines are predominantly operated within two different regions - the overload region ($T > T_n$) and constant power region

($n > n_n$). The city cycle accelerations are rather low and can be given around $1 \frac{m}{s^2}$. Nevertheless, the vehicle weight of 1600kg causes the electric motors to be operated at their maximum torque capability. This is also the case at constant power range. The highest vehicle speeds within the ECE15 are around 50km/h. The rated machine speed n_n corresponds to a translational velocity of 30km/h. Therefore, vehicle speeds higher than 30km/h naturally cause a higher operation frequency within this region.

ECE15, CFC Method	IM		PMSM	
Drive energy E_{drive} [$\frac{kWh}{100km}$]	10.4	100%	10.1	-3%
Energy recovery $E_{recover}$ [$\frac{kWh}{100km}$]	1.12	100%	1.44	+29%
Fuel consumption E_{fuel} [$\frac{l}{100km}$]	5.66	100%	5.56	-2%
Motor cycle efficiency η_{motor} [%]	80.8	100%	82.5	+1.7%
Vehicle cycle efficiency $\eta_{vehicle}$ [%]	26.2	100%	26.7	+0.4%

Table 6.4: Comparison of IM and PMSM operation characteristics at the ECE15 applying CFC method. The energy conversion is based on a diesel energy density of $9.83 \frac{kWh}{l}$ [STA08].

Tab. 6.4 shows a comparison between IM and PMSM at CFC. The IM works as a basis and is considered as 100%. The corresponding vehicle efficiencies are based on a required mechanical energy consumption of $14.57 \frac{kWh}{100km}$ at the ECE15. Tab. 6.4 also represents the basis for a subsequent comparison with VFC results.

The PMSM takes the lead requiring a 3% lower drive energy at the ECE15. The corresponding global fuel consumption of the vehicle is 2% lower compared to the IM. In fact, the relative fuel consumption savings of the different topologies are strongly depending on the shifted load ranges of the ICE. The hybrid vehicle provided with the CFC IM faces a 6% higher recharge time of the battery which is 436s in total. This represents an additional ICE load, which enhances the ICE efficiency on the one hand but even increases the fuel consumption on the other hand.

Considering all provided motor operation points, the PMSM shows a 1.7% higher cycle efficiency compared to the IM. Tab. 6.4 shows considerable energetic advantages for the PMSM which seem to be quite attractive for this kind of cycle. The CFC IM shows poor efficiencies, especially at part load operation ($T < T_n$). This statement becomes even more obvious when comparing the energy recovery potentials of the machines. The PMSM has a 29% higher energy recovery potential than the IM. In fact, the PMSM is still capable of recovering electric power at low part loads, see Fig. 6.8. Contrary to that, the CFC IM converts these low power into thermal energy heating up the active machine components only.

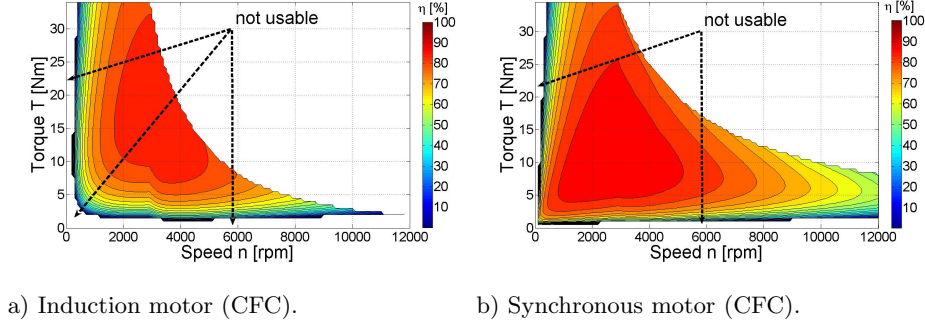


Figure 6.8: Generator efficiency map of IM and PMSM.

The advantages of the PMSM become much more smaller or even vanish when VFC is used. In fact, there is hardly any difference between the motor cycle efficiencies in case of the ECE15. Due to that, the vehicle fuel consumption is almost equal for both machines. The cycle efficiency of the IM can be increased by 2.5% which is more than twice the increase of the PMSM increasing from 82.5% to 83.7%. The cycle efficiency of the IM is very close to that of the PMSM which means that VFC may help to make IMs more favorable for city cycle applications. The energy recover potential with VFC is almost equal for both machines. Therefore, the disadvantages at low part load conditions vanish at the VFC IMs.

ECE15, VFC Method	IM		PMSM	
Drive energy E_{drive} [$\frac{\text{kWh}}{100\text{km}}$]	10.1	100%	10.1	0%
Energy recovery $E_{recover}$ [$\frac{\text{kWh}}{100\text{km}}$]	1.4	100%	1.43	+2%
Fuel consumption E_{fuel} [$\frac{1}{100\text{km}}$]	5.55	100%	5.56	+0.1%
Motor cycle efficiency η_{motor} [%]	83.3	100%	83.7	+0.4%
Vehicle cycle efficiency $\eta_{vehicle}$ [%]	26.7	100%	26.7	0%

Table 6.5: Comparison of IM and PMSM operation characteristics at the ECE15 applying VFC method. The energy conversion is based on a diesel energy density of $9.83 \frac{\text{kWh}}{\text{l}}$ [STA08].

6.6.3 European Urban Cycle

Fig. 6.9 shows the motor operation distribution within the European Urban Driving Cycle, EUDC. According to Sec. 6.6.2, a common operation range is specified. The given ranges provide operation points which can be met by both

machines. Unlike the ECE15, the operation points moved towards higher speeds. This is not surprising as the cycle speeds are higher having 120km/h at the maximum.

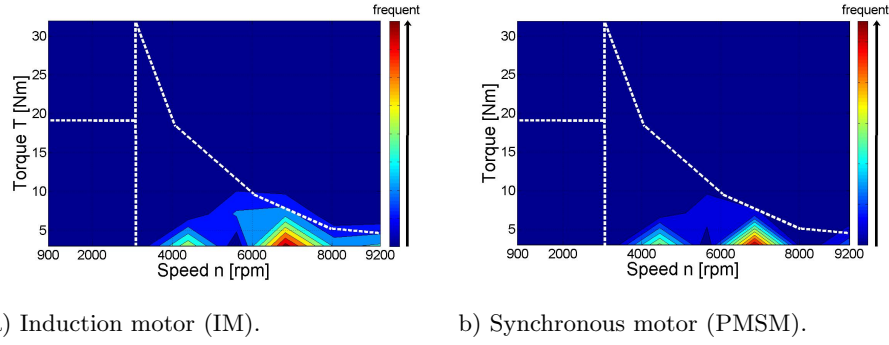


Figure 6.9: Motor operation distribution at the EUDC. The white dotted lines represent the individual operation ranges of the electric motors.

The histogram given in Fig. 6.9 does not show any operation within constant torque region. In fact, there are some operation points, although their frequency is pretty low and can be neglected compared to that of higher speed points. The most frequent operation points are between 4000rpm and 9000rpm. According to the rear axle torque distribution given by Equ. (6.6), these motor speeds correspond to the constant speed levels of the driving cycle being predominantly provided by the electric power train at the rear axle.

EUDC, CFC Method	IM		PMSM	
	Value	Efficiency	Value	Efficiency
Drive energy E_{drive} [$\frac{\text{kWh}}{100\text{km}}$]	5.2	100%	4.9	-6%
Energy recovery $E_{recover}$ [$\frac{\text{kWh}}{100\text{km}}$]	0.68	100%	0.62	-9%
Fuel consumption E_{fuel} [$\frac{1}{100\text{km}}$]	5.08	100%	5.17	+1.7%
Motor cycle efficiency η_{motor} [%]	82	100%	78.2	-3.8%
Vehicle cycle efficiency $\eta_{vehicle}$ [%]	29.8	100%	29.3	-0.5%

Table 6.6: Comparison of IM and PMSM operation characteristics at the EUDC applying CFC method. The energy conversion is based on a diesel energy density of $9.83 \frac{\text{kWh}}{\text{l}}$ [STA08].

Tab. 6.6 summarizes the energy consumption of the hybrid power train topologies for CFC machines. Thereby, the designed IM convinces at high speed applications with a motor cycle efficiency of 82%. Contrary to that, the disadvantages of the PMSM become more obvious at higher speeds. Due to the higher frequency at constant power region, the motor cycle efficiency of the PMSM goes

down to 78.2%. As a consequence the fuel consumption of the vehicle with the CFC PMSMs is 1.7% higher compared to that with the CFC IMs.

The different drive energies of the motors need to be considered by the introduced OD strategy. The PMSMs produce higher losses within the field weakening region resulting in an overall higher electric energy consumption. Consequently, the usable battery energy is depleted faster causing a higher power-off frequency of the motors. During that, the driver demand is predominantly provided by the ICE resulting in a higher overall fuel consumption at a lower electric energy consumption.

Having IMs mounted at the rear axle, the reverse is happening resulting in a higher electric energy consumption and a lower vehicle fuel consumption. The vehicle efficiency within the EUDC is based on a required overall mechanical energy consumption of $14.9 \frac{\text{kWh}}{100\text{km}}$. Both vehicle efficiencies can be increased by almost 3% compared to the corresponding city cycle section. The power train having IMs takes the lead having a vehicle cycle efficiency of 29.8%, closely followed by the PMSMs having 29.3%.

EUDC, VFC Method	IM		PMSM	
Drive energy $E_{drive} [\frac{\text{kWh}}{100\text{km}}]$	5.2	100%	4.9	-6%
Energy recovery $E_{recover} [\frac{\text{kWh}}{100\text{km}}]$	0.68	100%	0.62	-9%
Fuel consumption $E_{fuel} [\frac{\text{l}}{100\text{km}}]$	5.05	100%	5.16	+2%
Motor cycle efficiency $\eta_{motor} [\%]$	82	100%	78.2	-3.8%
Vehicle cycle efficiency $\eta_{vehicle} [\%]$	30	100%	29.4	-0.6%

Table 6.7: Comparison of IM and PMSM operation characteristics at the EUDC applying VFC method. The energy conversion is based on a diesel energy density of $9.83 \frac{\text{kWh}}{\text{l}}$ [STA08].

Tab. 6.7 shows the corresponding results for VFC machines. According to the statements given in Sec. 5.2.3, the influence of VFC is lower the higher the speed ranges of the cycle. Due to the flux reduction at constant power region, there is little scope left to adapt the machine flux ϕ , hence CFC and VFC become very close to each other. In fact, there is hardly any difference between the results given in Tab. 6.6 and Tab. 6.7.

6.7 Summary and Discussion

Sec. 6.6.2 and Sec. 6.6.3 analyze the cycle efficiency of a parallel hybrid power train having either IMs or PMSMs mounted at the rear axle. Therefore, the corresponding city (ECE15) and urban (EUDC) cycle sections of the NEDC have been investigated focusing on the energy consumption of the power train architecture by CFC and VFC methods.

Design Comparison

Considering the CFC machines, the PMSM shows clear advantages within the ECE15 having an almost 30% higher energy recover potential and a 1.7% higher motor cycle efficiency. This is not really surprising as synchronous machines are known to have excellent efficiencies around the base speed and under part load condition. However, the dominating characteristics of the PMSM become smaller by the use of VFC method. The results of the VFC IM are very close to that of the VFC PMSM in case of the ECE15. In fact, VFC methods predominantly help to reduce the poor energy recovery potential of CFC IMs. According to the statements given in Sec. 5.2.3, the influence of the VFC method on the motor efficiencies is low at constant power region. These statements are confirmed by the investigations of motor cycle efficiencies within the EUDC. The cycle causes the motors to be mostly operated at two to three times the base speed. Hence, the results obtained with VFC method are very close to those of CFC method.

High speed applications basically favor IMs. Therefore, the higher the speeds the higher the resulting IM motor cycle efficiency. Contrary to that, the reverse is happening in case of the PMSM having higher cycle efficiencies at lower cycle speeds. The reduction of the PMSM cycle efficiency gets obvious at the EUDC resulting in an overall cycle efficiency of approximately 78%. The IM has an almost 4% higher motor cycle efficiency compared to the PMSM.

It is clear that the given comparison between IM and PMSM strongly depends on the operation strategy of the axle torque distribution and the characteristic design points of the machines. Nevertheless, Tab. 6.4 to Tab. 6.7 gives a tendency of suitability on how to use the machines.

In conclusion, considering the predefined assumptions and application scenarios, the VFC IM takes the lead having convincing energetic characteristics within all operation ranges, especially at high speed applications. Therefore, it is highly recommendable to apply energy efficient control at IMs for the use in automotive traction applications. The PMSM convinces at city cycles having excellent efficiencies at constant torque region. As far as higher speeds are concerned, the PMSM suffers from increased losses reducing the overall motor cycle efficiency.

7

Summary and Conclusion

This doctoral thesis is divided into seven chapters which are summarized in the following.

Chapter 1 - Introduction: Mobility is considered to be a basic need of humanity. Therefore, automobiles always had, still have and will have a strong presence and importance for human beings. Considering the history of power train electrification, it has not been a history of continuous developments. Obviously, it has been accompanied by many ups and downs. The downs have largely been the same as today, costly batteries, small ranges, and time consuming recharging conditions. The ups have taken place due to environmental concerns meaning local and or global pollution, noise reduction and the call for sustainability of energy resources. Climate change and the finiteness of fossil energy resources nowadays are worldwide concerns. Automotive companies are therefore pushed to innovative solutions, mainly caused by political concerns, aiming at a gentle handling of energy sources. Shorter product innovation cycles cause cost and time urgencies which counteract product quality and consumer expectations.

At present, virtual design and dimensioning tools are of big interest as the early development process impacts subsequent production and modification costs. Virtual design tools allow a basic dimensioning of system components in conceptual design studies. Product optimization can already be done during early development stages which significantly reduces product varieties and subsequent product modification costs. Which machine topology to use for a specific automotive traction application and how to design and control them are essential questions. The present work deals with these issues and presents a time-efficient design

methodology (DM) for induction motors (IM) and permanent magnet synchronous motors (PMSM).

Chapter 2 - Hybrid Electric Power Train Topologies: Hybrid electric vehicles, HEVs, combine two energy sources and/or energy converter which can mainly be divided into series, parallel and power-split vehicle structures. The configurations differ by their individual propulsion energy flow which can either be serial, parallel or a mixed combination of both. The degree of suitability of a specific HEV heavily depends on the application scenario. Thus, series HEV are frequently used in commercial vehicles and buses, whereas parallel and power-split hybrids are predominately used in passenger cars. The subdivision of hybrids into micro, mild or full hybrids is well known. Nevertheless, it does not give any information concerning a technical or environmental evaluation of a vehicle. The hybridization ratio (HR) is defined as the relation between the continuous power outputs of the propulsion sources varying from almost zero (for conventional vehicles) up to infinity (for pure electric vehicles). The hybridization ratio (HR) allows an empirical estimation of fuel savings for given costs and can be used for a first estimation concerning the electric system component sizes.

Chapter 3 - AC Machine Topology Issues: The current work exclusively concentrates on two machine topologies - IMs and PMSMs having surface mounted magnets. At present, the given machines show the most promising characteristics concerning operation, assembling and costs for automotive traction drives. The individual suitability of a specific machine topology strongly depends on their operation ranges and therefore on the choice of the characteristic design values. Chap. 3 investigates IMs and PMSMs concerning their design, their operational characteristics and their fail-safe behavior. It gives background information on these issues and examines the corresponding choice of design parameters. Chap. 3 is aimed to ease the design considerations given in Chap. 4

Chapter 4 - AC Motor Design: Chap. 4 gives a detailed description of the introduced DM for a time-saving and reliable computation and evaluation of IMs and PMSMs with surface mounted magnets. The DM serves as an analytic design tool in conceptual design studies. Due to the time-saving approach, design parameters can easily be changed. Hence, the DM represents an evaluation basis illustrating the effects of the choice of characteristic design parameters on machine dimensions and efficiencies. The presented DM is exemplified by the sizing of a three-phase air-cooled IM and PMSM with an inner rotor configuration. The design concentrates on a high electromagnetic utilization providing a thermal acceptable continuous operation with a nominal power output of 5.25kW at a base speed of 3000rpm. The presented DMs for IMs and PMSMs are aimed to handle a minimum of necessary input specifications. The subsections of the chapter present the computation of the magnetic circuit and the iterative computation of the active component sizes. The sizing examples of IM and PMSM are compared to each other at the end of the chapter.

Chapter 5 - AC Motor Operation: Automotive applications normally require motors to be operated within wide speed ranges facing different loads. Thus, Chap. 5 presents the resulting efficiencies of the IM and PMSM design specifications introduced in Chap. 4. It gives an overview of their individual advantageous operation ranges and compares their operational characteristics at different control methods. Chap. 5 is supposed to serve as an additional evaluation basis on how to specify design specifications for a certain automotive traction application. Continuous and short-term operation of IM and PMSM are investigated evaluating the design specifications of IM and PMSM concerning the thermal utilization of active machine components. A corresponding comparison of the operational characteristics of IM and PMSM is given at the end of the chapter.

Chapter 6 - In Wheel Motor Application: In order to investigate IM and PMSM efficiencies in driving cycles, a parallel hybrid power train is set up in the simulation software veDYNA®. The software provides a full-vehicle model which has been enhanced by electric propulsion and supply components. The operation of the individual motors is considered by their steady-state performance maps introduced in Chap. 5. The electric motors are supposed to substitute a mechanical all-wheel drive (AWD) concept at the rear axle of a passenger car. The corresponding design values have been evaluated by an analysis of conventional AWD concepts. The evaluation of the electric motor cycle efficiencies and the corresponding fuel consumption of the vehicle is given for the New European Driving Cycle (NEDC) consisting of a city cycle section (ECE15) and an urban cycle section (EUDC). The chapter gives an overview of electric motor suitabilities for city and urban driving cycles by energy efficient control methods.

Chapter 7 - Conclusions: This thesis introduces a novel time-efficient DM for IMs and PMSMs with surface mounted magnets having a special focus on concept studies in an early development phases. The DM aims at a short computation time of the motor parameters which allows a fast evaluation of the machines concerning dimensions and operational characteristics. The DMs are exemplified by an air-cooled IM and an air-cooled PMSM having equal outer stator and rotor diameters. However, the presented DMs are valid for each kind of cooling conditions. The verification of the DM results and the design and operational comparison of IM and PMSM is given in Chap. 4 and Chap. 5. The corresponding comparison of the machines in an in-wheel motor application is presented in Chap. 6.

Indeed, it is a tough competition between the two machine topologies, as there are significant design advantages for the PMSM on the one hand and convincing operational advantages of the IM on the other hand. In conclusion, evaluating the research results under the given conditions and application scenario, the IM has slight advantages compared with the PMSM. The corresponding statements are given in Chap. 4 and Chap. 5.

The given sizing example of the IM has been assembled by THIEN eDrives GmbH. The theoretical research results of this work are currently investigated

further. The adaption of the motor control units - the converters - for an energy efficient control of the IMs is currently part of the research fields at the Electric Drives and Machines Institute in partnership with the Institute of Automotive Engineering in Graz, Austria.



a) Stator stack of the IM.



b) Rotor stack of the IM.

Figure 7.1: Iron stacks of the assembled IM.



Appendix A

A.1 Evaluation of Induction Motors and Permanent Magnet Synchronous Motors

The subsequent tables show a compendium and evaluation of the individual design and operational characteristics of the machines discussed in Chap. 3. The evaluation criteria and the given values in the subsequent tables result from a research work carried out by [WK09] in 2008.

Tab. A.1 represents an analysis of existing machines found in literature. The individual grading reflects the individual sequence according to the analyzed data. The IM is taken as basis and is denoted by 100%. Values which have not been accessible, mostly operational characteristics, have been added with attributes. The percentage values represent a reference as the real optimization criteria of the motor types were not known.

Tab. A.2 gives a short comment on the evaluation criteria trying to point out the essence of the operational characteristics of the investigated machines.

	IM		PMSM	
	Grading & Evaluation		Grading & Evaluation	
Active volume	2	100%	1	75%-95%
Active mass	2	100%	1	75%-90%
Stator loss	-	100%	-	-
Rotor loss	-	100%	-	-
Total loss	2	100%	1	70%-75%
Spinning loss	1	not existing	2	existing
Torque ripple	1	low	1	low / medium ¹
Noise emission	1	low	1	low / medium ¹
Overload capability	1	very good	1	very good
Wide speed capability	1	very good	2	medium ¹
Rotor position detection	1	not necessary	2	necessary
Fail safe behavior	1	very good	2	bad
Costs	1	low	1	low
Assembly	1	established	1	established
Average grading	1.25		1.33	

¹ Depending on control mechanism (BLAC vs. BLDC).

Table A.1: Overview of different design and operational characteristics of IMs, and PMSMs [WK09].

Criteria	IM		PMSM	
	Evaluation & Comment		Evaluation & Comment	
Active volume, active mass, torque density	o	Torque densities vary according to design criteria and cooling limitations (weight vs. efficiency); higher torque densities are related to higher motor losses	++	Torque densities vary according to design criteria and cooling limitations (weight vs. efficiency); high pole numbers cause low yoke heights but high motor losses
Total loss, efficiency	+	Copper and iron losses in stator and rotor; iron losses in rotor are small	++	Copper and iron losses in stator; iron losses in rotor are very small
Spinning loss	++	No separate excitation of the rotor; no decouple mechanism necessary	-	Permanent excitation of the rotor due to magnets; decouple mechanism recommendable
Overload capability	++	Very robust; high rotor temperatures acceptable	+	Excessive machine warming can lead to irreversible rotor demagnetization
Wide speed capability	++	Efficiency increase at field weakening range due to decrease of field building current	+	Efficiency decrease at field weakening range due to increase of field weakening current
Fail safe behavior	++	Safe state at no-load and short circuit	-	Short circuit: alternating torques; no-load: brake torques
Costs	++	Low cost assembling	+	Low cost assembling, sharp price increase for lanthanide magnets
++ very good, + good, o sufficient, - bad				

Table A.2: Overview of different design and operational characteristics of IMs and PMSMs [WK09].

B

Appendix B

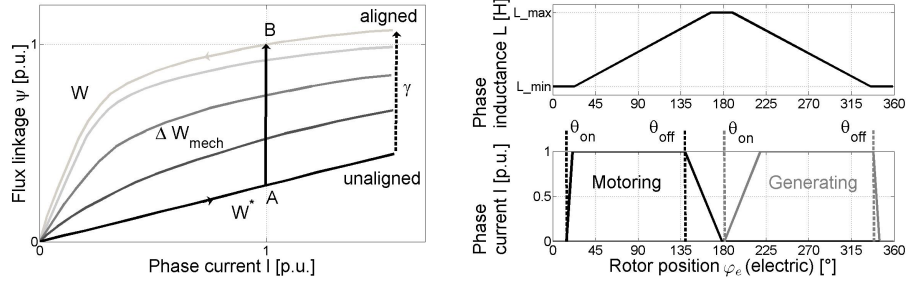
B.1 Switched Reluctance Motors

Switched reluctance motors (SRM) are generally known because of their simple and robust design. They convince by their relatively high speed ranges, their simple control and a hazard-free operation. The production costs of SRMs are expected to be lower compared to other motor technologies having less material and less energy consumption at their manufacturing processes. These advantages seem to be convincing for automotive traction applications.

B.1.1 Sizing

SRMs have a simple structure as the rotor consists of an iron core with distinctive poles whereas the stator has a multi-phased excitation winding with concentrated coils [RIE06].

According to Equ. (3.10), inductance differences can significantly contribute reluctance torque T_r without using any flux linkage ψ_a . Switched reluctance machines practice this principle as they use the magnetic unbalance of salient rotors for their torque output T . Considering a salient rotor pole configuration, the poles align themselves into a position such that the magnetic field lines are parallel orientated. When the stator pole is aligned to the rotor pole, the phase inductance is on a maximum since the magnetic resistance is minimal. Hence, an unaligned position of stator and rotor pole results in a minimal inductance.



a) The ψ - I -characteristic of a single SRM phase [SCH09].
 b) Ideal inductance and phase current characteristic of a SRM [YF09].

Figure B.1: Flux linkage, phase inductance and phase current as a function of the rotor tooth position of a single SRM phase.

Basically, the higher the inductance ratio between aligned and unaligned position, the higher the torque and power capability. Normally, the rotor pole arc is slightly wider than that of the stator pole. Therefore, SRMs have relatively few feasible stator/rotor pole number combinations ($\frac{6}{4}$, $\frac{8}{6}$, and integer multiples thereof being the most common) [ZH07].

The electromagnetic torque output T produced by the SRM is mainly based on the relative change of the magnetic co-energy W^* with the rotor position φ_m . Differently expressed, the torque output T can be given by the variation of the phase inductance L depending on the rotor position φ_m . It can be expressed by

$$T = \frac{\partial W^*}{\partial \varphi_m} = \frac{1}{2} I^2 \frac{\partial L}{\partial \varphi_m}, \quad (\text{B.1})$$

$$W^* = \psi i - W, \quad (\text{B.2})$$

where W and i denotes the magnetic energy and the phase current respectively [BAAL97]. The torque output is a quadratic function of the phase current I , and therefore independent of the current direction. In fact, this means that positive and negative torque outputs can be achieved with the same phase current polarity which represents a significant advantage of the SRM technology.

Basically, there are three parameters to control the torque output of the SRM, phase current I , turn-on θ_{on} and turn-off angle θ_{off} . The direction of the torque T is strongly related to the slope of the induction C_i which is a function of the rotor position φ_m [YF09]. Equ. B.1 shows that a positive gradient of the inductance likewise results in a positive torque output, whereas a negative gradient produces a negative one.

SRMs are normally designed to operate with high saturation, since the increase of the magnetic co-energy W^* corresponds to the mechanical energy output. The machine behavior and the relationship between the control parameters is highly nonlinear which results in a complex relation between the phase current

I and the torque output T . In fact, the characteristic of the phase current is strongly related to the circuit time which is again depending on the rotor position φ_m . An accurate control therefore has to precalculate the entire operational characteristics, which is given by flux linkage ψ and phase current I . These parameters cannot be adjusted independently from each other, hence, the $\psi - i$ characteristic conveys the finger print of each SRM. For this reason, iron losses have to be taken into account for an accurate torque calculation.

The maximum change of the co-energy ΔW_{mech} can be achieved if the phase current is switched on at q-position (unaligned) and switched off at d-position (aligned). Considering Fig. B.1, it is beneficial to switch on the phase current at position A (unaligned) almost representing a linear relationship to the flux linkage. The phase current should be kept constant for operating the SRM at higher saturation. Position B represents an aligned position and denotes the position where the phase current should be switched off. The inductance range determines the maximum torque capability. Thus, the difference between the aligned inductance L_d and the unaligned inductance L_q should be as high as possible. The equation reads

$$\frac{\partial L}{\partial \varphi_m} \approx \frac{Q_R}{C_i \pi} (L_d - L_q), \quad (\text{B.3})$$

where Q_R denotes the number of rotor poles, and C_i is a constant for the linear slope of the inductance. Because L_q is much smaller than L_d ($L_q \ll L_d$), the phase current increase is very fast, however, its decrease is very slow. In fact, the current flows only during half of the period, it is off during the second one, see Fig. B.1 [SCH07].

The number of rotor poles Q_R has a significant influence on the overload capacity. Basically, the higher the pole number, the lower the overload capability since the inductance difference decreases [ZH07]. High overload capabilities generally require SRMs to be operated with lower saturation as the inductance slope is higher. Therefore, stator and rotor iron cores have to be thicker in order to lower the flux densities. The peak torque capability is depending on:

- the rate of rise of the current after a phase winding has been commutated,
- the degree of saturation of the magnetic circuit,
- the allowable maximum current of the converter and
- the maximum allowable temperature rise.

The main losses of a SRMs are copper and iron losses. The stator has both of them since one tooth is spanned by one coil, representing a concentrated winding topology. The rotor does not have any magnets or coils, however, there are iron losses which have to be handled for a precise operation. The coil endings of the stator can be designed very shortly, besides, the copper fill factor is generally higher than those of other machines. This results in lower copper losses

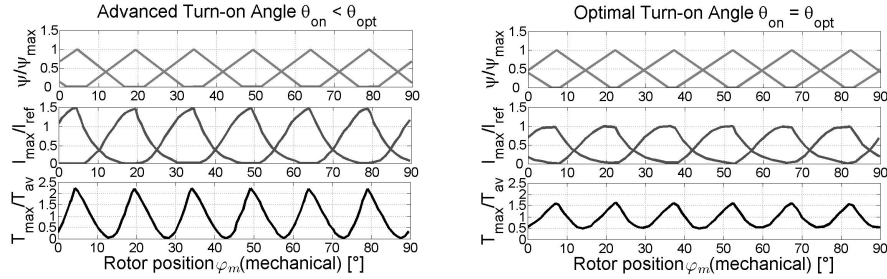
which cause a higher efficiency and a higher torque density for a given phase current [SCH07]. The iron losses are proportional to the magnetic excitation and the supply frequency f_n . Since flux waveforms are non-sinusoidal and flux harmonic spectra differ in various parts of the magnetic circuit, iron losses are not uniformly distributed in the core. Due to the high saturation level, the iron losses and the magnetic excitation are high. High MMFs require high magnetization currents which considerably lower the power factor $\cos(\varphi)$. The excitation of a SRM is a sequence of current pulses applied to each phase. A speed-control is done by regulating these currents according to a specific torque demand.

At constant torque region the available DC-link voltage of the energy source exceeds the back-EMF of the SRM, hence, the phase currents are controlled by PWM. When the machine is motoring, the peak current is solely determined by the turn-on angle, while when generating, both, turn-on and turn-off angle influence the peak current [ZH07]. As the back-EMF increases with higher speeds, the voltage may be insufficient for PWM. Consequently, entering constant power region means advancing the commutation angles for controlling the torque output. Generally, the higher the speed, the higher the commutation angle advance. At very high rotational speeds, the commutation advance is limited due to the influence of the back-EMF and winding inductance since the phase current waveform becomes continuous.

The number of rotor poles even influences the constant power range. Therefore, the higher the rotor pole number, the lower the constant power range. In summary, not only the overload capability is reduced at higher pole numbers, but also the constant power range is limited due to restricted commutation advances.

B.1.2 Operation, Control and Acoustic Noise

An optimal performance of a SRM can be achieved by a correct balance between the contributions of each phase to the total flux ϕ and the current I . An optimal turn-on angle θ_{opt} at a PWM control mode is therefore determined in a way that the phase current reaches its reference value I_{ref} at an unaligned position when rotor and stator pole are just starting to overlap. If the turn-on angle θ_{on} delays from the optimal value, the current increases on its reference value when entering a rising inductance slope region. In fact, this may have serious impacts on the torque output as the control value I_{ref} will not be reached at high motor speeds due to a large back-EMF [GRE00]. Contrarily, if the turn-on angle is advanced beyond the optimal value, the conducting period is expanded to an unaligned position. Current feeding at unaligned positions does not contribute any torque, since the flux linkage ψ is low and the inductance slope C_i is still flat. Copper losses increase which cause a higher idle power and a lower the power factor $\cos(\varphi)$. Shifting the turn-on angle towards the optimal angle will certainly lower the copper losses, nonetheless, the peak flux linkage may increase which will increase the iron losses. Considering the above mentioned statements, it can be concluded that there exists an optimal turn-on angle that represents a best



a) Advanced turn-on angles.

b) Optimal turn-on angles.

Figure B.2: Comparison of different turn-on angles as a function of the rotor position [KM05].

balance between copper and iron losses and therefore raises the efficiency for the provided torque output. The turn-off angle θ_{off} is specified in a way that the flux-linkages of two neighboring phases are equal to half of flux-linkage peak value on their intersection angle [KM05].

Fig. B.2 shows the effects of optimal control by properly adjusted turn-on angles at constant torque region. Not only the efficiency is increased because of minimum copper and iron losses, but also the torque ripple is lower. In [KM05], the deviation to the average torque was given by approximately 50% at optimal control. However, an advanced turn-on instant lead to an inevitably rise of the torque ripple. Torque pulsations, vibration and acoustic noise emission can be seen as the most hindering characteristics for the use of SRMs. Basically, vibrations are caused by mechanical deformations which arise by magnetic forces between the stator and rotor. The vibrations become much more serious when the radial deformation frequency of the stator is nearly equal to the natural frequency [ZWZ⁺09]. One way to smooth the torque output and to lower the pulsations are adjusted phase current waveforms combined with well balanced turn-on and turn-off angles. Hence, the estimation of the instantaneous torque, an accurate determination of the rotor position and the knowledge of the flux linkage represent key enabling factors for an effective control of SRMs. Generally speaking, the higher the speed and the higher the load, the higher the acoustic noise. The vibrations can be lowered by making the stator yoke bigger since the mechanical stiffness increases. Thereby, the overload capability can be improved, as the stator yoke becomes less saturated. Voltage-controlled SRMs usually generate lower acoustic noise than current controlled ones, since the random switching of the current controller results in a wide-band harmonic spectra. Moreover, reducing the supply voltage at light loads may even reduce the acoustic noise [ZH07]. Furthermore, there exist two alternative methods counteracting the emission of acoustic noise. The use of conduction overlap between two phases reduces torque pulsation since the currents of two neighboring phases are not switched on and off at the same time. The creation of an overlap,

once properly tuned, contributes to higher torque productivity and increases the torque density. Bipolar multi-phase excitation enables a short flux path between two neighboring phases. This lowers iron losses, torque pulsations and therefore vibrations [EKF05].

B.1.3 Fault Tolerance

In many cases, it is possible to consider each phase of a SRM operating in isolation. SRMs are characterized by multi-phase windings of which each is spanned over one tooth, representing a concentrated winding topology. The winding modularity of SRMs assures that coils have minimal influence on each other. A winding fault is therefore just the loss of one phase which means the other phases may continue to operate unaffectedly due to minimal electrical, magnetic and thermal interactions. Basically, the higher the number of phases, the higher the fault tolerance of the motor drives and the lower the effects during a faulted machine state. Each phase uses separate half bridges representing an electrical decouple mechanism. Besides, the mutual magnetic coupling between the phases is low.

Because the SRM is single-excited, there is a reduced likelihood of a phase-phase fault because the end windings do not overlap. However, two neighboring phases occupy the same slot, which might arise temperature problems due to limited thermal isolation between the phases [MJHC96]. In case of a phase fault, meaning a missing current contribution for the torque output, there will arise a dead zone along the inner stator length. Hence, the machine's inertia will be responsible for passing this zone. The commutation control signals of the damaged phase are blocked from now on in order to grant a continuous operation of the SRM.

Bibliography

- [AA05] C. D. ANDERSON and J. ANDERSON. *Electric and Hybrid Cars*. Mc Farland & Company, Inc., Jefferson, NC, 2005.
- [ANS11] ANSOFT. ANSYS Maxwell - Electromagnetic Field Simulation for High-Performance Electromechanical Design. Available at <http://www.ansoft.com/products/em/maxwell/>, 2011. Accessed on 15/09 2011.
- [AT09] M. T. ABOLHASSANI and H. A. TOLYAT. Fault Tolerant Permanent Magnet Motor Drives for Electric Vehicles. 1:1146–1152, 3rd May to 6th May 2009. Miami, FL.
- [BAAL97] T. T. BORGES, D. A. DE ANDRADE, H. R. DE AZEVEDO, and M. LUCIANO. Switched Reluctance Motor Drive at High Speeds, with Control of Current. *Electric Machines and Drives Conference Record*, 1:TB1/12.1–TB1/12.3, May 1997. Milwaukee, WI.
- [BBH09] D. BÜCHERL, I. BOLVASHENKOV, and H. G. HERZOG. Verification of the Optimum Hybridization Factor as Design Parameter of Hybrid Electric Vehicles. *Vehicle Power and Propulsion Conference (VPPC)*, 1:847–851, 2009. Dearborn, MI.
- [BHE06] I. BOLVASHENKOV, H. G. HERZOG, and A. ENGSTLE. Factor of Hybridization as a Design Parameter for Hybrid Vehicles. *International Symposium on Power Electronics, Electrical Drives, Automation and Motion (SPEEDAM)*, 1:926–929, July 2006. Taormina.
- [BIK99] U. BIKLE. *Die Auslegung lagerloser Induktionsmaschinen*. PhD thesis, Swiss Federal Institute of Technology Zurich, Zurich, Switzerland, 1999.
- [BOE07] W. BOEGE. *Vieweg-Handbuch Elektrotechnik: Grundlagen und Anwendungen für Elektrotechniker*. Friedr. Vieweg & Sohn Verlag / GWV Fachverlage GmbH, Wiesbaden, 2007.
- [BOS07] R. BOSCH. *Autoelektrik / Autoelektronik*. Friedr. Vieweg & Sohn Verlag / GWV Fachverlage GmbH, Wiesbaden, 5th edition, 2007.

- [BOU07] S. BOUVIER. Charakterisierung Permanentmagneterregter Synchronmaschinen für den Einsatz in Elektrischen Achsen. Master's thesis, Graz University of Technology, Graz, Austria, 2007.
- [CAR08] F. CARDARELLI. *Materials Handbook*. Springer-Verlag, London, 2nd edition, 2008.
- [CMS⁺10] D. CASADEI, M. MENGONI, G. SERRA, A. TANI, L. ZARRI, and M.F. CABANAS. Energy-Efficient Control Of Induction Motors For Automotive Applications. *International Conference on Electrical Machines (ICEM)*, pages 1–6, September 2010. Department of Electric Engineering, University of Bologna, Italy.
- [CWBR04] W. CANDERS, H. WÖHL-BRUHN, and B. RIUS-SAMBEAT. Charakterisierung und gezielter Entwurf von Elektromotoren für Fahrzeugantriebe. 2. *Braunschweiger Symposium - Hybridfahrzeuge und Energiemanagement*, 2:211, 2004. Braunschweig, Germany.
- [D'A93] S. D'AGOSTINO. The Electric Car. *IEEE Potentials*, 12(1):28–32, February 1993. Department of Electrical Engineering, Cornell University, Ithaca, NY.
- [DYN11] TESIS DYNAware. veDYNA. Available at <http://www.thesis-dynaware.com>, 2011. Accessed on 26/09 2011.
- [EBSB07] B. ESTERL, T. BUTZ, B. SIMEON, and B. BURGERMEISTER. Real-Time Capable Vehicle-Trailer Coupling by Algorithms For Differential-Algebraic Equations. *Vehicle System Dynamics*, 45:819–834, 2007.
- [EKF05] C. S. EDRINGTON, M. KRISHNAMURTHY, and B. FAHIMI. Bipolar Switched Reluctance Machines: A Novel Solution for Automotive Applications. *IEEE Transactions on Vehicular Technology*, 54(3):795–808, 2005. Department of Electrical Engineering, Arkansas State University, Jonesboro, AK.
- [EMB08] U.S. EMBASSY. U.S. Diplomatic Mission to Germany - About the USA. Available at <http://usa.usembassy.de/>, 2008. Accessed on 06/2011.
- [ERT97] M. EHSANI, K. M. RAHMAN, and H. A. TOLYAT. Propulsion System Design of Electric and Hybrid Vehicles. *IEEE Transactions on Industrial Electronics*, 44(1):19–27, 1997. Department of Electrical Engineering, Texas A&M University, College Station, TX.
- [FB07] D.G. FINK and H. WAYNE BEATY. *Standard Handbook of Electrical Engineering*. McGraw-Hill, New York, 15th edition, 2007.
- [FIS06] R. FISCHER. *Elektrische Maschinen*. Carl Hanser Verlag, Munich, 2006.

- [GBS⁺04] C. GERADA, K. J. BRADLEY, M. SUMNER, P. WHEELER, S. PICKERING, J. CLARE, C. WHITLEY, and G. TOWERS. The Implications of Winding Faults in Induction Motor Drives. *Industry Application Conference*, 4:2506–2513, October 2004. School of Electric & Electronic Engineering, Nottingham University, UK.
- [GHV03] H.-U. GIERSCH, H. HARTHUS, and N. VOGELSANG. *Elektrische Maschine - Prüfen, Normung, Leistungselektronik*. Teubner / GWV Fachverlag GmbH, Wiesbaden, 5th edition, May 2003.
- [GRE00] A. GREIF. *Untersuchungen an Geschalteten Reluktanzantrieben für Elektrofahrzeuge*. PhD thesis, Munich University of Federal Armed Forces, Munich, Germany, 2000.
- [HAN94] D. HANSELMAN. *Brushless Permanent Magnet Motor Design*, chapter 4, pages 67–93. Orono, Maine, 2nd edition, 1994.
- [HIR10] M. HIRZ. *Advanced Computer Aided Design in Conceptual Automotive Development*. Graz, Austria, 2010.
- [HIR11] W. HIRSCHBERG. Fahrzeugdynamik. *Lecture notes*, page 105, 2011. Graz, Austria.
- [HØY08] K. G. HØYER. The History of Alternative Fuels in Transportation: The Case of Electric and Hybrid Cars. *Utilities Policy*, 16(2):63–71, 2008. Oslo University College, Oslo, Norway.
- [HUB11] A. HUBER. THIEN eDrives GmbH: Experimental Data Concerning Sizing and Operation of Induction Motors and Permanent Magnet Synchronous Motors. Lustenau, Austria, 2011.
- [HVB99] E. HERING, A. VOGT, and K. BRESSLER. *Handbuch der elektrischen Anlagen und Maschinen*. Springer Verlag, 1999. Munich.
- [ISDK08] R. INGRUBER, R. SEEBACHER, G. DANNERER, and K. KRISCHAN. Wirkungsgradoptimaler Betrieb von Asynchronmotoren bei variabler Drehzahl. 10. *Symposium Energieinnovation*, 1:234–235, 13th February to 15th February 2008. Graz, Austria.
- [IZH05] D. ISHAK, Z. Q. ZHU, and D. HOWE. Eddy Current Loss in the Rotor Magnets of Permanent-Magnet Brushless Machines Having a Fractional Number of Slots Per Pole. *IEEE Transactions on Magnetics*, 41(9):2462–2469, September 2005. Department of Electronic & Electric Engineering, University of Sheffield, UK.
- [JAE95] B. JAECKLE. *Antriebstechnik im Maschinenbau*, volume 5, pages 29–40. Bundesamt für Konjunkturfragen, Bern, 1995.
- [JB02] C. M. JEFFERSON and R. H. BARNARD. Hybrid Vehicle Propulsion. *Advances in Transport*, 10:150, 2002. University of the West of England, UK, University of Hertfordshire, UK.

- [JMA11] JMAG. JMAG - Designer. Available at http://jmag-international.com/products/studio_designer/, 2011. Accessed on 15/09 2011.
- [JMH96] A. G. JACK, B. C. MECROW, and J. A. HAYLOCK. A Comparative Study of Permanent Magnet and Switched Reluctance Motors for High-Performance Fault-Tolerant Applications. *IEEE Transactions on Industry Applications*, 32(4):889–895, August 1996. Department of Electric & Electronic Engineering, Newcastle Tyne University.
- [KM05] I. KIOSKERIDIS and C. MADEMLIS. Maximum Efficiency in Single-Pulse Controlled Switched Reluctance Motor Drives. *IEEE Transactions on Energy Conversion*, 20(4):809–817, December 2005. Department of Electronics, Technological Educational Institute of Thessaloniki, Greece.
- [LE04] S. M. LUKIC and A. EMADI. Effects of Drivetrain Hybridization on Fuel Economy and Dynamic Performance of Parallel Hybrid Electric Vehicles. *IEEE Transactions on Vehicular Technology*, 53(2):385–389, March 2004. Electrical & Computational Engineering Department, Illinois Institute of Technology, Chicago, IL.
- [LEV08] E. LEVI. Multiphase Electric Machines for Variable-Speed Applications. *IEEE Transactions on Industrial Electronics*, 55:1893 – 1909, May 2008. Liverpool John Moores University, Liverpool.
- [LFL93] T. LIU, J. FU, and T. A. LIPO. A Strategy for Improving Reliability of Field-Oriented Controlled Induction Motor Drives. *IEEE Transactions on Industry Applications*, 29(5):910–918, October 1993. Department of Electrical Engineering, Taiwan Institute of Technology, Taipei.
- [LS04] F. LIBERT and J. SOULARD. Design Study of Different Direct-Driven Permanent-Magnet Motors for a Low Speed Application. *Nordic Workshop on Power and Industrial Electronics*, June 2004. Trondheim, Norway.
- [LYJ08] J. LI, XU Y., and ZOU J. A Study On The Reduction Of Vibration And Acoustic Noise For Brushless DC Motor. *International Conference on Electrical Machines and Systems (ICEMS)*, pages 561 – 563, October 2008. Department of Electric Engineering, Harbin Institute of Technology, Harbin.
- [MAG11] CHEN YANG MAGNETICS. NdFeB Magnete - Neodym Eisen Bor Magnete. Available at <http://www.cy-magnetics.com>, 2011. Accessed on 05/03 2011.

- [MAN89] M. MANOWARDA. Elektrische Maschinen I. *Lecture notes*, 1989. Graz, Austria.
- [MAT11] MATHWORKS. MATLAB. Available at <http://www.mathworks.com>, 2011. Accessed on 26/09 2011.
- [MJHC96] B. C. MECROW, A. G. JACK, J. A. HAYLOCK, and J. COLES. Fault-Tolerant Permanent Magnet Machine Drives. *IEE Proceedings - Electric Power Applications*, 143(6):437–442, November 1996. Newcastle upon Tyne University, UK.
- [MUE94] G. MUELLER. *Grundlagen elektrischer Maschinen*. Wiley-VCH Verlag GmbH & Co KG, Weinheim, 1994.
- [MUL10] M. MULVEY. Daily Exhaust From the Combustion Chamber. Available at <http://http://dailyexhaust.com/2010/07/electric-cars-have-been-around-a-long-time.html>, 2010. Accessed on 10/01 2010.
- [MVP08] G. MUELLER, K. VOGT, and B. PONICK. *Berechnung elektrischer Maschinen*. Wiley-VCH Verlag GmbH & Co KG, Weinheim, 2008.
- [NER06] W. NERRETER. *Grundlagen der Elektrotechnik*. Carl Hanser Verlag, Munich, Germany, 2006.
- [NL96] D. W. NOVOTNY and T. A. LIPO. *Vector Control and Dynamics of AC Drives*. Oxford University Press, New York, 1996.
- [NP06] M. NOLL and F. PIRKER. Smart Drives for Smart Cars. *E & I Elektrotechnik und Informationstechnik*, Springer Verlag, 123(10):432–436, 2006. Munich.
- [OVE04a] OVE. Rotating Electrical Machines - Part1: Rating and Performance, Österreichischer Verband für Elektrotechnik, Österreichisches Normungsinstitut, 2004.
- [OVE04b] OVE. Rotating Electrical Machines - Part2: Losses and Efficiency, Österreichischer Verband für Elektrotechnik, Österreichisches Normungsinstitut, 2004.
- [PEI03] M. PEIPPONEN. Drehmomentregelung in einem Lenkungsantrieb. Master's thesis, Lappeenranta University of Technology, Lappeenranta, Finland, 2003.
- [PJHN08] J. PYRHÖNEN, T. JOKINEN, V. HRABOVCOV, and H. NIEMELÄ. *Design of Rotating Electrical Machines*. John Wiley and Sons, Ltd, 2008. Hoboken.

- [PUR06] J. PURANEN. *Induction Motor Versus Permanent Magnet Synchronous Motor in Motion Control Applications: A Comparative Study*. PhD thesis, Lappeenranta University of Technology, Lappeenranta, Finland, 2006.
- [PZZHH04] V.V PANKRATOV, Y.A. ZIMA, G.S. ZINOVIEV, and L. HONGHEE. New Approach To Energy Efficient Control Of Induction Motor Drives. *Industrial Electronics Society (IECON)*, 2:1400 – 1404, November 2004. Novosibirsk State Technical University, Russia.
- [RIE06] U. RIEFENSTAHL. *Elektrische Antriebssysteme: Grundlagen, Komponenten, Regelverfahren, Bewegungssteuerung*. Vieweg Teubner Verlag, Wiesbaden, 2006.
- [RL04] Q. RONGHAI and T. A. LIPO. Analysis and Modeling of Air-Gap and Zigzag Leakage Fluxes in a Surface-Mounted Permanent-Magnet Machine. *IEEE Transactions on Industry Applications*, 40(1):121–127, February 2004. Global Research Center, General Electric Company, Niskayuna, NY.
- [RNA11] A. ROJAS ROJAS, H. NIEDERKOFER, and J. E. W. APONTE. Optimization of Vehicle Suspension Kinematics With In-Wheel Electric Motors. *International Congress of Mechanical and Mechatronics Engineering (CIMM)*, 5th, August 2011. Bogotá, Colombia.
- [RS85] M. RAHMAN and G. SLEMON. Promising Applications of Neodymium Boron Iron Magnets in Electrical Machines. *IEEE Transactions on Magnetics*, 21(5):1712–1716, September 1985. Memorial University of Newfoundland, St. John's, Newfoundland.
- [SCH07] D. SCHRÖDER. *Elektrische Antriebe: Grundlagen*. Springer Verlag, Munich, 2007.
- [SCH09] D. SCHRÖDER. *Elektrische Antriebe-Regelung von Antriebssystemen*. Springer Verlag, Munich, 2009.
- [SIN04] D. SINELNIKOVA. *Design und optimale Betriebsführung doppelt gespeister Asynchrongeneratoren für die regenerative Energieerzeugung*. PhD thesis, Chemnitz University of Technology, Chemnitz, Germany, 2004.
- [SL88] R. SCHIFERL and T. A. LIPO. Power Capability of Salient Pole Permanent Magnet Synchronous Motors in Variable Speed Drive Applications. *Industry Applications Society Annual Meeting*, 1:23–31, October 1988. Department of Electrical & Computational Engineering, Wisconsin University, Madison, WI.
- [SMW93] D. A. STATON, T. J. E. MILLER, and S. E. WOOD. Maximising the Saliency Ratio of the Synchronous Reluctance Motor. *IEE*

- Proceedings B - Electric Power Applications.*, 140(4):249–259, July 1993. Department of Electronic & Electric Engineering, Glasgow University, Glasgow.
- [SOV09] B. K. SOVACOOOL. Early Modes of Transport in the United States: Lessons for Modern Energy Policymakers. *Policy and Society*, 27(4):411–427, 3 2009. National University of Singapore, Virginia Polytechnic Institute & State University.
- [SR08] U. SEIFFERT and G. RAINER. *Virtuelle Produktentstehung fuer Fahrzeug und Antrieb im Kfz - Prozesse, Komponenten, Beispiele aus der Praxis*, pages 1–98. Vieweg + Teubner Verlag / GWV Fachverlage GmbH, Wiesbaden, 1st edition, 2008.
- [ST05] S.STANTON and Z. TANG. Design of Interior Permanent Magnet Machines for Hybrid Electric Vehicles. *Application Workshops for High-Performance Design*, 1:1–41, 2005.
- [STA08] C. STAN. *Alternative Antriebe für Automobile - Hybridsysteme, Brennstoffzellen, alternative Energieträger*, volume 2. Springer Verlag, Berlin Heidelberg, 2008.
- [SUL04] C. SULZBERGER. An Early Road Warrior: Electric Vehicles in the Early Years of the Automobile. *IEEE Power and Energy Magazine*, 2(3):66–71, 2004. New York.
- [SUL11] S.-K. SUL. *Control of Electric Machine Drive Systems*. John Wiley and Sons, Ltd, New Jersey, 2011.
- [THI11] THIEN. THIEN eDRIVES GmbH. Available at <http://www.thien-edrives.>, 2011. Accessed on 20/09 2011.
- [THY11] THYSSENKRUPP. Thyssenkrupp electrical steel - power core. Technical report, 2011. Gelsenkirchen, Germany.
- [TSKT04] P. TURNBULL, R. D. SCHULTZ, J. KUO, and B. TURNER. Thermal Analysis of An Electric Machine for a Hybrid Vehicle. *SAE 2004 World Congress & Exhibition - Advanced Hybrid Vehicle Powertrains*, March 2004. Detroit, MI.
- [VOG88] K. VOGT. *Berechnung rotierender elektrischer Maschinen*. VEB Verlag Technik, Berlin, 1988.
- [WEI06] P. WEISS. *Ein Modell zur Simulation der transienten Vorgänge einer Asynchronlinearmaschine. Parametrierung am Beispiel eines Wirbelstromläufers*. PhD thesis, Cottbus University of Technology, Cottbus, Germany, 2006.
- [WH10] J. WILLBERGER and M. HIRZ. Energy Efficient Operation of In-wheel Motors for 4 Wheel Driven Passenger Cars. *FISITA 2010 World Automotive Congress*, 2010. Budapest, Hungary.

- [WJH02] B. A. WELCHKO, T. M. JAHNS, and S. HITI. IPM Synchronous Machine Drive Response to a Single-Phase Open Circuit Fault. *IEEE Transactions on Power Electronics*, 17(5):764–771, September 2002. Department of Electrical & Computational Engineering, Wisconsin University, WI.
- [WK09] J. WILLBERGER and K. KRISCHAN. Untersuchung, Charakterisierung und Bewertung von Elektromotoren für deren Einsatz im Kraftfahrzeug. Technical Report FTG-2009/08, Graz University of Technology, Graz, Austria, 2009.
- [WRR10] J. WILLBERGER and A. E. ROJAS-ROJAS. Der Radnabenantrieb: Eine Mechatronische Herausforderung. In *Seminar HTL Steyr - Innovationen und neue Technologien in der Fahrzeugtechnik*, Steyr, Austria, 2010.
- [WZZC04] T. WANG, P. ZHENG, Q. ZHANG, and S. CHENG. Design Characteristics of the Induction Motor Used for Hybrid Electric Vehicle. *12th Symposium on Electromagnetic Launch Technology.*, 1:523–527, May 2004. Department of Electrical Engineering, Harbin Institute of Technology, China.
- [XW07] L. XIN and S. S. WILLIAMSON. Comparative Investigation of Series and Parallel Hybrid Electric Vehicle (HEV) Efficiencies Based on Comprehensive Parametric Analysis. *Vehicle Power and Propulsion Conference (VPPC)*, 1:499–505, September 2007. Department of Electrical & Computational Engineering, Concordia University, Montreal.
- [XZH00a] L. XU, Z. Q. ZHU, and D. HOWE. Acoustic Noise Radiated From Direct Torque Controlled Induction Motor Drives. *IEE Proceedings - Electric Power Applications.*, 147(6):491–496, November 2000. Department of Electronic & Electric Engineering, Sheffield University.
- [XZH00b] L. XU, Z. Q. ZHU, and D. HOWE. Investigation of Acoustic Noise Radiated from Direct Torque Controlled Induction Machines. *3rd International Power Electronics and Motion Control Conference (IPEMC 2000).*, 2:735–740, 2000. Department of Electronic & Electric Engineering, Sheffield University.
- [YF09] C. YOOPAKDEE and N. H. FUENGWARODSAKUL. Variable Speed Switched Reluctance Drive for Low Cost Applications. *6th International Conference on Electrical Engineering/Electronics, Computer, Telecommunications and Information Technology (ECTI-CON).*, 1:262–265, May 2009. King Mongkut's University of Technology North Bangkok, Bangkok, Thailand.

- [ZBL08] D. ZARKO, D. BAN, and T.A. LIPO. Analytical Solution For Cogging Torque In Surface Permanent-Magnet Motors Using Conformal Mapping. *IEEE Transactions on Magnetics*, 44:52 – 65, January 2008. Zagreb University, Zagreb.
- [ZH07] Z. Q. ZHU and D. HOWE. Electrical Machines and Drives for Electric, Hybrid, and Fuel Cell Vehicles. *Proceedings of the IEEE*, 95(4):746–765, April 2007. Department of Electronic & Electric Engineering, University of Sheffield.
- [ZSH06] Z. Q. ZHU, J. X. SHEN, and D. HOWE. Flux-Weakening Characteristics of Trapezoidal Back-EMF Machines in Brushless DC and AC Modes. *5th International Power Electronics and Motion Control Conference (IPEMC 2006)*, 2:1–5, August 2006. Department of Electronic & Electric Engineering, University of Sheffield.
- [ZWS07] G. ZHANG, F. WANG, and Y. SHEN. Reduction Of Rotor Loss And Cogging Torque Of High Speed PM Machine By Stator Teeth Notching. *International Conference on Electrical Machines and Systems (ICEMS)*, pages 856 – 859, October 2007. Shenyang University of Technology, Shenyang.
- [ZWZ⁺09] Y. ZHU, D. WANG, G. ZHAO, D. YANG, and Y. WANG. Research Progress of Switched Reluctance Motor Drive System. *International Conference on Mechatronics and Automation (ICMA)*, 1:784–789, August 2009. School of Automobile Engineering, Harbin Institute of Technology, Weihai, China.

